ISSN 0021-3438 (Print)
ISSN 2412-8783 (Online)

IZVESTIYA

NON-FERROUS METALLURGY

Vol. 29, No. 5, 2023

Scientific and Technical Journal
Founded in 1958
6 Issues per year

ИЗВЕСТИЯ ВУЗОВ

ЦВЕТНАЯ МЕТАЛЛУРГИЯ

Том 29, № 5, 2023

Научно-технический журнал
Основан в 1958 г.
Выходит 6 раз в год

ISSN 0021-3438 (Print)
ISSN 2412-8783 (Online)

IZVESTIYA NON-FERROUS METALLURGY

Vol. 29, No. 5
2023

Scientific and Technical Journal | Founded in 1958 | 6 Issues per year | http://cvmet.misis.ru

Journal is included into the List of the peer-reviewed scientific publications recommended by the Highest Attestation Commission of the Ministry of Education and Science of the Russian Federation for publishing the results of doctoral and candidate dissertations

Abstracting/Indexing: Russian Science Citation Index (RSCI), Chemical Abstracts (Online), INIS, OCLC ArticleFirst, Ulrich's Periodicals Directory, VINITI Database (Abstract Journal)

Founder

National University of Science and Technology "MISIS"
Address: 4 build. 1 Leninskiy Prosp., Moscow 119049, Russia
http://www.misis.ru

Editorial Staff

Address: NUST MISIS, 4 build. 1 Leninskiy Prosp., Moscow 119049, Russia
Phone: +7 (495) 638-45-35
E-mail: izv.vuz@misis.ru

Certificate of registration No. 015842 (13.03.1997)
Re-registration PI No. ФС77-79229 (25.09.2020)

Subscription: Ural-Press Agency

Leading Editor – A.A. Kudinova
Executive Editor – O.V. Sosnina
Layout Designer – E.A. Legkaya

Signed print 16.10.2023. Format 60×90 1/8.
Offset paper No. 1. Digital printing. Quires 9.75
Order 18298. Free price

Printed in the printing house of the MISIS Publish House
4 build. 1 Leninskiy Prosp., Moscow 119049, Russia. Phone/fax: +7 (499) 236-76-17

ISSN 0021-3438 (Print)
ISSN 2412-8783 (Online)

ИЗВЕСТИЯ ВУЗОВ
ЦВЕТНАЯ МЕТАЛЛУРГИЯ

Том 29, № 5
2023

Научно-технический журнал Основан в 1958 г. Выходит 6 раз в год http://cvmet.misis.ru

Журнал включен в Перечень рецензируемых научных изданий, рекомендованных ВАК Минобрнауки РФ для публикации результатов диссертаций на соискание ученых степеней

Журнал включен в базы данных: Russian Science Citation Index (RSCI), Chemical Abstracts (Online), INIS, OCLC ArticleFirst, Ulrich's Periodicals Directory, РИНЦ, БД/РЖ ВИНИТИ

Учредитель

ФГАОУ ВО Национальный исследовательский технологический университет «МИСИС»
Адрес: 119049, г. Москва, Ленинский пр-т, 4, стр. 1
http://www.misis.ru

Редакция журнала

Адрес: 119049, г. Москва, Ленинский пр-т, 4, стр. 1, НИТУ МИСИС
Тел.: +7 (495) 638-45-35
E-mail: izv.vuz@misis.ru

Свидетельство о регистрации № 015842 от 13.03.1997 г.
Перерегистрация ПИ № ФС77-79229 от 25.09.2020 г.

Подписка: Агентство «Урал-пресс»

Ведущий редактор – А.А. Кудинова
Выпускающий редактор – О.В. Соснина
Дизайн и верстка – Е.А. Легкая

Подписано в печать 16.10.2023. Формат 60×90 1/8.
Бум. офсетная № 1. Печать цифровая. Усл. печ. л. 9,75
Заказ 18298. Цена свободная

Отпечатано в типографии Издательского Дома МИСИС
119049, г. Москва, Ленинский пр-т, 4, стр. 1. Тел./факс: +7 (499) 236-76-17

CONTENTS

СОДЕРЖАНИЕ

Mineral Processing of Non-Ferrous Metals

5 **Lavrinenko A.A., Kuznetsova I.N., Lusinyan O.G., Golberg G.Yu.**

Utilizing Russian polymer anion active depressants in the flotation of out-of-balance talcose copper nickel ore

Обогащение руд цветных металлов

5 **Лавриненко А.А., Кузнецова И.Н., Лусинян О.Г., Гольберг Г.Ю.**

Применение отечественных полимерных анионоактивных депрессоров при флотации забалансовой отталькованной медно-никелевой руды

Metallurgy of Non-Ferrous Metals

15 **Belousova N.V., Belousov O.V., Borisov R.V., Zhizhaev A.M., Tomashevich Ye.V.**

Production of nickel and cobalt metal powders under autoclave conditions

Металлургия цветных металлов

15 **Белоусова Н.В., Белоусов О.В., Борисов Р.В., Жижаев А.М., Томашевич Е.В.**

Получение металлических порошков никеля и кобальта в автоклавных условиях

Metallurgy of Rare and Precious Metals

25 **Targanov I.E., Solodovnikov M.A., Troshkina I.D.**

Oxidative leaching of rhenium from grinding waste of rhenium-containing superalloys

Металлургия редких и благородных металлов

25 **Тарганов И.Е., Солодовников М.А., Трошкина И.Д.**

Окислительное выщелачивание рения из шлифотходов ренийсодержащих суперсплавов

Foundry

34 **Koltygin A.V., Pavlov A.V., Bazhenov V.E., Gnatyuk O.D., Baranov I.I., Belov V.D.**

Microstructure and properties of the GEWZ522K casting magnesium alloy based on the Mg–Gd–Nd–Y–Zn–Zr system

47 **Shlyaptseva A.D., Petrov I.A., Ryakhovskiy A.P.**

Effect of different titanium-containing additives on the modification efficiency of an aluminum–silicon eutectic alloy

Литейное производство

34 **Колтыгин А.В., Павлов А.В., Баженов В.Е., Гнатюк О.Д., Баранов И.И., Белов В.Д.**

Структура и свойства литейного магниевого сплава GEWZ522K системы Mg–Gd–Nd–Y–Zn–Zr

47 **Шляпцева А.Д., Петров И.А., Ряховский А.П.**

Влияние различных титансодержащих добавок на эффективность модифицирования эвтектического сплава системы алюминий–кремний

Physical Metallurgy and Heat Treatment

57 **Ashmarin A.A., Gordeeva M.I., Betsofen S.Ya., Lozovan A.A., Wu R., Alexandrova S.S., Selivanov A.A., Bykadorov A.N., Prokopenko D.A.**

Investigation into the impact of phase composition on the thermal expansion and mechanical properties of Al–Cu–Li alloys

69 **Shliarova Yu.A., Shlyarov V.V., Zaguliaev D.V., Ivanov Yu.F., Gromov V.E.**

Electron-ion-plasma surface modification of hypereutectic silumin

Металловедение и термическая обработка

57 **Ашмарин А.А., Гордеева М.И., Бецофен С.Я., Лозован А.А., Wu R., Александрова С.С., Селиванов А.А., Быкадоров А.Н., Прокопенко Д.А.**

Исследование влияния фазового состава на термическое расширение и механические свойства сплавов Al–Cu–Li

69 **Шлярова Ю.А., Шляров В.В., Загуляев Д.В., Иванов Ю.Ф., Громов В.Е.**

Электронно-ионно-плазменное модифицирование поверхности силумина заэвтектического состава

UDC 622.765
https://doi.org/10.17073/0021-3438-2023-5-5-14

Research article
Научная статья

Utilizing Russian polymer anion active depressants in the flotation of out-of-balance talcose copper nickel ore

A.A. Lavrinenko, I.N. Kuznetsova, O.G. Lusinyan, G.Yu. Golberg

Institute of Comprehensive Exploitation of Mineral Resources n.a. Academician N.V. Melnikov of the Russian Academy of Sciences
4 Kryukovskiy Impasse, Moscow, 111020, Russia

✉ Anatoliy A. Lavrinenko (lavrin_a@mail.ru)

Abstract: Experimental studies were conducted on the flotation of low-sulfide copper-nickel ore containing flotation-active magnesium silicates, specifically talc, using organic polymeric anionic reagents containing carboxyl and hydroxyl groups as depressants. The following reagents, which contain carboxyl groups, were examined: carboxymethyl cellulose and carboxymethylated starch; polyacrylic acid and its derivatives; sodium humate. Copolymers of ethylene oxide with ethylenediamine and glycerol containing hydroxyl groups were also investigated. The objective of this study was to identify new efficient domestic depressants for flotation-active silicates, selectively acting in the flotation of low-sulfide copper-nickel ore, in comparison with the performance of foreign Depramin 347 depressant. The impact of depressant reagents on the surface properties of talc was determined by the values of air bubble detachment force and electrokinetic potential. It was observed that for reagents containing carboxyl groups, the depressing effectiveness decreased in the following order: carboxymethyl cellulose → carboxymethylated starch → polyacrylic acid → sodium humate. This reduction was attributed to a decrease in the acidic properties of the reagents, a decline in their adsorption affinity for talc, and a decrease in the proportion of active carboxyl groups participating in the formation of the electrokinetic potential. Furthermore, a trend towards increased depressing ability was noted for carboxymethyl cellulose samples with an increasing degree of substitution. In contrast, reagents containing hydroxyl groups had virtually no depressing effect on talc. The data obtained support the use of domestic industrial samples of carboxymethyl cellulose, namely CMC 7N and PAC-N, as depressants for floating silicates, particularly talc, which is a detrimental impurity in the concentrate.

Keywords: flotation, copper-nickel sulfide ore, talc, depressants, carboxyl groups, hydroxyl groups, air bubble detachment force, electrokinetic potential, adsorption.

For citation: Lavrinenko A.A., Kuznetsova I.N., Lusinyan O.G., Golberg G.Yu. Utilizing Russian polymer anion active depressants in the flotation of out-of-balance talcose copper nickel ore. *Izvestiya. Non-Ferrous Metallurgy.* 2023;29(5):5–14.
https://doi.org/10.17073/0021-3438-2023-5-5-14

Применение отечественных полимерных анионоактивных депрессоров при флотации забалансовой отталькованной медно-никелевой руды

А.А. Лавриненко, И.Н. Кузнецова, О.Г. Лусинян, Г.Ю. Гольберг

Институт проблем комплексного освоения недр им. академика Н.В. Мельникова Российской академии наук
111020, Россия, г. Москва, Крюковский тупик, 4

✉ Анатолий Афанасьевич Лавриненко (lavrin_a@mail.ru)

Аннотация: Были выполнены экспериментальные исследования по флотации малосульфидной медно-никелевой руды, содержащей флотоактивные магниевые силикаты, в частности тальк, с применением в качестве депрессоров органических полимерных анионоактивных реагентов, содержащих карбоксильные и гидроксильные группы. Исследовали следующие реагенты, содержащие карбоксильные группы: карбоксиметилированные целлюлоза и крахмал; полиакриловая кислота и ее производные; гумат

натрия. Также изучали сополимеры окиси этилена с этилендиамином и глицерином, содержащие гидроксильные группы. Цель исследования – выявление новых эффективных отечественных депрессоров флотоактивных силикатов, селективно действующих при флотации малосульфидной медно-никелевой руды, по сравнению с действием зарубежного депрессора Depramin 347. Влияние реагентов-депрессоров на поверхностные свойства талька определяли по значениям силы отрыва пузырька воздуха и электрокинетического потенциала. Установлено, что для реагентов, содержащих карбоксильные группы, депрессирующая способность убывает в следующей последовательности: карбоксиметилцеллюлоза → карбоксиметилированный крахмал → полиакриловая кислота → гумат натрия. Это обусловлено уменьшением кислотных свойств реагентов, убыванием их адсорбционного сродства к тальку и снижением доли активных карбоксильных групп, принимающих участие в формировании электрокинетического потенциала. При этом выявлена тенденция к возрастанию депрессирующей способности образцов карбоксиметилцеллюлозы с увеличением степени замещения. В то же время реагенты, содержащие гидроксильные группы, практически не оказывают депрессирующего действия на тальк. Полученные данные обосновывают применение отечественных промышленных образцов карбоксиметилцеллюлозы (КМЦ 7Н, ПАЦ-Н), в частности в качестве депрессоров талька при флотации медно-никелевой руды, что позволяет снизить содержание в концентрате талька, являющегося вредной примесью.

Ключевые слова: флотация, медно-никелевая сульфидная руда, тальк, депрессоры, карбоксильные группы, гидроксильные группы, сила отрыва пузырька воздуха, электрокинетический потенциал, адсорбция.

Для цитирования: Лавриненко А.А., Кузнецова И.Н., Лусинян О.Г., Гольберг Г.Ю. Применение отечественных полимерных анионоактивных депрессоров при флотации забалансовой отталькованной медно-никелевой руды. *Известия вузов. Цветная металлургия*. 2023;29(5):5–14. https://doi.org/10.17073/0021-3438-2023-5-5-14

Introduction

Sulfide copper-nickel ores serve as a valuable source not only for copper and approximately 90 % nickel but also for platinum group metals (PGM), gold, silver, cobalt, selenium, tellurium, and other rare and trace elements. These elements are closely associated with sulfides of base metals and sometimes with the surrounding rock. As free-milling ore reserves continue to deplete, the industrial utilization of complex raw materials with low concentrations of valuable components becomes necessary. This demands the development of new reagent flotation modes.

A significant challenge in processing both sulfide and particularly low-sulfide copper-nickel ores is the presence of hydrophobic waste rock minerals, notably magnesium silicates such as talc, chlorite, sericite, and olivine (forsterite). These minerals readily enter flotation concentrates, increasing smelting costs and reducing smelting efficiency. Hydrophilic silicates also contribute negatively. For example, complex orthopyroxene particles with a talc periphery significantly dilute concentrates in the flotation of Merensky Reef ores [1]. Hydrophilic serpentine enters the concentrate due to partial coating of sulfides by oppositely charged serpentine slurry particles, which diminishes the recovery and flotation rate of sulfides [2].

The significance of researching the processing of low-sulfide copper-nickel ores with high talc content stems from the necessity to depress the flotation of flotation-active magnesium-bearing silicate minerals.

In global practices of copper-nickel ore concentration, non-toxic natural polysaccharides such as guar gum, carboxymethyl cellulose (CMC), and occasionally dextrin, either individually or in combination, are widely employed as depressants for hydrophobic waste rock [3]. The most effective depressant for hydrophobic silicates is guar gum, although its high cost and limited availability (mostly used abroad) present challenges [4]. The depression of magnesium-containing silicates can also be achieved using more readily available and cost-effective polysaccharides, thanks to their widespread sources of production and annual reproducibility. These include starch derivatives, dextrin, and carboxymethyl starches (CMS) [5—8]. However, apart from a few derivatives like dextrin, there is limited documentation on the use of starch derivatives as depressants in sulfide minerals flotation [8].

In Russia, the depression of hydrophobic waste rock during the flotation of copper-nickel ores relies on the use of a more readily available anionic polysaccharide polymer, carboxymethyl cellulose (CMC). The most challenging issue encountered is the depression of talc, which, due to its inherent high hydrophobicity, is susceptible to degradation in an aqueous environment, resulting in the formation of fine particles. Talc also exhibits exceptionally high flotation activity, presenting significant challenges in the flotation process of complex PGM-containing copper-nickel sulfide ores [4]. The adsorption of an anionic polymer onto talc is influenced by various factors, including the characteristics of the polymer (such as type, number of ionized polar groups, degree of substitution (DS), and molar mass (MM)), as well as solution properties [5; 9—13].

Since hydrophobic interaction plays a pivotal role in the sorption of polymeric depressants onto talc, adsorption increases with the degree of polymerization of the reagent, augments the hydrophobicity of the macromolecule. However, high molecular weight polymers exhibit lower selectivity compared to their low molecular weight counterparts [5]. Polysaccharides and other polymers traditionally employed in the flotation of sulfide ores typically have molar masses (MM) in the range of 150—600 t/kmol. In recent years, polysaccharides with lower MM (100—150 t/kmol) have also proven to be effective [14].

The depressant effect of anionic polymers on talc diminishes as the pH increases. At high pH and low ionic strength of the solution, the adsorption density of anionic polymers is at its lowest. Conversely, at high ionic strength and low pH, especially in the presence of Mg, Ca, and other ions, the adsorption density increases [9—13]. The presence of divalent and trivalent cations enhances the depression of talc but also reduces the selectivity in the flotation of mineral mixtures. The degree of polymer substitution influences not only its solubility but also its ability to be adsorbed onto talc and sulfide minerals [13; 15].

The interaction mechanisms between polysaccharides and mineral surfaces encompass hydrophobic, chemical, electrostatic, and acid-base interactions, in addition to the formation of hydrogen bonds [5; 9; 15; 16]. These mechanisms contribute to the partial adsorption of polysaccharides onto sulfide minerals, thereby impeding their flotation. The interaction between polysaccharides and sulfides has received limited research attention [6]. The selectivity of their effects during flotation is contingent upon MM and DS values [16]. Few studies have explored the impact of the polymer's chemical nature on selectivity, and typically, the choice of polymer for waste rock depression is made through empirical means.

Previous studies have focused on the depressant properties of corn dextrin from Bio Polimer, Depramin 267 and 347 CMC from Akzo Nobel, and the synthetic polymer Akremon D-13 [17]. Additionally, carboxymethylated corn starches (CMS) with varying viscosities, synthesized at the Research Institute of Starch Products, have been examined [6]. The most favorable results were obtained with the Depramin 347 depressant.

This study aims to identify effective domestic depressants for silicate flotation that exhibit selectivity in the flotation of low-sulfide copper-nickel ore, in comparison to the foreign depressant Depramin 347.

Research methodology

The research focuses on investigating the depressant effect during the flotation of out-of-balance talcose copper-nickel ore and the hydrophilic properties of Russia-manufactured anionic polymers with varying degrees of substitution (DS) and viscosity (MM-related characteristics) towards talc and sulfides. This study also involves comparing these reagents with the most effective depressant identified in previous research, Depramin 347 (refer to Table 1).

Flotation experiments were conducted using out-of-balance ore, which contained the following components by weight: 0.12 % Cu, 0.2 % Ni, 0.01 % Co, 0.8 % S, 1.9 % Fe, 0.94 % Mg, 50.5 % SiO_2, 1.1 g/t Pd, 0.2 g/t Pt, and 0.06 g/t Au. The mineral composition of the ore consisted of chalcopyrite (0.3 %), pentlandite (0.6 %), pyrrhotite (0.2 %), pyrite (0.14 %), pyroxenes (58 %), talcum powder (12 %), amphiboles (8 %), magnesite (3.75 %), plagioclases (1 %), and other constituents.

Flotation of the ore, which was ground to 84 % fineness at –71 μm, was carried out under natural pH conditions of 7. The primary flotation process began with the addition of a silicate depressant, followed by Aerophine 3416 and butyl xanthogenate collectors at a rate of 25 g/t each, and MIBK foaming agent at a rate of 20 g/t. Control flotation received 40 % of the reagents from the primary flotation flow rate. Subsequently, concentrates from both the primary and control flotations were combined.

For the flotation of a 5 g sample of talc, which was ground to –71 μm, a 100 mL chamber was used presence of 50 mg/L MIBK.

In order to investigate the hydrophilizing effects of the depressants, we employed a method that assesses mineral wettability by measuring the detachment force of an air bubble from the mineral surface in a reagent solution.

The examination of the interactions between depressants of varying viscosity and DS with the surfaces of sulfides and talc was conducted by measuring the ζ-potential of minerals using a ZETA-check PMX 500 instrument (Germany). The cell had a volume of 50 mL, and the weight of finely ground mineral used was 0.2 g.

The depressant's effectiveness was assessed by calculating the relative reduction in Ni and Si recovery in the concentrate, expressed as a percentage:

$$\Delta = 100 \frac{\varepsilon_0 - \varepsilon_i}{\varepsilon_0},$$

where ε_0 represents the component extraction without

Properties of investigated reagents

Характеристика исследованных реагентов

Description	Dynamic viscosity of 2 % solution at t = 25 °C, mPa·s; MM	Degree of substitution (DS)
Containing carboxyl groups (–COOH)		
Carboxymethylated starch CMS BUR-1V (ZAO Polycell), 60 % active substance	about 300 (4 % solution)	0.4
Carboxymethyl cellulose CMC 7N (ZAO "Polycell"), 50 % active substance	≤ 40 (Höppler), ≤ 140 (Brookfield), degree of polymerization – 350	0.6–0.8
Carboxymethyl cellulose (polyanionic cellulose) PAC-N (ZAO "Polycell"), 45 % active substance	≤ 40 (Höppler), ≤ 170 (Brookfield), degree of polymerization – 500, MM ~ 116 000	0.9
Carboxymethyl cellulose Depramin 347 ("Akzo Nobel"), 80 % active substance	91 (Brookfield)	0.54
Na humate (mixture of polycondensed aromatic compounds containing side OH- and COOH-groups)	–	–
Macromer 30H (NPP "Macromer"), polyacrylic acid, 45 % active substance	MM ~ 12 000	
Macromer 17N (NPP "Macromer"), polyacrylic acid with grafted polyoxyethylene glycol chains (PAA), 50 % active substance	MM ~ 36 000	
Containing hydroxyl groups (–OH)		
Laprol 3703-2-37 (NPP "Makromer") based on glycerol, block copolymer with ethylene oxide: 37 %, 100 % active substance	MM ~ 3700	
Lapramol 6504 (NPP "Makromer") based on ethylenediamine, 25–30 % ethylene oxide, propylene oxide, 100 % active substance	MM ~ 6500	

the depressant, ε_i represents the component extraction at the i-th depressant flow rate.

The selectivity of the depressant's action was determined using Cohen's enrichment factor (I):

$$I = \varepsilon_{Ni} / \varepsilon_{Si}.$$

Results and discussion

The results of copper-nickel ore flotation process for talc and other silicates depression using reagents, displayed in the table, are illustrated in Fig. 1. The selectivity of the reagent action is depicted in Fig. 2.

Based on the obtained data, it can be concluded that the suppressive effect of depressants on the flotation of silicates and sulfides follows this order: PAC-N ≅ ≅ CMS 7N > Depramin 347 > Na humate ≅ CMS BUR-1V (as shown in Figs. 1 and 2). However, CMC with a higher degree of polymerization and DS (CMC 7N and PAC-N) exhibited lower selectivity at low flow rates. Yet, at flow rates exceeding 600 g/t, their selectivity improves to the level of Depramin 347.

Depressants containing hydroxyl groups (Laprol, Lapramol), as well as Macromer 30N with MM ~ 12000 at a flow rate of 400 g/t, had almost no impact on the flotation results of the ore under investigation (the concentrate yield decreased by approximately 1 %). However, when using Macromer 17N with an MM of 36000, the depressant's effectiveness increased. The concentrate yield decreased by 5 %, and the nickel recovery in the concentrate also decreased by 5 %.

The investigation into talc flotation with MIBK in the presence of CMC depressants revealed an escalation in the depressant's impact as the viscosity (molar mass) and DS of CMCs increased, particularly for PAC-N (as demonstrated in Fig. 3). The hierarchy of dimin-

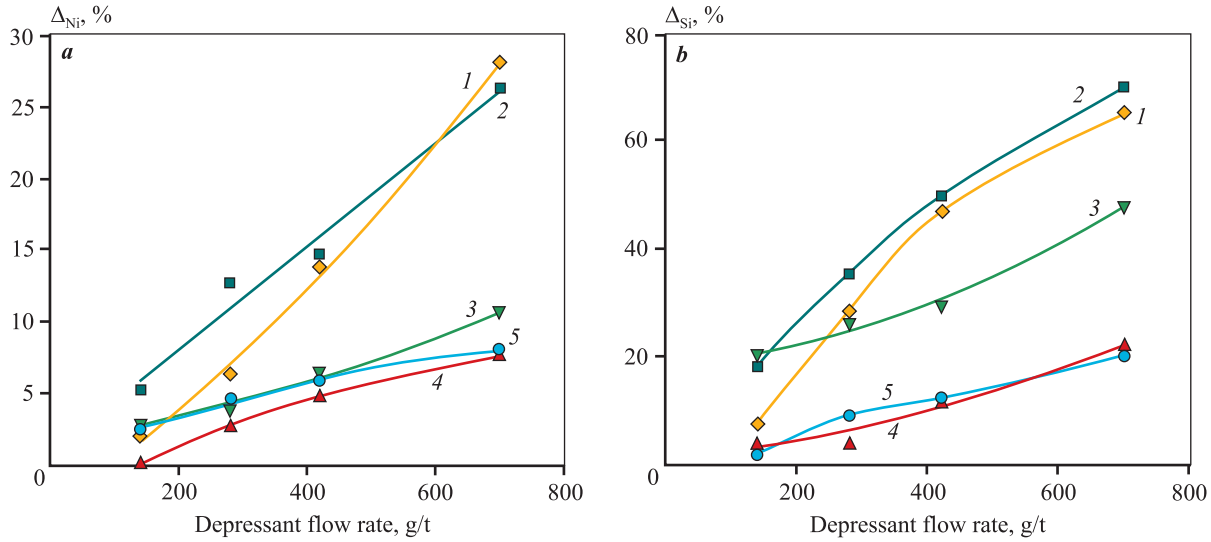

Fig. 1. Relative decrease (Δ) in Ni (***a***) and Si (***b***) recovery into concentrate during Cu–Ni ore flotation
1 – CMC 7N; ***2*** – PAC-N; ***3*** – Depramin 347; ***4*** – CMS BUR-1V; ***5*** – sodium humate

Рис. 1. Относительное снижение (Δ) извлечения Ni (***a***) и Si (***b***) в концентрат при флотации Cu–Ni руды
1 – КМЦ 7Н; ***2*** – ПАЦ-Н; ***3*** – Depramin 347; ***4*** – КМК БУР-1В; ***5*** – гумат Na

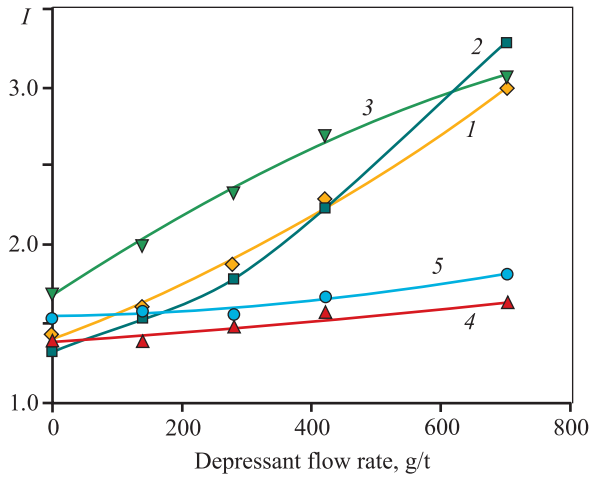

Fig. 2. Cohen's enrichment factor (Ni from Si) (*1*)
1 – CMC 7N; ***2*** – PAC-N; ***3*** – Depramin 347, ***4*** – CMS BUR-1V; ***5*** – sodium humate

Рис. 2. Коэффициент разделения Ni от Si по Коэну (*1*)
1 – КМЦ 7Н; ***2*** – ПАЦ-Н; ***3*** – Depramin 347; ***4*** – КМК БУР-1В; ***5*** – гумат Na

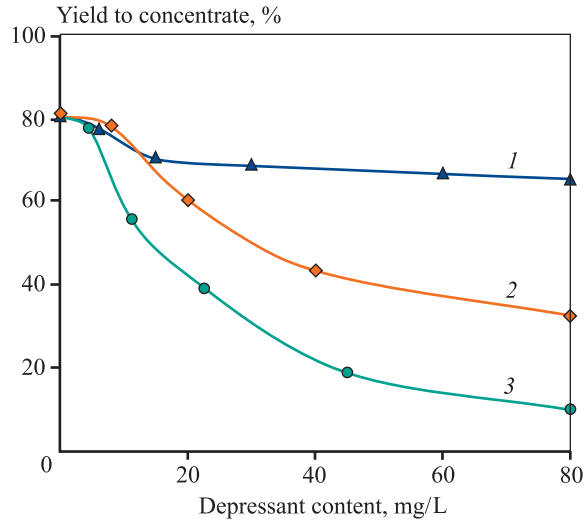

Fig. 3. The influence on talc flotation with MIBC: CMS (*1*), Depramin 347 (*2*) and PAC-N (*3*)

Рис. 3. Влияние КМК (*1*), Depramin 347 (*2*) и ПАЦ-Н (*3*) на флотацию талька с МИБК

ishing suppressive effects of depressants is as follows: PAC-N — Depramin 347 — CMS.

In order to elucidate the mechanism of action of the polysaccharides used on the primary ore minerals (pentlandite, pyrrhotite) and talc, studies were conducted to assess their hydrophobicity and surface charge following treatment with depressants.

The impact of depressant adsorption on altering the hydrophobicity of minerals, assessed through the air bubble detachment force from the slurry of talc, pentlandite, and pyrrhotite, was substantiated by the results obtained from flotation experiments. Detachment force measurements were conducted in the presence of a combination of Aerophine 3416 A and butyl xanthogenate (in a 1 : 1 ratio) with a total concentration of 30 mg/L. The data depicted in Fig. 4 demonstrate that CMC-based depressants significantly enhance the hydrophilicity of the talc surface when compared to CMC and

Na humate. The degree of hydrophilization decreases in the following order: PAC-N > Depramin 347 > > CMC 7N > CMS > Na humate = CMS BUR-1V. Simultaneously, all investigated depressants also diminish the hydrophobicity of sulfides, with the most pronounced effect observed in the presence of PAC-N and CMC 7N.

Measurements of the electrokinetic potential of the examined minerals revealed that CMCs with higher viscosity and DS exert a more pronounced effect on shifting the ζ-potential of talc towards negative values (as illustrated in Fig. 5). The influence of CMS and CMC on the ζ-potential of talc remains consistent across the pH range of 7 to 9 (as shown in Fig. 6). Furthermore, for pH levels greater than 7, the negative ζ-potential of talc remains essentially unaltered [18; 19]. Therefore, altering the pH within the range of 7 to 9 is unlikely to affect the adsorption of anionic CMC and CMS. These findings strongly suggest that the primary mechanism driving the adsorption of polysaccharides onto talc is hydrophobic interaction, rather than electrostatic forces.

The negative shift in the ζ-potential on pyrrhotite and chalcopyrite following interaction with anionic polysaccharides indirectly suggests the adsorption of these polymers, as shown in Figs. 7 and 8. The most significant shift is observed on pyrrhotite, particularly in the presence of high-viscosity depressants like CMC 7N and CMS BUR-1V, and this shift intensifies as pH levels increase. A similar correlation was noted, for instance, with starch tricarboxylate as a depressant [19]. It appears that a larger quantity of these polysaccharides is adsorbed onto the pyrrhotite surface compared to chalcopyrite. This was hypothesized to be due to the presence of more metal hydroxyl layers on pyrrhotite, which facilitated greater polysaccharide adsorption [19].

The studies have demonstrated that CMC-based depressants exhibit superior efficiency, both in terms of silicate suppression and the selectivity of their action, when compared to CMS and Na humate in the flotation of talcose copper-nickel ore. As the viscosity (degree of polymerization) of CMC and its DS increase, the suppressive effect of the polymer on both silicates and sulfides intensifies, yet the selectivity in separating sulfides from silicates diminishes. Among the investigated options, CMS with average values of these characteristics prove to be the most effective for the flotation of low-sulfide Cu—Ni ore.

An analysis of the averaged relative changes in the interaction between talc and the examined depres-

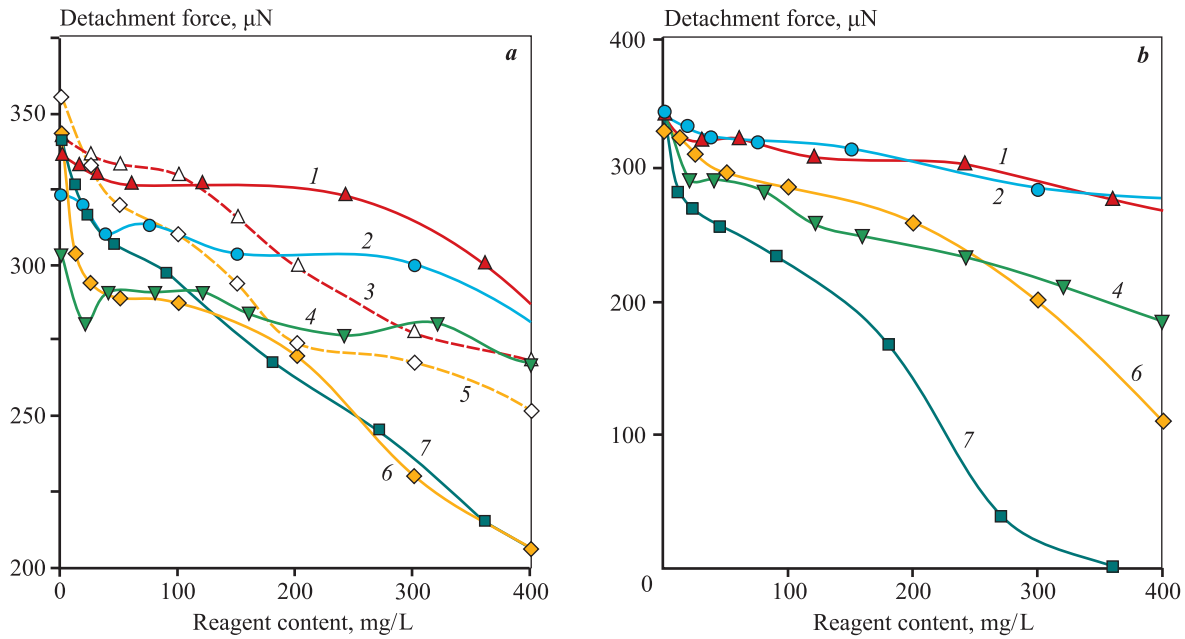

Fig. 4. Detachment force of air bubble from pentlandite (***1***, ***2***, ***4***, ***6***, *7*) and pyrrhotite (*3*, *5*) (***a***) and talc (***b***) in the presence of depressants:

1, *3* – CMS BUR-1V; ***2*** – sodium humate; ***4*** – Depramin 347; ***5***, ***6*** – CMC 7N; *7* – PAC-N

Рис. 4. Сила отрыва пузырька воздуха от пентландита (***1***, ***2***, ***4***, ***6***, *7*) и пирротина (*3*, *5*) (***a***), а также талька (***b***) в присутствии депрессоров

1, *3* – КМК БУР-1В; ***2*** – гумат Na; ***4*** – Depramin 347; ***5***, ***6*** – КМЦ 7Н; *7* – ПАЦ-Н

sants, in conjunction with the known physicochemical properties of these reagents, including values such as the acidity constant (*pKa*) and their maximum adsorption capacity on the talc surface (*G*) [20—26], reveals that the efficiency of depressants in the flotation of talcose copper-nickel ore follows a descending order: carboxymethyl cellulose → carboxymethylated starch → polyacrylic acid (PAA) → sodium humate (SH)

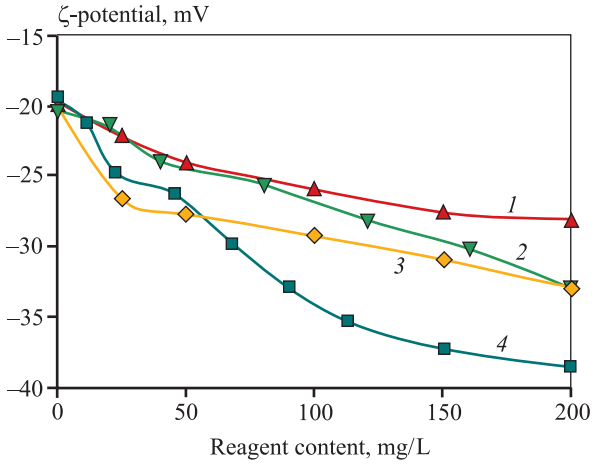

Fig. 5. Comparison of anionic depressants influence on talc zeta potential at pH = 9

1 – CMS BUR-1V; ***2*** – Depramin 347; ***3*** – CMC 7N; ***4*** – PAC-N

Рис. 5. Сравнение влияния анионных депрессоров на ζ-потенциал талька при pH = 9

1 – КМК БУР-1В; ***2*** – Depramin 347; ***3*** – КМЦ 7Н; ***4*** – ПАЦ-Н

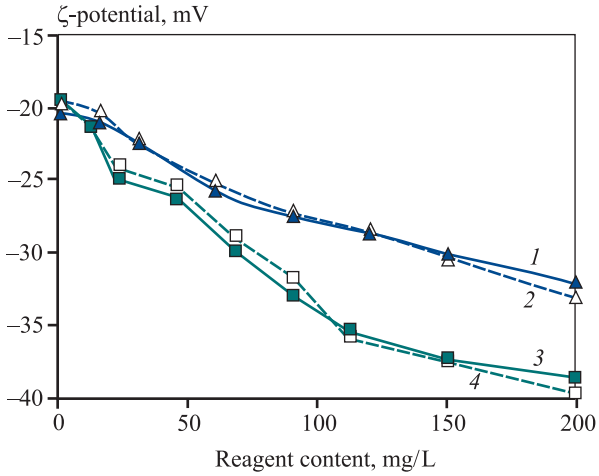

Fig. 6. pH influence on talc ζ-potential in the presence of depressants

1, ***2*** – CMS; ***3***, ***4*** – PAC-N
1, ***3*** – pH = 9; ***2***, ***4*** – pH = 7

Рис. 6. Влияние pH на ζ-потенциал талька в присутствии депрессоров

1, ***2*** – КМК; ***3***, ***4*** – ПАЦ-Н
1, ***3*** – pH = 9; ***2***, ***4*** – pH = 7

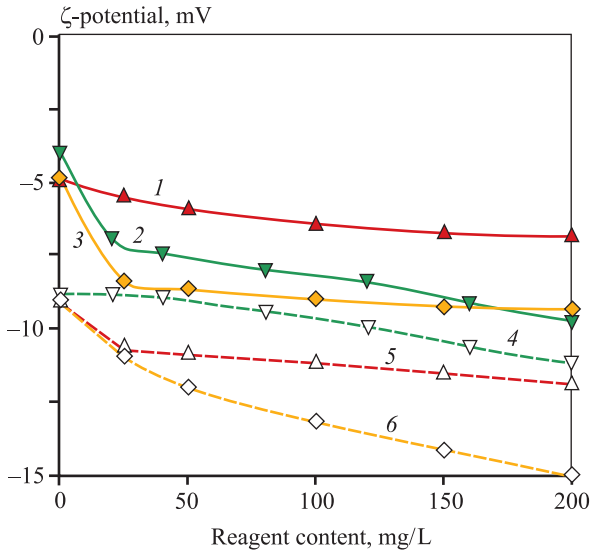

Fig. 7. Influence of depressants concentration on ζ-potential of chalcopyrite (***1–3***) and pyrrhotite (***4–6***) at pH = 7

1, ***5*** – CMS BUR-1V; ***2***, ***4*** – Depramin 347; ***3***, ***6*** – CMC 7N

Рис. 7. Влияние концентрации депрессоров на ζ-потенциал халькопирита (***1–3***) и пирротина (***4–6***) при pH = 7

1, ***5*** – КМК БУР-1В; ***2***, ***4*** – Depramin 347; ***3***, ***6*** – КМЦ 7Н

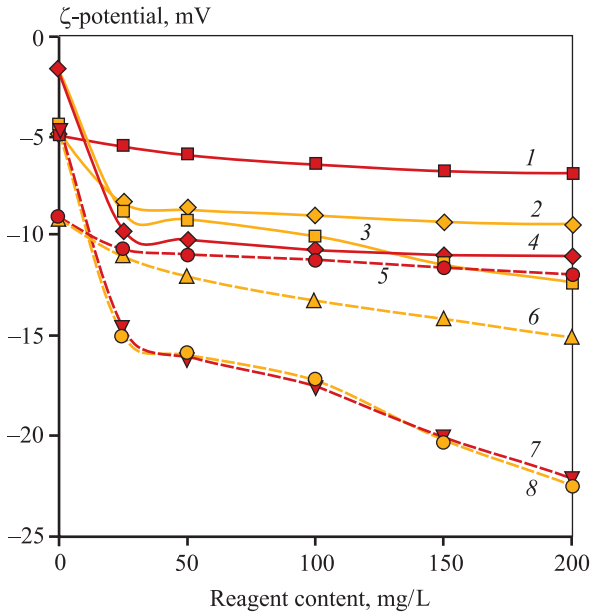

Fig. 8. Electrokinetic potential of chalcopyrite (***1–4***) and pyrrhotite (***5–8***) with CMS BUR-1V (***1***, ***4***, ***5***, ***7***) and CMC 7N (***2***, ***3***, ***6***, ***8***) at pH = 7 (***1***, ***2***, ***5***, ***6***) and pH = 9 (***3***, ***4***, ***7***, ***8***)

Рис. 8. Электрокинетический потенциал халькопирита (***1–4***) и пирротина (***5–8***) в присутствии КМК БУР-1В (***1***, ***4***, ***5***, ***7***) и КМЦ 7Н (***2***, ***3***, ***6***, ***8***) при pH = 7 (***1***, ***2***, ***5***, ***6***) и pH = 9 (***3***, ***4***, ***7***, ***8***)

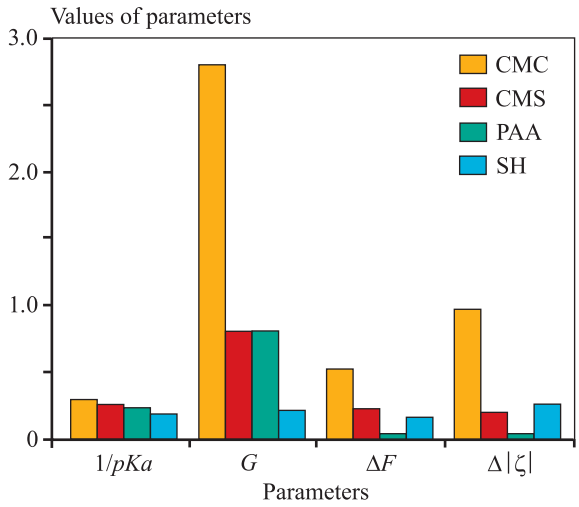

Fig. 9. Relative change of interaction parameters for polymeric reagents with talc

Γ – adsorption value, mg/m^2; ΔF – relative decrease of detachment force; $\Delta|\zeta|$ – relative increase of electrokinetic potential modulus; *pKa* – the indicator of acidity constant

Рис. 9. Относительное изменение параметров взаимодействия полимерных реагентов-депрессоров с тальком

Γ – величина адсорбции, мг/м^2; ΔF – относительное снижение силы отрыва, доли ед.; $\Delta|\zeta|$ – относительное увеличение модуля электрокинетического потенциала, доли ед.; *pKa* – показатель константы кислотности

(Fig. 9). This decrease in efficiency can be attributed to a reduction in the acidic properties of the reagents, a decline in their affinity for adsorption onto talc, and a decrease in the proportion of active carboxyl groups participating in the formation of the electrokinetic potential.

Therefore, it can be deduced from the collected data that polyanionic cellulose PAC-N and CMC 7N exhibit the highest depressant capacity when it comes to the flotation of sulfides in comparison to talc.

Based on a comprehensive set of experimental and analytical studies concerning the depressant impact of domestic samples of carboxymethylated starch (CMS BUR, CMS-363), carboxymethyl cellulose (PAC-N, CMC 7N), polyacrylic acid (PAA), and sodium humate (SH) in relation to talc (flotation-active silicates) during the flotation of talcose low-sulfide copper-nickel ore, a consistent pattern has been established regarding the diminishing depressing efficacy of the studied reagents containing carboxyl groups in relation to talc. Furthermore, a notable trend towards an increased depressant effectiveness of CMC samples with a higher degree of substitution has been observed. This holds the promise of reducing the content of undesirable impurities in the concentrate.

Conclusions

Based on an extensive series of experimental and analytical investigations regarding the depressing effects of domestically sourced polymeric anionic reagents containing carboxyl groups on talc (flotation-active silicates) during the flotation of talcose low-sulfide Cu—Ni ore, a discernible pattern emerges: their depressing effectiveness decreases in the following order-carboxymethyl cellulose → carboxymethylated starch → polyacrylic acid → sodium humate. This reduction can be ascribed to a decrease in parameters indicative of the reagents' affinity for talc. Remarkably, an increase in the degree of substitution within CMC molecules corresponds to an augmentation of their capacity to depress talc. These findings solidify the recommendation to employ domestic industrial samples of carboxymethyl cellulose PAC-N and CMC 7N as depressants for silicates, particularly talc, which is recognized as an undesirable impurity in the concentrate.

References

1. Becker M., Harris P.J., Wiese J.G., Bradshaw D.J. Mineralogical characterisation of naturally floatable gangue in Merensky Reef ore flotation. *International Journal of Mineral Processing.* 2009;93(3-4):246—255. https://doi.org/10.1016/j.minpro.2009.10.004
2. Kusuma Andreas M., Liu Qingxia, Zeng Hongbo. Understanding interaction mechanisms between pentlandite and gangue minerals by zeta potential and surface force measurements. *Minerals Engineering.* 2014;69:15—23. https://doi.org/10.1016/j.mineng.2014.07.005
3. Bulatovic S.M. Handbook of flotation reagents. Chemistry, theory and practice. Flotation sulfide ores. Amsterdam: Elsevier, 2007. 448 p.
4. Zhao K., Gu G., Wang C., Rao X., Wang X., Xiong X. The effect of a new polysaccharide on the depression of talc and the flotation of a nickel-copper sulfide ore. *Minerals Engineering.* 2015;77:99—106. https://doi.org/10.1016/j.mineng.2015.02.014.5,8,13,14
5. Beattie David A., Huynh Le, Kaggwa Gillian B.N., Ralston John. The effect of polysaccharides and polyacrylamides on the depression of talc and the flotation of sulphide minerals. *Minerals Engineering.* 2006;19(6-8):598—608. https://doi.org/10.1016/j.mineng.2005.09.011
6. Lavrinenko A.A., Kuznetsova I.N., Sarkisova L.M., Shrader E.A., Kopyl'tsov A.A. Influence of the molecular weight of carboxymethylated starches on their depressant action during flotation of talc platinum-metal Cu—Ni ore. In: *Scientific foundations and practice of processing ores and technogenic raw materials:* XXVII International scientific

and technical conference held within the frame work of the XX Ural mining and industrial decade (Ekaterinburg, 7—8 April, 2022). Ekaterinburg : IP Russkikh A.V., 2022. P. 216—219. (In Russ.).
Лавриненко А.А., Кузнецова И.Н., Саркисова Л.М., Шрадер Э.А., Копыльцов А.А. Влияние молекулярного веса карбоксиметилированных крахмалов на их депрессирующее действие при флотации отальк-ованной платинометалльной Cu—Ni руды. В сб.: *Научные основы и практика переработки руд и техногенного сырья:* Материалы XXVII Международной научно-технической конференции, проводимой в рамках XX Уральской горнопромышленной декады (г. Екатеринбург, 7—8 апреля 2022 г.). Екатеринбург: ИП Русских А.В., 2022. С. 216—219.

7. Zhang Chenxu, Tan Yiping, Yin Fengxiang, Wu Jiamei, Wang Lichang, Cao Jian. The influence of branched chain length on different causticized starches for the depression of serpentine in the flotation of pentlandite. *Minerals*. 2022;12:1081. https://doi.org/10.3390/min12091081
8. Khoso Sultan Ahmed, Hu Yuehua, Liu Runqing, Tian Mengjie, Sun Wei, Gao Ya, Han Haisheng, Gao Zhiyong. Selective depression of pyrite with a novel functionally modified biopolymer in a Cu—Fe flotation system. *Minerals Engineering*. 2019;135:55—63. https://doi.org/10.1016/j.mineng.2019.02.044
9. Morris G.E, Fornasiero D., Ralston J. Polymer depressants at the talc-water interface adsorption isotherm, microflotation and electrokinetic studies. *International Journal of Mineral Processing*. 2002;67:211—227.
10. Parolis L.A.S., Groenmeyer G.V., Harris P.J. Equilibrium adsorption studies of polysaccharides on talc: The effects of molecular weight and charge and the influence of metal cations. *Mining, Metallurgy & Exploration Volume*. 2005;22:12—16.
11. McFadzean B., Dicks P., Groenmeyer G., Harris P., O'Connor C. The effect of molecular weight on the adsorption and efficacy of polysaccharide depressants. *Minerals Engineering*. 2011;24(5):463—469.
12. Khraisheh M., Holland C., Creany C., Harris P., Parolis L. Effect of molecular weight and concentration on the adsorption of CMC onto talc at different ionic strengths. *International Journal of Mineral Processing*. 2005;75: 197—206. https://doi.org/10.1016/j.minpro.2004.08.012
13. Parolis Lesley A.S., Rene van der Merwe, Groenmeyer Gary V., Harris Peter J. The influence of metal cations on the behaviour of carboxymethyl celluloses as talc depressants. *Colloids and Surfaces A: Physicochemical and Engineering Aspects*. 2008;317(1-3):109—115. https://doi.org/10.1016/j.colsurfa.2007.10.001
14. Wiese J.G., Harris P.J., Bradshaw D.J. The use of very low molecular weight polysaccharides as depressants in PGM flotation. *Minerals Engineering*. 2008;21(6): 471—482. https://doi.org/10.1016/j.mineng.2008.02.013
15. Mierczynska-Vasilev Agnieszka, Beattie David A. Adsorption of tailored carboxymethyl cellulose polymers on talc and chalcopyrite: Correlation between coverage, wettability, and flotation. *Minerals Engineering*. 2010;23(11-13):985—993.
16. Jenkins P., Ralston J. Adsorption of a polysaccharide at the talc-aqueous solution interface. *Colloids Surf. A: Physicochem. Eng. Asp.* 1998;139:27—40.
17. Kuznetsova I.N., Lavrinenko A.A., Shrader E.A., Sarkisova L.M. Reduction in flotation-active silicate recovery in bulk concentrate of low-sulphide platinum-metal ore. *Mining Informational and Analytical Bulletin*. 2019;5:200—208. (In Russ.).
Кузнецова И.Н., Лавриненко А.А., Шрадер Э.А., Саркисова Л.М. Снижение извлечения флотоактивных силикатов в коллективный концентрат при флотации малосульфидной платинометалльной руды. *Горный информационно-аналитический бюллетень (научно-технический журнал).* 2019;5: 200—208. https://doi.org/10.25018/0236-1493-2019-05-0-200-208
18. Khoso Sultan Ahmed, Gao Zhiyong, Tian Mengjie, Hu Yuehua, Sun Wei. Adsorption and depression mechanism of an environmentally friendly reagent in differential flotation of Cu—Fe sulphides. *Journal of Materials Research and Technology*. 2019;8(6):5422—5431. https://doi.org/10.1016/j.jmrt.2019.09.00
19. Khoso Sultan Ahmed, Hu Yuehua, Liu Runqing, Tian Mengjie, Sun Wei, Gao Ya, Han Haisheng, Gao Zhiyong. Selective depression of pyrite with a novel functionally modified biopolymer in a Cu—Fe flotation system. *Minerals Engineering*. 2019;135:55—63. https://doi.org/10.1016/j.mineng.2019.02.044
20. Zhivkov A.M. Electric properties of carboxymethyl cellulose. In: *Cellulose — fundamental aspects*. Eds. T. van de Ven, L. Godbout. London: IntechOpen, 2013. P. 197—226.
21. Lefnaoui S., Moulai-Mostefa N. Synthesis and evaluation of the structural and physicochemical properties of carboxymethyl pregelatinized starch as a pharmaceutical excipient. *Saudi Pharmaceutical Journal*. 2015;23: 698—711.
22. Wiśniewska M., Urban T., Grządka E., Zarko V.I., Gun'ko V.M. Comparison of adsorption affinity of polyacrylic acid for surfaces of mixed silica—alumina. *Colloid and Polymer Science*. 2014;292:699—705.
23. Laird D.A., Koskinen W.C. Triazine soil interactions. In: *The triazine herbicides*. Eds. LeBaron H.M., McFar-

land J.E., Burnside O.C. Amsterdam: Elsevier B.V., 2008. P. 275—299.
24. Bazar J.A., Rahimi M., Fathinia S., Jafari M., Chipakwe V., Chelgani S.C. Talc flotation: An overview. *Minerals*. 2021;11:662.
25. Morris G.E., Fornasiero D., Ralston J. Polymer depressants at the talc-water interface: adsorption isotherm, microflotation and electrokinetic studies. *International Journal of Mineral Processing*. 2002;67:211—227.
26. Duowei Yuan, Lei Xie, Xingwei Shi, Longsheng Yi, Guofan Zhang, Hao Zhang, Qi Liu, Hongbo Zeng. Selective flotation separation of molybdenite and talc by humic substances. *Minerals Engineering*. 2018;117: 34—41.

Information about the authors

Anatoliy A. Lavrinenko – Dr. Sc. (Eng.), Chief Researcher, Head of laboratory, Institute of Comprehensive Exploitation of Mineral Resources n.a. Academician N.V. Melnikov of the Russian Academy of Sciences (ICEMR RAS).
https://orcid.org/0000-0002-7955-5273
E-mail: lavrin_a@mail.ru

Irina N. Kuznetsova – Cand. Sci. (Eng.), Senior Researcher, ICEMR RAS.
https://orcid.org/0000-0002-5980-8472
E-mail: iren-kuznetsova@mail.ru

Oganes G. Lusinyan – Cand. Sci. (Eng.), Leading Engineer, ICEMR RAS.
https://orcid.org/0000-0002-5655-1747
E-mail: lusinyan.oganes@yandex.ru

Grigoriy Yu. Golberg – Dr. Sc. (Eng.), Leading Researcher, ICEMR RAS.
https://orcid.org/0000-0002-7968-3144
E-mail: gr_yu_g@mail.ru

Информация об авторах

Анатолий Афанасьевич Лавриненко – д.т.н., гл. науч. сотрудник, заведующий лабораторией Института проблем комплексного освоения недр им. академика Н.В.Мельникова Российской академии наук (ИПКОН РАН).
https://orcid.org/0000-0002-7955-5273
E-mail: lavrin_a@mail.ru

Ирина Николаевна Кузнецова – к.т.н., ст. науч. сотрудник ИПКОН РАН.
https://orcid.org/0000-0002-5980-8472
E-mail: iren-kuznetsova@mail.ru

Оганес Георгиевич Лусинян – к.т.н., вед. инженер ИПКОН РАН.
https://orcid.org/0000-0002-5655-1747
E-mail: lusinyan.oganes@yandex.ru

Григорий Юрьевич Гольберг – д.т.н., вед. науч. сотрудник ИПКОН РАН.
https://orcid.org/0000-0002-7968-3144
E-mail: gr_yu_g@mail.ru

Contribution of the authors

A.A. Lavrinenko – formulated the research concept, defined the study's objective, analyzed experimental data, and authored the manuscript.

I.N. Kuznetsova – prepared ore samples for investigation, conducted flotation experiments, conducted detachment force and zeta potential measurements, processed experimental data, and contributed to result discussions.

O.G. Lusinyan – prepared ore samples for investigation, conducted flotation experiments and calculations, and participated in result discussion.

G.Yu. Golberg – acquired and analyzed published data, analyzed experimental data, participated and contributed to result discussions.

Вклад авторов

А.А. Лавриненко – формулировка концепции работы, определение цели работы, анализ экспериментальных данных, написание статьи.

И.Н. Кузнецова – приготовление проб руды для проведения исследований, выполнение экспериментов по флотации, измерению силы отрыва и электрокинетического потенциала, обработка экспериментальных данных, участие в обсуждении результатов.

О.Г. Лусинян – приготовление проб руды для проведения исследований, выполнение экспериментов по флотации и расчетов, участие в обсуждении результатов.

Г.Ю. Гольберг – сбор и анализ литературы, анализ экспериментальных данных, участие в обсуждении результатов.

The article was submitted 22.05.2023, accepted for publication 24.07.2023
Статья поступила в редакцию 22.05.2023, подписана в печать 24.07.2023

UDC 546.73/546.74/66.046.8
https://doi.org/10.17073/0021-3438-2023-5-15-24

Research article
Научная статья

Production of nickel and cobalt metal powders under autoclave conditions

N.V. Belousova[1], **O.V. Belousov**[1,2], **R.V. Borisov**[1,2], **A.M. Zhizhaev**[2], **Ye.V. Tomashevich**[2]

[1] **Siberian Federal University**
79 Svobodnyi Prosp., Krasnoyarsk, 660041, Russia

[2] **Institute of Chemistry and Chemical Technology at the Siberian Branch of the Russian Academy of Sciences – Krasnoyarsk Science Center of the Siberian Branch of the Russian Academy of Sciences**
50/24 Akademgorodok, Krasnoyarsk, 660036, Russia

✉ Natalia V. Belousova (netmamba@mail.ru)

Abstract: This paper presents the results of studies on the reduction of dispersed cobalt and nickel metal powders from their salts in ammonia-alkaline aqueous solutions under hydrothermal autoclave conditions. A unified and environmentally friendly method for producing these powders has been developed. Hydrazine hydrate, with a 25–50 % excess of the stoichiometric ratio, was used as a reducing agent. This choice allows for obtaining metal phases that are chemically uncontaminated by decomposition products. The experiments determined the conditions for the quantitative reduction of cobalt (II) and nickel (II) ions from ammonia-alkaline aqueous solutions. The synthesis temperature for the dispersed phases ranged from 110 to 155 °C. It has been demonstrated that under the conditions used, the process is completed quantitatively within 60 min. Metal concentrations in the solutions were determined using atomic absorption spectroscopy. The results of the *X*-ray phase analysis confirm that cobalt forms in the HCP lattice, while nickel forms in the FCC lattice. No other phases, including *X*-ray amorphous phases, were observed. It was found that with an increase in the hydrothermal synthesis temperature from 110 to 155 °C, the specific surface area of cobalt increased by more than 1.5 times, and that of nickel black powders increased by approximately 2 times. Scanning electron microscopy revealed that cobalt is formed in the shape of lamellar particles with a lateral size of about 500 nm and a thickness of 50 nm, which aggregate into fractal structures. Nickel is represented by spherical particles arranged in chain-like structures. Using *X*-ray photoelectron spectroscopy, it was determined that the surface of the materials is covered with oxidized forms. The surface atomic concentration of cobalt (0) was approximately 2 %, while that of nickel (0) was about 25 %.

Keywords: nickel, cobalt, autoclaves, hydrothermal conditions, nanopowders, surface.

Acknowledgments: This research was conducted as part of the state assignment of the Institute of Chemistry and Chemical Technology of the SB RAS (project FWES-2021-0014). The authors also acknowledge the utilization of the equipment of the Krasnoyarsk Regional Center for Collective Use of FRC KSC SB RAS.

For citation: Belousova N.V., Belousov O.V., Borisov R.V., Zhizhaev A.M., Tomashevich Ye.V. Production of nickel and cobalt metal powders under autoclave conditions. *Izvestiya. Non-Ferrous Metallurgy.* 2023;29(5):15–24. https://doi.org/10.17073/0021-3438-2023-5-15-24

Получение металлических порошков никеля и кобальта в автоклавных условиях

Н.В. Белоусова[1], **О.В. Белоусов**[1,2], **Р.В. Борисов**[1,2], **А.М. Жижаев**[2], **Е.В. Томашевич**[2]

[1] **Сибирский федеральный университет**
660041, Россия, г. Красноярск, пр. Свободный, 79

[2] **Институт химии и химической технологии СО РАН – обособленное подразделение ФИЦ КНЦ СО РАН**
660036, Россия, г. Красноярск, Академгородок, 50/24

✉ Наталья Викторовна Белоусова (netmamba@mail.ru)

Аннотация: Представлены результаты исследований восстановления дисперсных металлических порошков кобальта и никеля из аммиачно-щелочных водных растворов их солей в гидротермальных автоклавных условиях. Отработана унифицированная,

экологически безопасная методика получения этих порошков. В качестве восстановителя применяли гидрат гидразина с 25–50 %-ным избытком от стехиометрического соотношения, который позволяет получать металлические фазы, химически не загрязненные продуктами разложения. В результате экспериментов установлены условия количественного восстановления ионов кобальта (II) и никеля (II) из аммиачно-щелочных водных растворов. Температуру синтеза дисперсных фаз варьировали в диапазоне от 110 до 155 °С. Показано, что в использованных режимах проведения процесс количественно завершается в течение 60 мин. Концентрации металлов в растворах определяли методами атомно-абсорбционной спектроскопии. Результаты рентгенофазового анализа подтвердили, что кобальт формируется в ГПУ-, а никель – в ГЦК-решетке, другие фазы, включая рентгеноаморфные, отсутствуют. Установлено, что с ростом температуры гидротермального синтеза от 110 до 155 °С удельная площадь поверхности кобальта увеличивается более чем в 1,5 раза, а порошков никелевой черни – примерно в 2 раза. Сканирующей электронной микроскопией показано, что кобальт формируется в виде пластинчатых частиц латеральным размером около 500 нм и толщиной 50 нм, которые агрегированы во фрактальные структуры. Никель представлен частицами сферической формы, упорядоченными в цепочкоподобные структуры. Методом рентгеновской фотоэлектронной спектроскопии установлено, что поверхность материалов покрыта окисленными формами. Поверхностная атомная концентрация кобальта (0) составила порядка 2 %, а никеля (0) – около 25 %.

Ключевые слова: никель, кобальт, автоклавы, гидротермальные условия, нанопорошки, поверхность.

Благодарности: Работа выполнена в рамках государственного задания Института химии и химической технологии СО РАН (проект FWES-2021-0014) с использованием оборудования Красноярского регионального центра коллективного пользования ФИЦ КНЦ СО РАН.

Для цитирования: Белоусова Н.В., Белоусов О.В., Борисов Р.В., Жижаев А.М., Томашевич Е.В. Получение металлических порошков никеля и кобальта в автоклавных условиях. *Известия вузов. Цветная металлургия*. 2023;29(5):15–24.
https://doi.org/10.17073/0021-3438-2023-5-15-24

Introduction

Serious attention to dispersed materials based on non-ferrous metals is warranted due to their properties, which are primarily of practical interest. Powders of nickel, cobalt, and their alloys have been and continue to be widely used in numerous vital areas of human activity, including metallurgy [1], heterogeneous catalysis [2; 3], materials science [4—6], medicine and biology [7], electronic and electrical engineering [6; 8], among others. In the paper [9], magnetic carbon materials containing nickel and cobalt are described for addressing environmental issues. Furthermore, the authors of the article [4] have presented information on the production of corrosion-resistant coatings based on these metals.

The specific requirements for the composition, dispersion ability, morphology, and other essential characteristics of functional materials are largely determined by their application spheres. Consequently, methods for producing these materials are actively under development and improvement. The body of research dedicated to addressing these issues is extensive. Classical approaches for obtaining highly dispersed nickel and cobalt powders, such as thermal decomposition or exposure to reducing gases like hydrogen, are well-established [6; 8; 10]. However, they come with a set of challenges, primarily associated with the difficulty of controlling the powders' dispersion ability due to the potential sintering of materials driven by diffusion processes. Maintaining the required temperature is a significant challenge in heterogeneous reduction to metal powders. This difficulty may arise from the heat generated during the reduction reaction, leading to localized overheating of specific surface areas and, consequently, the sintering of particles.

Enlargement processes in hydrothermal systems can be observed at lower temperatures, but spontaneous heating does not occur, especially with conventional convection heating methods [11].

Chemical precipitation of dispersed Ni and Co metal powders from aqueous solutions under the influence of potent reducing agents has been the focus of numerous studies. In the article [12], the potential for separating nickel and cobalt metal phases from their hot salt solutions using sodium hypophosphite is demonstrated. Several investigations have been dedicated to the reduction of Ni(II) and Co(II) salts from aqueous solutions using sodium tetrahydridoborate [13—15]. However, in these cases, it is essential to consider the possibility of metal powder contamination with decomposition products of sodium hypophosphite and sodium tetrahydridoborate, respectively. Such contamination is entirely unacceptable in various practical applications, such as heterogeneous catalysis.

The use of hydrazine hydrate as a reducing agent is highly appealing, as it guarantees the purity of the materials obtained. It's not surprising that occasional instances of using this reagent for producing dispersed metal powders, including nickel and cobalt, can be found

in the literature [16—19]. In [19], it was demonstrated that the reduction of mixtures of difficult-to-solubilize nickel and cobalt carbonates with hydrazine hydrate at 80—95 °C resulted in the formation of nanocrystalline powders of the respective metals.

The use of hydrometallurgical processes in open systems, despite their simplicity, is accompanied by several challenges, including inefficient reagent utilization and environmental pollution. The development of environmentally sustainable and efficient methods for producing dispersed materials based on non-ferrous metals with the necessary structural characteristics and properties is an urgent objective. This challenge can be addressed through autoclave technologies [17; 18].

The objective of this study is to develop a unified, environmentally friendly technique for obtaining dispersed cobalt and nickel metal powders and to investigate the structural parameters of the resulting materials.

Research methodology

In this study, we used high-purity aqueous ammonia (special purity grade 23-5; GOST 24147-80), $NiCl_2 \cdot 6H_2O$ (reagent grade), $CoCl_2 \cdot 6H_2O$ (reagent grade), potassium hydroxide (reagent grade), 64 % $N_2H_4 \cdot H_2O$ (reagent grade), and gaseous argon (Grade-3). Deionized water was prepared using the Direct-Q3 purification system (Millipore, USA). The experiments were conducted in laboratory fluoroplastic autoclaves with volumes ranging from 30 to 200 cm^3, the design of which is detailed in [17; 20; 21].

The synthesis of dispersed cobalt and nickel magnetic powders was carried out within a temperature range of 110 to 155 °C, following the procedure outlined in [17]. The choice of this temperature range is based on the consideration that at lower temperatures, the reduction processes may be hindered due to the possible formation of stable hydrazine complexes, while at higher temperatures, the system's pressure significantly increases.

The procedure involved placing a measured quantity of $CoCl_2 \cdot 6H_2O$ (or $NiCl_2 \cdot 6H_2O$) in a fluoroplastic liner and dissolving it in an aqueous solution of ammonium hydroxide. Subsequently, a 10 % sodium hydroxide solution and hydrazine hydrate (in excess of 30 % of the stoichiometry ratio) were added and stirred. Argon purging was used to remove air oxygen. Following this, the autoclave was sealed by securing it within a stainless-steel casing and then placed in a thermostat, where it was heated to the required temperature for a specified duration (60 min). The thermostat design allowed for vertical plane stirring. After the experiment, the autoclave was disassembled, the liquid phase was collected for analysis, and the solid phase was thoroughly washed with distilled water, dried at a temperature of 100 °C, and weighed. The residual concentration of cobalt or nickel ions in the solution was used to calculate the extent of metal reduction. Additionally, the obtained mass of the precipitate was compared to the calculated mass. The excess of the mass of synthesized powder over the calculated mass served as an indicator of the formation of oxidized forms of the metal (oxide, hydroxide).

The electron-microscopic analysis of materials was conducted using a scanning electron microscope TM4000 (Hitachi, Japan) equipped with a microanalysis system Quantax 70 (Bruker, Germany) operating in backscattered electrons mode, with an accelerating voltage of 20 keV. High-resolution electron microphotographs were obtained using a scanning electron microscope S5500 (Hitachi, Japan) in secondary electrons mode, with an accelerating voltage of 3 keV.

The specific surface area of the powders was determined through low-temperature nitrogen adsorption using an analyzer ASAP-2420 (Micromeritics, USA), at a $t = -195.75$ °C, applying the BET model.

X-ray diffractograms were recorded using a desktop diffractometer Proto AXRD (Proto Manufacturing, Canada) and CuK_α radiation. The recording was conducted in the angle range of $2\theta = 15°\div100°$, with a spacing of 0.02° and accumulation time at 2 sec point.

X-ray photoelectron spectra were registered using a spectrometer SPECS (SPECS GmbH — Surface Analysis and Computer Technology, Germany), equipped with a hemispherical energy analyzer PHOIBOS 150 MCD9 (SPECS GmbH). Monochromatic AlK_α radiation (1253.6 eV) from the anode of the *X*-ray tube was used for excitation. The transmittance energy of the energy analyzer was set at 20 eV for panoramic spectra or 10 eV for high-resolution spectra. Spectra data were processed using the CasaXPS software package. To correct for electrostatic charging, the maximum of the C 1s spectrum (285.0 eV) arising from hydrocarbon contaminants was utilized. High-resolution spectra were approximated using doublets of the asymmetric Gaussian—Lorentzian form, following Shirley subtraction of the nonlinear background.

The content of nickel and cobalt ions in the solutions was determined by atomic absorption spectroscopy using a spectrometer AAnalyst-400 (Perkin Elmer, USA).

Research results and discussion

The reduction process of nickel and cobalt salts by hydrazine hydrate, as demonstrated earlier [17], can be thermodynamically described by the following equations:

$$2CoCl_2 \cdot 6H_2O + N_2H_4 \cdot H_2O + 4NaOH = \\ = 2Co + 4NaCl + N_2 + 17H_2O, \quad (1)$$

$$2NiCl_2 \cdot 6H_2O + N_2H_4 \cdot H_2O + 4NaOH = \\ = 2Ni + 4NaCl + N_2 + 17H_2O. \quad (2)$$

According to the assumption proposed in [18; 22], the reduction of nickel and cobalt proceeds through the stage of formation of stable hydrazine complexes of the respective metals. These complexes are stable under normal conditions, and precipitation into the metallic state occurs at elevated temperatures.

Despite the use of closed systems, the quantitative progress processes (1) and (2) requires an excess of reducing agent, approximately 20 % above the stoichiometric ratio. This excess is necessary due to the potential oxidation of the reducing agent, which may occur because of the presence of oxygen in both the gas phase of the autoclave (owing to incomplete removal) and oxygen dissolved in the liquid phase.

It was observed that in ammonia-alkaline media, the reduction of nickel and cobalt at a temperature of 110 °C is completed within 1 h, while, as per [18], cobalt metal separation does not occur below t = 120 °C.

Specific surfaces of nickel and cobalt powders

Удельные поверхности порошков никеля и кобальта

Sample No.	Metal	t, °C	S_{surf}, m^2/g
1	Co	110	5.1
2		125	5.8
3		140	6.5
4		155	8.0
5	Ni	110	10.2
6		125	15.1
7		140	21.3
8		155	21.6

Under hydrothermal conditions in a closed system at t = 110 °C, it was found that the precipitation depth of cobalt metal is not less than 95 % with a 20 % excess of hydrazine hydrate from the stoichiometric ratio. With a 50 % excess of the reducing agent, the concentration of cobalt ions in the solution after metal precipitation, as determined by atomic absorption spectroscopy, is less than < 0.1 mg/L.

A similar situation is observed in the reduction process of nickel chloride (2). Increasing the synthesis temperature does not result in significant changes in product output, but it does influence the structural characteristics of the powders (see the table). The specific surface area of cobalt synthesized at t = 155 °C is nearly twice

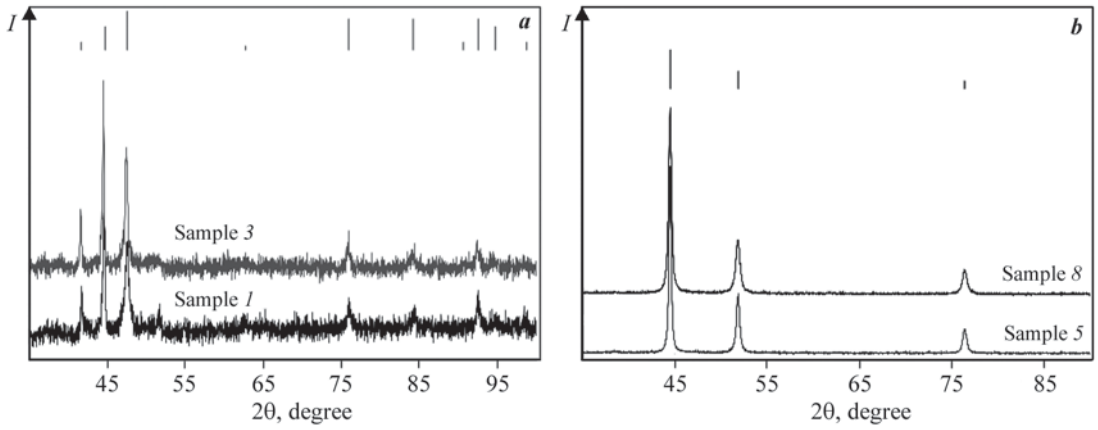

Fig. 1. Fragments of *X*-ray diffractograms of cobalt (***a***) and nickel (***b***) powders (see the table)

The stick diagrams of cobalt JCPDS 05-0727 (P63/mmc, a = 0.25031 nm, c = 0.40605 nm) and nickel JCPDS 65-2865 (FCC, a = 0.35240 nm) are shown above

Рис. 1. Фрагменты рентгеновских дифрактограмм порошков кобальта (***a***) и никеля (***b***) (см. таблицу)

Сверху показаны штрих-диаграммы кобальта JCPDS 05-0727 (P63/mmc, a = 0,25031 нм, c = 0,40605 нм) и никеля JCPDS 65-2865 (ГЦК, a = 0,35240 нм)

that of the material obtained at t = 110 °C. In the case of nickel, a similar situation arises: the surface areas of powders synthesized at 110 and 155 °C differ by approximately a factor of 2. This phenomenon is likely linked to the formation of a higher number of nuclei at higher temperatures due to an increased rate of reduction. This situation has been discussed in [23] concerning the preparation of noble metal nanoparticles for catalytic processes.

Based on the *X*-ray phase analysis of the precipitates, the material is composed of a single phase corresponding to the respective metal (see Fig. 1). Cobalt *X*-ray diffractograms exhibit metal reflections (JCPDS 05-0727) in the HCP modification, which is characteristic for the considered temperature range. The parameters for this phase are a = 0.25031 nm and c = 0.40605 nm. However, it's worth noting that [18] suggests that cobalt is formed from alkaline media with a metastable FCC lattice. In contrast, nickel adopts an FCC lattice with a cell parameter of a = 0.35240 nm. The *X*-ray diffractograms display peak broadening, which could be attributed, in part, to the material's dispersion.

It's worth noting that as a result of reactions (1) and (2), cobalt and nickel are generated in the modifications that are stable within these temperature ranges, specifically HCP and FCC, respectively.

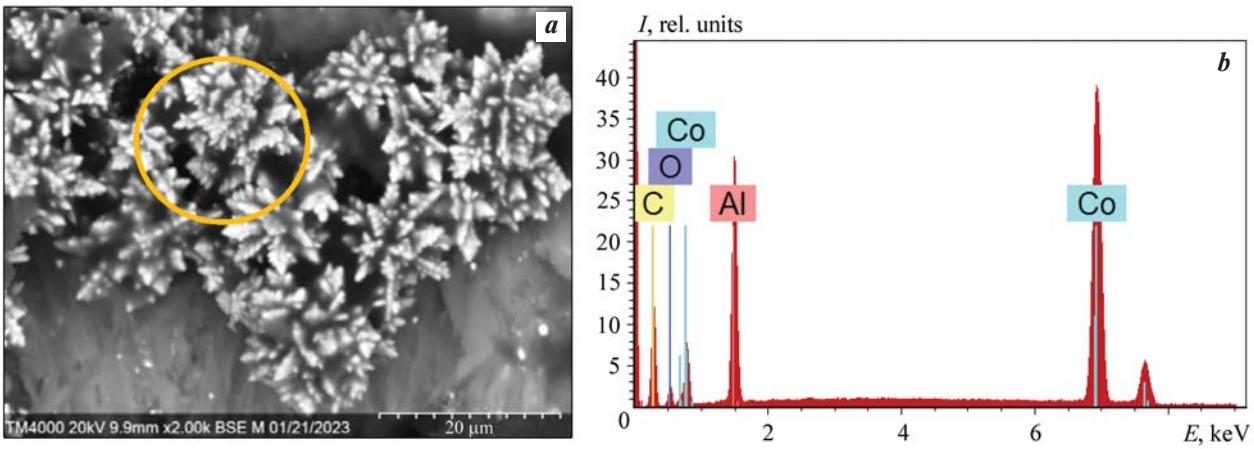

Fig. 2. SEM image (***a***) and energy dispersive spectrum for the imaged area (***b***) for cobalt (sample *3*, see the table)

Рис. 2. СЭМ-изображение (***a***) и энергодисперсионный спектр по отображаемой области (***b***) для кобальта (обр. *3*, см. таблицу)

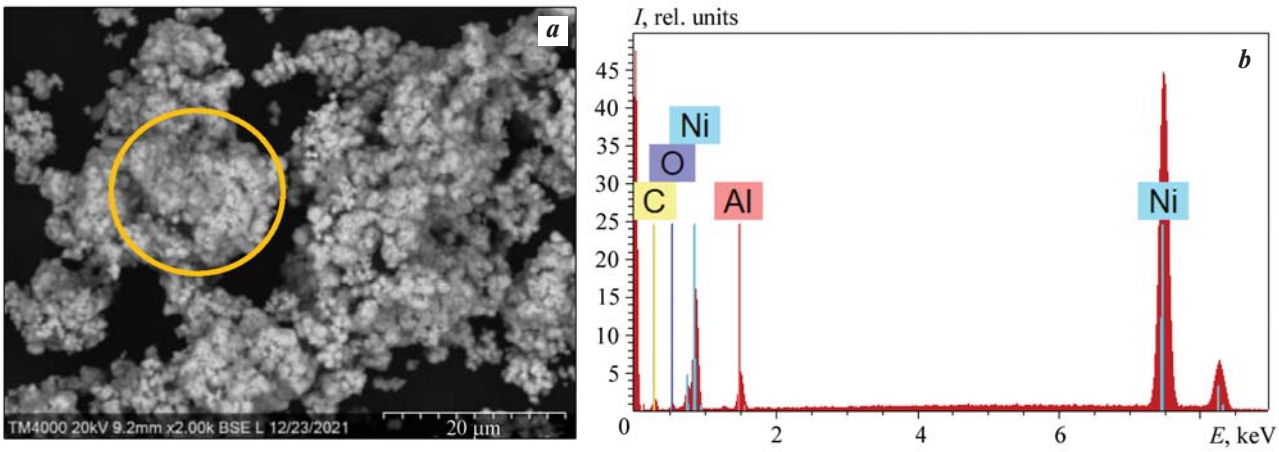

Fig. 3. SEM image (***a***) and energy dispersive spectrum for the imaged area (***b***) for nickel (sample *7*, see the table)

Рис. 3. СЭМ-изображение (***a***) и энергодисперсионный спектр по отображаемой области (***b***) для никеля (обр. *7*, см. таблицу)

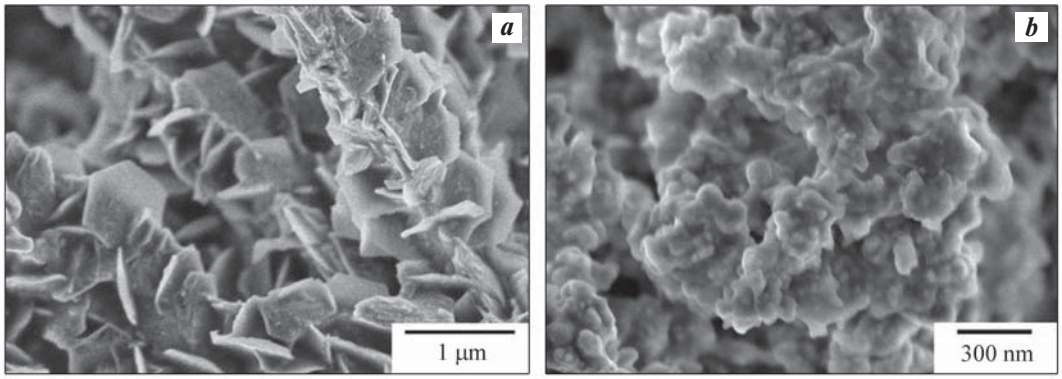

Fig. 4. SEM image of cobalt (***a***, sample *3*) and nickel (***b***, sample *7*)

Рис. 4. СЭМ-изображения кобальта (***a***, обр. *3*) и никеля (***b***, обр. *7*)

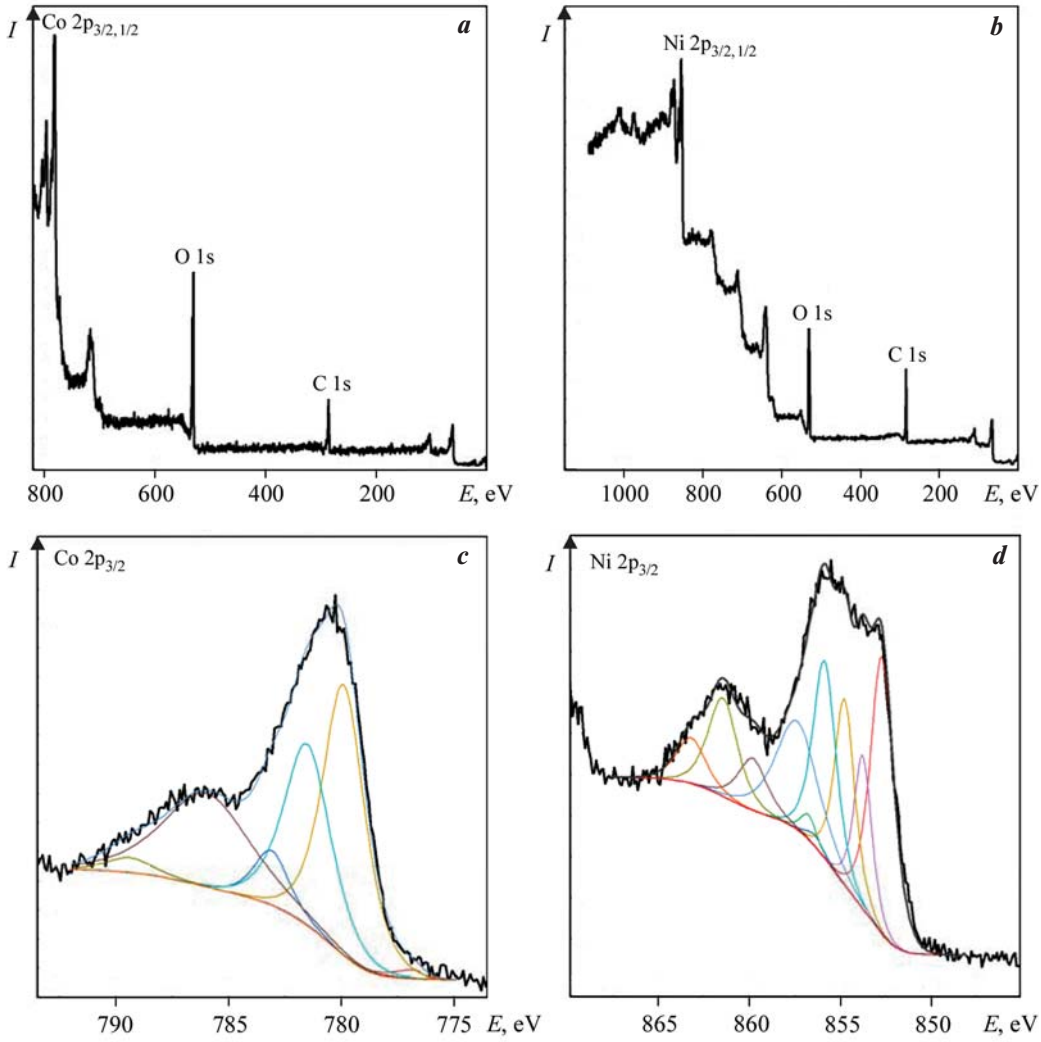

Fig. 5. *X*-ray photoelectron spectra after etching with argon ions for 3 min – panoramic spectra for cobalt (***a***) and nickel (***b***) and high-resolution spectra of Co $2p_{3/2}$ (***c***, sample *3*) and Ni $2p_{3/2}$ (***d***, sample *7*) lines

Рис. 5. Рентгеновские фотоэлектронные спектры после травления ионами аргона в течение 3 мин – обзорные для кобальта (***a***) и никеля (***b***), а также спектры высокого разрешения линий Co $2p_{3/2}$ (***c***, обр. *3*) и Ni $2p_{3/2}$ (***d***, обр. *7*)

Electron microscopic investigations have revealed that during reduction, cobalt forms fractal structures with dimensions of up to 10 μm (see Fig. 2). Upon closer examination, it becomes evident that these fractal agglomerates are composed of lamellar particles, including regular hexagonal shapes, with lateral dimensions of approximately 500 nm and a thickness of about 50 nm. Based on the *X*-ray spectral analysis (see Fig. 2), the material primarily consists of cobalt (94—98 at.% at various points) and oxygen (2—6 at.%), potentially indicating the presence of oxidized forms of the metal on the surface, likely in an amorphous state.

The morphology of nickel as revealed by scanning electron microscopy (Fig. 3), is markedly distinct. The particles have a shape closely resembling spheres and are arranged in chain structures, which become more distinguishable upon closer inspection (Fig. 4). According to the *X*-ray spectrometry analysis, the material primarily consists of nickel (97—100 at.% at various points) with a minimal oxygen content (up to 3 at.%).

The extent of oxidized products formed on the surface of nickel and cobalt metal, within a layer up to ~5 nm thick, can be estimated using *X*-ray photoelectron spectroscopy. Panoramic *X*-ray photoelectron spectra (Fig. 5, *a*, *b*) clearly exhibit the 1S lines of oxygen and carbon, as well as the 2p lines of cobalt and nickel, respectively. High-resolution spectra were subjected to decomposition (Fig. 5, *c*) using parameters and line shapes as presented in [24]. This decomposition identified components with energies of 780 eV or higher, corresponding to oxidized forms of Co(II), along with a component corresponding to the cobalt metal (778.1 eV). Calculations indicated that the total fraction of oxidized forms of cobalt on the surface is approximately 98 at.%. The nickel line, when scanned within the narrow $2p_{3/2}$ range (Fig. 5, *d*), can be decomposed into 8 components [24]. The peak at $E = 852.9$ eV corresponds to the nickel metal, while the other components align with the Ni(II)—OH multiplet set [25]. According to calculations, the fraction of nickel metal on the surface is 25 at.%.

Conclusion

1. A unified and environmentally friendly methodology for producing dispersed cobalt and nickel metal powders has been successfully developed.

2. It has been demonstrated that under autoclave hydrothermal conditions, cobalt and nickel are quantitatively reduced from their ammonia-alkaline salt solutions when hydrazine hydrate is used in excess of 50 % of the stoichiometric ratio.

3. XRF data confirm that cobalt adopts the HCP lattice, while nickel takes on the FCC lattice; no other phases were detected.

4. The *X*-ray photoelectron spectroscopy method revealed that the materials' surfaces are covered with oxidized forms of the metals.

5. Furthermore, it has been observed that as the temperature increases from 110 to 155 °C, the specific surface area of nickel increases by a factor of 2, and that of cobalt increases by 1.6 times.

References

1. Bolshakova O.V., Bolshakov S.V., Belousova N.V., Sinko A.V. Variations in cemenation reactions for different active Ni powders. *Tsvetnye Metally*. 2018;6:77—83. (In Russ.).
https://doi.org/10.17580/tsm.2018.06.11
Большакова О.В., Большаков С.В., Белоусова Н.В., Синько А.В. Изучение кинетики процесса цементации меди активным никелевым порошком. *Цветные металлы*. 2018;6:77—83.
https://doi.org/10.17580/tsm.2018.06.11
2. Yin W., Alekseeva M.V., Venderbosch R.H., Yakovlev V.A. Heeres H.J. Catalytic hydrotreatment of the pyrolytic sugar and pyrolytic lignin fractions of fast pyrolysis liquids using nickel based catalysts. *Energies*. 2020; 13(1):285.
https://doi.org/10.3390/en13010285
3. Lapidus A.L., Tsapkina M.V., Krylova A.Yu., Tonkonogov B.P. Bimetallic cobalt catalysts for the synthesis of hydrocarbons from CO and H_2. *Russian Chemical Reviews*. 2005;74(6):577—58.
https://doi.org/10.1070/RC2005v074n06ABEH001170
4. Li W., Hao J., Liu W., Mu S. Electrodeposition of nano Ni—Co alloy with (220) preferred orientation from choline chloride-urea: Electrochemical behavior and nucleation mechanism. *Journal of Alloys and Compounds*. 2021;853(5): 157158.
https://doi.org/10.1016/j.jallcom.2020.157158
5. Gürmen S., Stopić S., Friedrich B. Synthesis of nanosized spherical cobalt powder by ultrasonic spray pyrolysis materials. *Research Bulletin*. 2006;41(10):1882.
https://doi.org/10.1016/j.materresbull.2006.03.006
6. Khokhlacheva N.M., Lyushinskii A.V., Paderno V.N., Khokhlacheva T.G., Gryunval'd M.P., Bel'chikova M.E. Preparation of the mixtures of ultrafine powders of nickel, cobalt, and copper. *Soviet Powder Metallurgy and Metal Ceramics*. 1992;31(7):555—558.
https://doi.org/10.1007/BF00793429

7. Zakharov Yu.A., Eremenko N.K., Dodonov V.G., Obraztsova I.I., Eremenko A.N. Synthesis and properties of Co/Au and Ni/Au nanoparticles with core/shell structure. *Chemistry for Sustainable Development*. 2015;2: 177—182.
https://doi.org/10.15372/KhUR20150212
8. Huang Z., Liu F., Makuza B., Yu D., Guo X., Tian Q. Metal reclamation from spent lithium-ion battery cathode materials: directional conversion of metals based on hydrogen reduction. *ACS Sustainable Chemistry and Engineering*. 2022;10(2):756—765.
https://pubs.acs.org/doi/10.1021/acssuschemeng.1c05721
9. Kang J., Zhang H., Duan X., Sun H., Tan X., Liu S., Wang S. Magnetic Ni—Co alloy encapsulated N-doped carbon nanotubes for catalytic membrane degradation of emerging contaminants. *Chemical Engineering Journal*. 2019;362:251—261.
https://doi.org/10.1016/j.cej.2019.01.035
10. Nguyen T.H. Study on the kinetics of process for obtaining cobalt nanopowder by hydrogen reduction under isothermal conditions. *Izvestiya. Non-Ferrous Metallurgy*. 2021;27(1):49—56. (In Russ.).
https://doi.org/10.17073/0021-3438-2021-1-49-56
Нгуен Т.Х. Исследование кинетики процесса получения нанопорошка кобальта водородным восстановлением в изотермических условиях. *Известия вузов. Цветная металлургия*. 2021;27(1):49—56.
https://doi.org/10.17073/0021-3438-2021-1-49-56
11. Belousov O.V., Belousova N.V., Sirotina A.V. Solovyov L.A., Zhyzhaev A.M., Zharkov S. M., Mikhlin Y.L. Formation of bimetallic Au—Pd and Au—Pt nanoparticles under hydrothermal conditions and microwave irradiation. *Langmuir*. 2011;27:11697—11703.
https://doi.org/10.1021/la202686x
12. Brenner A., Riddell G.E. Deposition of nickel and cobalt by chemical reduction. *Journal of Research of the National Bureau of Standards*. 1947;39:385—395.
13. Zaharov Yu.A., Pugachev V.M., Dodonov V.G., Popova A.N., Kolmykov R.P., Rostovtsev G.A., Vasiljeva O.V., Zyuzyukina E.N., Ivanov A.V., Prosvirin I.P. Nanosize powders of transition metals binary systems. *Journal of Physics: Conference Series*. 2012;345:012024.
https://doi:10.1088/1742-6596/345/1/012024
14. Solov'eva A.Yu., Eremenko N.K., Obraztsova I.I., Eremenko A.N., Gubin S.P., Synthesis and optical properties of Fe@Au, Ni@Au bimetallic core—shell nanoparticles. *Russian Journal of Inorganic Chemistry*. 2018;63(4): 444—448.
https://doi.org/10.1134/S0036023618040204
Соловьева А.Ю., Еременко Н.К., Образцова И.И., Еременко А.Н., Губин С.П. Синтез и оптические свойства биметаллических наночастиц ядро—оболочка Fe@Au, Ni@Au. *Журнал неорганической химии*. 2018;63(4):416—420.
https://doi.org/10.1134/S0036023618040204
15. Zaharov Yu.A., Pugachev V.M., Bogomyakov A.S., Ovcharenko V.I., Korchuganova K.A., Russakov D.M., Kolmykov R.P. Influence of NicoreAushell nanoparticles' morphology on their magnetic properties. *Journal of Physical Chemistry C*. 2020;124(1):1008—1019.
https://doi.org/10.1021/acs.jpcc.9b07897
16. Logutenko O.A., Titkov A.I., Vorob'ev A.M. Shundrina I.K., Yukhin Yu.M. Lyakhov N.Z. Synthesis of nickel nanoparticles by the reduction of its salts using the modified polyol method in the presence of sodium polyacrylates with various molecular weights. *Russian Journal of General Chemistry*. 2018;88(2):288—294.
https://doi.org/10.1134/S1070363218020160
Логутенко О.А., Титков А.И., Воробьев А.Ю., Шундрина И.К., Юхин Ю.М., Ляхов Н.З. Синтез наночастиц никеля восстановлением его солей модифицированным полиольным методом в присутствии полиакрилатов натрия с различной молекулярной массой. *Журнал общей химии*. 2018;88(2): 311—318.
https://doi.org/10.1134/S1070363218020160
17. Belousov O.V., Borisov R.V., Romanchenko A.S., Belousova N.V., Zeer G.M. Autoclave synthesis of finely divided nickel powders. *Russian Journal of Inorganic Chemistry*. 2021;66(10):1463—1468.
https://doi.org/ 10.31857/S0044457X21100032
Белоусов О.В., Борисов Р.В., Белоусова Н.В., Зеер Г.М., Романченко А.С. Автоклавный синтез высокодисперсных порошков никеля. *Журнал неорганической химии*. 2021;66(10):1380—1386.
https://doi.org/ 10.31857/S0044457X21100032
18. Li Y.D., Li L.Q., Liao H.W., Wang H.R. Preparation of pure nickel, cobalt, nickel—cobalt and nickel—copper alloys by hydrothermal reduction. *Journal of Materials Chemistry*. 1999;9:2675—2677.
https://doi.org/10.1039/A904686K
19. Lapsina P., Popova A., Vladimirov A., Kagakin E., Sachkov V. Effect of synthesis conditions on size characteristics of nickel and cobalt nanostructured powders. *Key Engineering Materials*. 2016;683: 181—186.
https://doi.org/10.4028/www.scientific.net/KEM.683.181
20. Belousova N.V., Belousov O.V., Borisov R.V., Akimenko A.A. Autoclave dissolution of platinum metals in hydrochloric acid oxidizing media. *Russian Journal of Non-Ferrous Metals*. 2021;62:668—674.
https://doi.org/10.3103/S1067821221060043
Белоусова Н.В., Белоусов О.В., Борисов Р.В., Акименко А.А. Автоклавное растворение платиновых ме-

таллов в солянокислых окислительных средах. *Известия вузов. Цветная металлургия*. 2021;27(5):50—57. https://doi.org/10.17073/0021-3438-2021-5-50-57

21. Belousova N.V., Belousov O.V., Borisov R.V. Dissolution of metallic iridium powders in hydrochloric acid oxidizing media. *Tsvetnye Metally*. 2022;(8):40—45. (In Russ). https://doi.org/10.17580/tsm.2022.08.05
Белоусова Н.В., Белоусов О.В., Борисов Р.В. Растворение порошков металлического иридия в кислых окислительных средах. *Цветные металлы*. 2022;8:40—45. https://doi.org/10.17580/tsm.2022.08.05
22. Li Y.D., Li C.W., Wang H.R., Li L. Q., Qian Y.T. Preparation of nickel ultrafine powder and crystalline film by chemical control reduction. *Materials Chemistry and Physics*. 1999;59(1):88—90. https://doi.org/10.1016/S0254-0584(99)00015-2
23. Xia X., Xie S., Liu M., Pen, H.C., Lu N., Wang J., Kim M.J., Xia Y. On the role of surface diffusion in determining the shape or morphology of noble-metal nanocrystals. *Proceedings of the National Academy of Sciences*. 2013;110:6669—6673. https://doi.org/10.1073/pnas.1222109110
24. Biesinger M.C., Payne B.P., Grosvenor A.P., Lau L.W., Gerson A.R., Smart R.S.C. Resolving surface chemical states in XPS analysis of first row transition metals, oxides and hydroxides: Cr, Mn, Fe, Co and Ni. *Applied Surface Science*. 2011;257(7):2717—2730. https://doi.org/10.1016/j.apsusc.2010.10.051
25. Payne B.P., Biesinger M.C., McIntyre N.S. Use of oxygen/nickel ratios in the XPS characterisation of oxide phases on nickel metal and nickel alloy surfaces. *Journal of Electron Spectroscopy and Related Phenomena*. 2012;185(5-7): 159—166. https://doi.org/10.1016/j.elspec.2012.06.008

Information about the authors

Natalia V. Belousova – Dr. Sci. (Chem.), Prof., Head of the Department of Metallurgy of Non-Ferrous Metals of Siberian Federal University (SFU).
https://orcid.org/0000-0002-1355-7399
E-mail: netmamba@mail.ru

Oleg V. Belousov – Dr. Sci. (Chem.), Leading Researcher of the Laboratory of Hydrometallurgical Processes of the Institute of Chemistry and Chemical Technology of the Sibirian Branch of the Russian Academy of Sciences (ICCT SB RAS), Professor of the Department of Metallurgy of Non-Ferrous Metals of SFU.
https://orcid.org/0000-0001-7778-5393
E-mail: ov_bel@icct.ru

Roman V. Borisov – Cand. Sci. (Chem.), Researcher of the Laboratory of Hydrometallurgical Processes of ICCT SB RAS, Associate Professor of the Department of Mineral Processing of SFU.
https://orcid.org/0000-0002-6137-0975
E-mail: roma_boris@list.ru

Anatoly M. Zhizhaev – Cand. Sci. (Eng.), Leading Researcher of the Laboratory of Physical and Chemical Research Methods of Materials of ICCT SB RAS.
https://orcid.org/0000-0002-1447-4050
E-mail: zhyzhaev@icct.ru

Yevgeny V. Tomashevich – Cand. Sci. (Chem.), Senior Researcher of the Laboratory of Hydrometallurgical Processes of ICCT SB RAS.
https://orcid.org/0000-0003-0273-3200
Email: yetomash@gmail.com

Информация об авторах

Наталья Викторовна Белоусова – д.х.н., проф., заведующая кафедрой металлургии цветных металлов Сибирского федерального университета (СФУ).
https://orcid.org/0000-0002-1355-7399
E-mail: netmamba@mail.ru

Олег Владиславович Белоусов – д.х.н., ведущий научный сотрудник лаборатории гидрометаллургических процессов Института химии и химической технологии Сибирского отделения Российской академии наук (ИХХТ СО РАН), профессор кафедры металлургии цветных металлов СФУ.
https://orcid.org/0000-0001-7778-5393
E-mail: ov_bel@icct.ru

Роман Владимирович Борисов – к.х.н., научный сотрудник лаборатории гидрометаллургических процессов ИХХТ СО РАН, доцент кафедры обогащения полезных ископаемых СФУ.
https://orcid.org/0000-0002-6137-0975
E-mail: roma_boris@list.ru

Анатолий Михайлович Жижаев – к.т.н., ведущий научный сотрудник лаборатории физико-химических методов исследования материалов ИХХТ СО РАН.
https://orcid.org/0000-0002-1447-4050
E-mail: zhyzhaev@icct.ru

Евгений Владимирович Томашевич – к.х.н., старший научный сотрудник лаборатории гидрометаллургических процессов ИХХТ СО РАН.
https://orcid.org/0000-0003-0273-3200
E-mail: yetomash@gmail.com

Contribution of the authors

N.V. Belousova – conceptualization, article writing.

O.V. Belousov – methodology development, article writing.

R.V. Borisov – *X*-ray phase analysis, graphic material preparation, article writing.

A.M. Zhizhaev – participation in result discussion, electron microscopic studies.

Ye.V. Tomashevich – *X*-ray photoelectron spectroscopy research.

Вклад авторов

Н.В. Белоусова– определение цели работы, написание статьи.

О.В. Белоусов – разработка методики, написание статьи.

Р.В. Борисов – проведение рентгенофазового анализа, подготовка графического материала, написание статьи.

А.М. Жижаев – участие в обсуждении результатов, проведение электронно-микроскопических исследований.

Е.В. Томашевич – проведение исследований методом рентгенофотоэлектронной спектроскопии.

The article was submitted 03.05.2023, revised 21.08.2023, accepted for publication 23.08.2023

Статья поступила в редакцию 03.05.2023, доработана 21.08.2023, подписана в печать 23.08.2023

UDC 669.849 : 669.018.44 : 669.24
https://doi.org/10.17073/0021-3438-2023-5-25-33

Research article
Научная статья

Oxidative leaching of rhenium from grinding waste of rhenium-containing superalloys

I.E. Targanov, M.A. Solodovnikov, I.D. Troshkina

Mendeleev University of Chemical Technology of Russia
9 Miusskaya Sq., Moscow, 125047, Russia

✉ Irina D. Troshkina (troshkina.i.d@muctr.ru)

Abstract: The study investigated the feasibility of oxidative leaching rhenium in the presence of hydrochloric acid from machining waste (grinding waste) derived from products made of ZhS-32VI, a nickel-based heat-resistant alloy containing rhenium. This was achieved through agitation leaching process. The grinding waste fraction size of –0.071 mm, which accounted for the highest yield (49.2 wt.%), was utilized in the experiments. The rhenium leaching process was conducted in two variations: in the first option, grinding waste was mixed with a hydrochloric acid solution at ~100 °C, followed by the addition of hydrogen peroxide to the leaching solution after it had cooled; in the second option, leaching was performed using a hydrochloric acid solution with the gradual addition of hydrogen peroxide solution. The highest degree of rhenium leaching (91.0 %) was achieved in the first option. In this case, the initial concentration of hydrochloric acid was 8M, and the molar ratio of the added reagents was $\nu(HCl)$: $\nu(H_2O_2)$ = 2.7 : 1.0. The kinetics of nickel leaching using a 6M hydrochloric acid solution at 70 °C, with a solid-to-liquid phase ratio of 1 g : 50 mL, was also examined. The analysis of the kinetic data, processed using the "contracting sphere," Ginstling–Brounshtein, and Kazeev–Erofeev models, indicates that the nickel leaching process occurs within the kinetic region. Additionally, the kinetics of rhenium leaching from the solid residue obtained after the hydrochloric acid leaching of nickel from grinding waste was investigated. Employing the same kinetic models to analyze the data, it was determined that the limiting stage of this process involves the diffusion of hydrogen peroxide within the rhenium-containing solid residue.

Keywords: rhenium, nickel, superalloys, grinding waste, leaching, hydrochloric acid, oxidizing agent, kinetics.

For citation: Targanov I.E., Solodovnikov M.A., Troshkina I.D. Oxidative leaching of rhenium from grinding waste of rhenium-containing superalloys. *Izvestiya. Non-Ferrous Metallurgy.* 2023;29(5):25–33. https://doi.org/10.17073/0021-3438-2023-5-25-33

Окислительное выщелачивание рения из шлифотходов ренийсодержащих суперсплавов

И.Е. Тарганов, М.А. Солодовников, И.Д. Трошкина

Российский химико-технологический университет им. Д.И. Менделеева
125047, Россия, г. Москва, Миусская пл., 9

✉ Ирина Дмитриевна Трошкина (troshkina.i.d@muctr.ru)

Аннотация: В агитационном режиме исследована возможность окислительного выщелачивания рения в присутствии соляной кислоты из отходов механической обработки (шлифотходов) изделий из Re-содержащего жаропрочного сплава ЖС-32ВИ на основе никеля. Использовали фракцию шлифотходов –0,071 мм с наибольшим выходом (49,2 мас.%). Процесс извлечения рения осуществляли в двух вариантах: в первом – шлифотходы контактировали с раствором соляной кислоты при температуре ~100 °С, после охлаждения раствора выщелачивания в него добавляли раствор пероксида водорода; во втором – выщелачивание проводили с применением раствора соляной кислоты с порционным добавлением раствора пероксида водорода. Наибольшее значение степени извлечения рения (91,0 %) наблюдалось при выщелачивании в первом варианте, начальная концентрация соляной кислоты составила 8М, мольное соотношение добавляемых реагентов – $\nu(HCl)$: $\nu(H_2O_2)$ = 2,7 : 1,0. Была изучена кинетика выщелачивания никеля раствором соляной кислоты (6М) при температуре 70 °С и соотношении фаз шлифотход : раствор, рав-

ном 1 г : 50 мл. Анализ обработки кинетических данных с использованием моделей «сжимающейся сферы», Гинстлинга–Броунштейна и Казеева–Ерофеева позволяет утверждать, что процесс выщелачивания никеля протекает в кинетической области. Исследована кинетика выщелачивания рения из твердого остатка солянокислого выщелачивания никеля из шлифотходов. Применение для обработки данных тех же кинетических моделей позволяет выделить диффузию пероксида водорода в ренийсодержащем твердом остатке как лимитирующую стадию.

Ключевые слова: рений, никель, суперсплавы, шлифотходы, выщелачивание, соляная кислота, окислитель, кинетика.

Для цитирования: Тарганов И.Е., Солодовников М.А., Трошкина И.Д. Окислительное выщелачивание рения из шлифотходов ренийсодержащих суперсплавов. *Известия вузов. Цветная металлургия*. 2023;29(5):25–33.
https://doi.org/10.17073/0021-3438-2023-5-25-33

Introduction

The annually increasing global demand for high-tech materials, including rare elements, underscores the importance of recycling secondary raw materials. One such rare element is rhenium, which is extracted from primary raw materials solely as a by-product [1; 2]. Rhenium's main natural sources encompass sulfide molybdenum and copper ores, polymetallic uranium ores, and the fumarole gases of the Kudryavy Volcano on Iturup Island [3]. Depletion projections for rhenium reserves are on par with those for other non-ferrous and rare metals, whose resources are anticipated to be depleted within the next 100—110 years [2]. Consequently, it is imperative to develop and enhance recycling technologies for rhenium.

According to forecasts [4], the demand for rhenium in Russia is expected to reach 20 tons/year by 2032 and 35 tons/year by 2064.

The primary utilization of rhenium (78 %) occurs in the production of superalloys used for aircraft jet engines and turbines to generate electricity, where rhenium plays a vital role as an alloying element [5; 6]. Nickel-based superalloys exhibit exceptional oxidation resistance and mechanical strength. Substantial enhancements in their mechanical properties at high temperatures have been achieved through the careful control of material structure, incorporating alloying elements like rhenium, ruthenium, and hafnium [7; 8]. The addition of Re to these superalloys creates solid solution strengthening of the matrix, significantly improving heat resistance. However, it's worth noting that the cost of adding rhenium, for example, at 3 wt.% in the CMSX-4 alloy, accounts for approximately 60 % of the alloy's total cost [9; 10].

Monocrystalline rhenium-containing superalloys based on nickel are predominantly employed [6; 10—12].

The total waste generated from rhenium-containing heat-resistant nickel alloys, primarily consisting of discarded parts from gas turbine engines, was estimated to be 25—35 tons/year in the Russian Federation in 2012 [13]. Assuming a rhenium content of 3 %, this amounts to 0.75—1.0 tons/year of recoverable rhenium.

Existing technologies for processing waste form nickel-based heat-resistant alloys can be categorized into two groups: pyrometallurgical and hydrometallurgical [6; 14; 15]. Pyrometallurgical methods encompass direct waste melting and oxidative thermal methods [16], while hydrometallurgical approaches are based on electrochemical processes (anodic dissolution) [12; 17] and methods involving the decomposition of waste in acid solutions. The choice of processing technology depends on the type of raw material (solid parts or waste from mechanical processing, such as grinding waste) and the availability of specialized equipment like vacuum furnaces and electrolysis cells, among others.

Methods based on waste decomposition using acid solutions can involve both the removal of the alloy base and direct oxidative leaching to extract rhenium into solution. Leaching agents like mineral acids and their mixtures, in the presence of an oxidizing agent, can be employed for efficient rhenium leaching. Nitrate processing of multi-component alloys has proven effective [14], although the presence of nitrate ions in solutions can complicate subsequent sorption of rhenium. In a separate study [18], rhenium was leached using "aqua regia". When sulfuric acid is used, it becomes possible to leach the alloy base, nickel [19], followed by the addition of an oxidizing agent to isolate rhenium, or by using a mixture of sulfuric acid with an oxidizing agent like hydrogen peroxide for direct rhenium extraction into solution [14].

The high content of nickel and cobalt in grinding waste, both valuable non-ferrous metals, justifies the use of hydrochloric acid leaching during their comprehensive processing. In chloride environments, it's possible to separate these elements due to their similar chemical properties, requiring fewer steps in the preparation of the leaching solution [20].

The objective of this study is to establish the patterns of oxidative leaching of rhenium using hydrochloric

acid solutions from grinding waste derived from a rhenium-containing nickel-based superalloy.

Research methodology

The focus of this study was the grinding waste derived from the ZhS32-VI superalloy, which exhibits the following elemental composition, wt.%: 1.5 Re; 9.0 Co; 8.5 W; 5.9 Al; 4.9 Cr; 4.0 Ta; 1.6 Nb; 1.0 Mo; 0.15 C; 0.02 V; 0.025 Ce, 60.0 Ni. The particle size distribution of this waste material is summarized in Table 1.

The grinding waste with the highest weight fraction (49.2 wt.%), specifically with a particle size of −0.071 mm (as shown in Table 1), was selected for use in the study.

The choice of this finer particle size is based on its larger specific surface area and higher mass yield, making it a preferred option for selecting a hydrometallurgical processing method. This method includes the decomposition of waste using hydrochloric acid solutions, in the presence of an oxidizing agent, specifically a 30 % H_2O_2 solution.

In order to ensure the purity of the grinding waste and eliminate contaminants such as glycol, mineral oils, lubricating additives, surfactants, corrosion inhibitors, and rags, which may be present due to the use of various lubricants and coolants during machining workpieces, the grinding waste from rhenium-containing superalloys underwent a cleaning process. This involved washing the waste with hot water (~90 °C) followed by drying prior to conducting the experiments.

A sample of the grinding waste was brought into contact with a hydrochloric acid solution at various phase ratios of solid to liquid, ranging from 1 : 50 to 1 : 100 (g : mL), under agitation. A mixing speed of 200 min^{-1} was selected, considering that the grinding waste particles were suspended and thoroughly mixed while ensuring a continuous flow of the solution around them. Depending on the specific experiment, the reaction mixture was heated and leached at a temperature of 100 °C for 60 minutes. After cooling the reaction mixture, hydrogen peroxide solution (*I*) was added to it batchwise. The experimental leaching setup consisted of a flask heater containing a three-neck flask equipped with a reflux condenser, and mixing was facilitated using an overhead stirrer.

When conducting experiments without heating to prevent spontaneous heating and potential hydrogen peroxide decomposition, the process took place within a thermostatically controlled jacketed cell that was actively cooled using running water. The oxidizing agent was added to the cooled reaction mixture batchwise, following each hour of the experiment (*II*). Stirring was maintained at a speed of 200 min^{-1}. Periodically, throughout the experiment, samples of the solution were withdrawn and subjected to analysis for rhenium content using the photometric method with ammonium thiocyanate. In order to ensure an adequate concentration of hydrochloric acid (with at least a 30 % excess), the selection was made considering theoretical calculations based on the chemical reactions of the acid with the constituent metals of the alloy and those components of the alloy that, as indicated in published data, are reactive with it.

The kinetics of nickel leaching from grinding waste using a hydrochloric acid solution was investigated under agitation in a thermostated reactor for a duration of 15 h at 70 °C. A sample of grinding waste was brought into contact with a 6M hydrochloric acid solution at a solid to liquid phase ratio of 1 : 50 (g : mL). At specific time intervals, samples of the solution were obtained and analyzed for nickel content using the titrimetric method with EDTA-Na_2.

The kinetics of rhenium leaching from the concentrate formed after the removal of nickel from waste using a solution of hydrochloric acid and hydrogen peroxide was investigated under agitation mode. The experiments were conducted in a thermostatically controlled cell that was actively cooled by running water. A sample of rhenium concentrate was brought into contact with a hydrochloric acid solution initially at a concentration of 2M, with a solid-to-liquid phase ratio of 1 : 250 (g : mL). The oxidizing agent was added in 1 ml increments every 30 min. At specific time intervals, samples of the solution were extracted and subjected to analyzed for Re content.

Table 1. **Particle size distribution of grinding waste of ZhS32-VI superalloy**

Таблица 1. Фракционный состав шлифотходов суперсплава ЖС32-ВИ

Particle size, mm	Yield, wt.%
+2.0	3.1
−2.0+1.2	0.7
−1.2+1.0	2.0
−1+0.5	1.1
−0.5+0.1	24.7
−0.1+0.071	19.2
−0.071	49.2

The degree of saturation of the solution with rhenium (or nickel), $\alpha_{(Me)}$, was calculated using the following equation:

$$\alpha_{(Me)} = C_{(Me)}V_{solution} /(\omega_{(Me)}m_{sample}),$$

where $C_{(Me)}$ represents the current concentration of the metal (rhenium or nickel), g/L; $V_{solution}$ stands for the solution volume, L; $\omega_{(Me)}$ denotes the weight fraction of the metal (rhenium or nickel) in grinding waste; m_{sample} is the weight of the sample, g.

Results and discussion

Rhenium metal undergoes a reaction with hydrogen peroxide to produce rhenium acid as described by the following equation:

$$2Re + 7H_2O_2 \rightarrow 2HReO_4 + 6H_2O.$$

In preliminary experiments, it was determined that quantitatively extracting rhenium into solution is not achievable solely by using a solution of hydrogen peroxide, without first removing the nickel component, which is a fundamental constituent of the superalloy.

Table 2 provides a summary of the data pertaining to the oxidative leaching of rhenium from pre-washed grinding waste originating from a rhenium-containing superalloy. These leaching experiments were conducted in hydrochloric acid solutions with the aid of hydrogen peroxide as an oxidizing agent, under various leaching methods and conditions.

The most effective extraction of rhenium into solution occurs when the waste is heated in an acidic solution with the addition of an oxidizing agent after the mixture has been cooled to room temperature. It appears that the initial removal of the majority of the alloy by preheating it in hydrochloric acid solutions a temperature of 100 °C for 1 hour facilitates better access of the oxidizing agent to the rhenium within the alloy.

Furthermore, elevating the concentration of the hydrochloric acid solution from 6M to 8M during the preheating step and maintaining it during the leaching process results in a 7.5 % increase in the degree of rhenium extraction into solution, followed by the subsequent addition of an oxidizing agent.

The extent of nickel leaching, which constitutes the base of the superalloy, when treated with a 6M hydrochloric acid solution at a temperature of 70 °C over time, is graphically depicted in Fig. 1.

As illustrated in in Fig. 1, it's evident that equilibrium is achieved after ~600 min.

In order to pinpoint the limiting stage of the nickel leaching process with the hydrochloric acid solution, the kinetic data were subjected to analysis using both kinetic and diffusion mathematical models (Fig. 2, Table 3).

The "contracting sphere" model, also known as the Gray—Weddington equation [22], is used to describe processes where a reaction takes place on the surface of a spherical solid that loses mass and diminishes in size

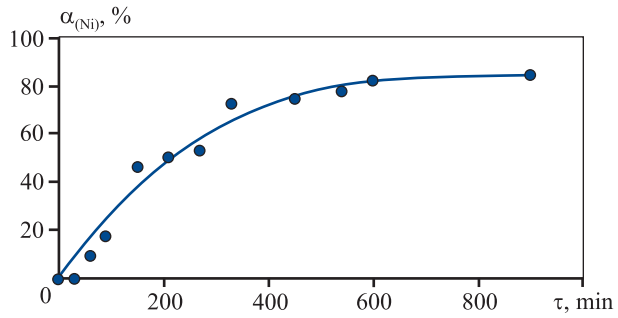

Fig. 1. Temporal variation in nickel leaching using a 6M hydrochloric acid solution at 70 °C

Рис. 1. Зависимость степени выщелачивания никеля солянокислым раствором (6М) при температуре 70 °С от времени

Table 2. **Hydrochloric acid oxidative leaching of rhenium**

Таблица 2. Солянокислое окислительное выщелачивание рения

Initial concentration of HCl	Procedure conditions	Mole ratio $\nu(HCl) : \nu(H_2O_2)$	Phase ration, g : mL	$\alpha_{(Re)}$, %
8M	*I*	2.7 : 1.0	1 : 130	91.0
6M	*I*	2.0 : 1.0	1 : 130	83.5
6M	*I*	1.4 : 1.0	1 : 50	71.4
6M	*II*	2.4 : 1.0	1 : 100	68.5
8M	*II*	6.6 : 1.0	1 : 50	47.0

Table 3. **Kinetic characteristics of hydrochloric acid leaching of nickel from grinding waste obtained using various models**

Таблица 3. Кинетические характеристики солянокислого выщелачивания никеля из шлифотходов, полученные при использовании различных моделей

Equation of "contracting sphere"		Ginstling–Brounshtein equation		Kazeev–Erofeev equation	
$1-(1-\alpha)^{1/3}=k\tau$		$1-(2/3)\alpha-(1-\alpha)^{2/3}=k\tau$		$\ln[-\ln(1-\alpha)]=n\ln\tau+\ln k_\tau$	
$k\cdot10^4$, min^{-1}	R^2	$k\cdot10^4$, min^{-1}	R^2	n	R^2
8	0.933	3	0.883	1.56	0.849

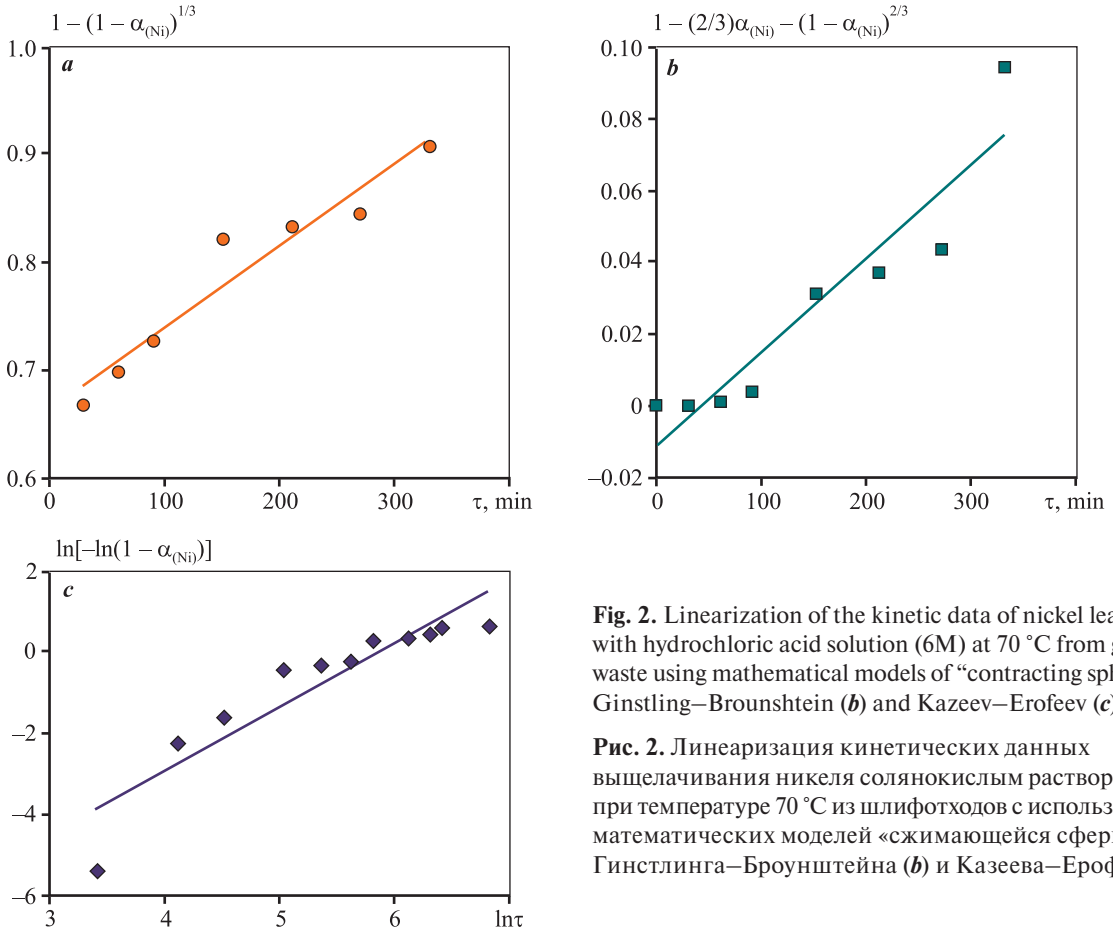

Fig. 2. Linearization of the kinetic data of nickel leaching with hydrochloric acid solution (6M) at 70 °C from grinding waste using mathematical models of "contracting sphere" (***a***), Ginstling–Brounshtein (***b***) and Kazeev–Erofeev (***c***)

Рис. 2. Линеаризация кинетических данных выщелачивания никеля солянокислым раствором (6М) при температуре 70 °С из шлифотходов с использованием математических моделей «сжимающейся сферы» (***a***), Гинстлинга–Броунштейна (***b***) и Казеева–Ерофеева (***c***)

during the reaction, leading to the formation of an undissolved porous layer of product. This equation is particularly suitable for processes occurring within the kinetic range of reactions and is expressed as follows:

$$1 - (1 - \alpha)^{1/3} = k\tau, \quad (1)$$

where α represents the leaching rate (as a fraction), k is the rate constant of the reaction, min^{-1}, and τ is the time, min.

In cases where a dense, non-porous product layer is formed, the Ginstling—Brounshtein equation is employed [20, 22]:

$$1 - (2/3)\alpha - (1 - \alpha)^{2/3} = k\tau. \quad (2)$$

The use of the generalized kinetic Kazeev—Erofeev equation helps determine the limiting stage of the process and estimate the values of the n index in the equation:

$$\alpha = 1 - \exp(-K\tau^n), \quad (3)$$

where K and n are the kinetic parameters. This equation serves as a function of the likelihood of the degree of transformation, applicable to both topochemical reactions and reactions of different types.

In its doubly logarithmic form, Eq. (3) is linearized as follows:

$$\ln[-\ln(1 - \alpha)] = n\ln\tau + \ln k_\tau. \quad (4)$$

Based on the results of the mathematical analysis of kinetic data for the leaching of nickel from the grinding waste of rhenium-containing superalloys, it is evident that the data are more suitably linearized by employing the "contracting sphere" equation. Furthermore, the examination of mathematical processing using the Kazeev—Erofeev equation has allowed us to ascertain that the value of the $n = 1.56$. This value indicates that the leaching of nickel follows a kinetic reaction in the process.

Regarding the leaching of rhenium from the concentrate formed after the removal of nickel, which is the primary component of the superalloy, this process was conducted using a solution of hydrogen peroxide in the presence of hydrochloric acid. The degree of rhenium leaching from the concentrate, with the addition of a 2M hydrochloric acid solution and periodic introduction of hydrogen peroxide (Fig. 3), exhibits a characteristic convex shape over time and reaches a plateau within ~1 h.

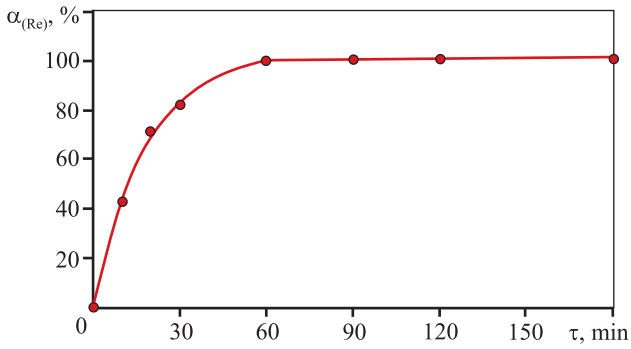

Fig. 3. Temporal variation of rhenium leaching using hydrogen peroxide (30 %) in the presence of hydrochloric acid (2M)

Рис. 3. Зависимость степени выщелачивания рения пероксидом водорода (30 %) в присутствии соляной кислоты (2M) от времени

The degree of rhenium leaching rate into the solution achieved a level of ≥99 %.

In order to identify the rate-limiting stage of the process, the kinetic data were subjected to analysis using the previously described kinetic and diffusion mathematical models (Fig. 4, Table 4).

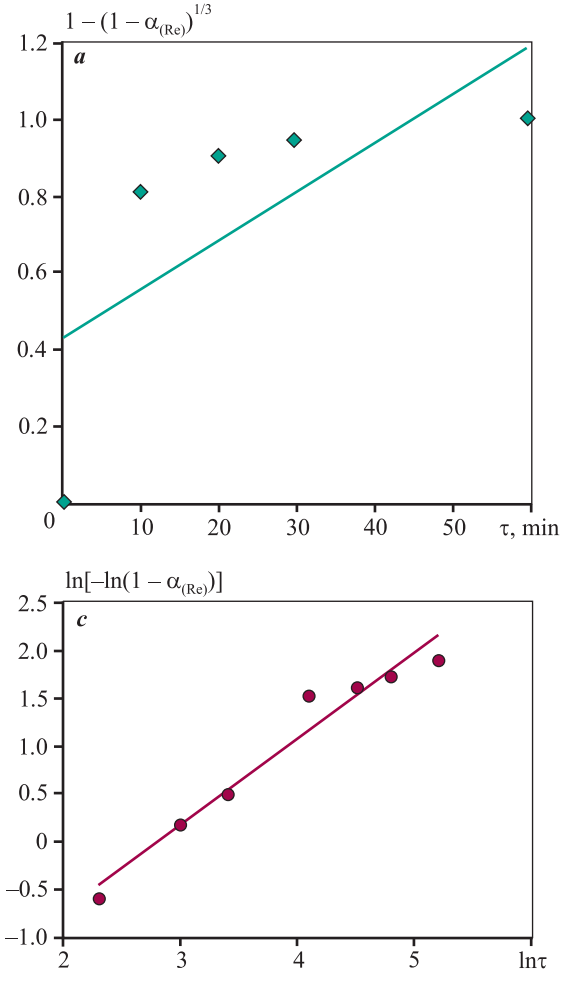

Fig. 4. Linearization of kinetic data of rhenium leaching from concentrate using "contracting sphere" (***a***), Ginstling-Brounshtein (***b***) and Kazeev–Erofeev (***c***) mathematical models

Рис. 4. Линеаризация кинетических данных выщелачивания рения из концентрата с использованием математических моделей «сжимающейся сферы» (***a***), Гинстлинга–Броунштейна (***b***) и Казеева–Ерофеева (***c***)

Table 4. **Kinetic characteristics of rhenium leaching from concentrates obtained using different models**

Таблица 4. Кинетические характеристики выщелачивания рения из концентрата, полученные при использовании различных моделей

Equation of "contracting sphere"		Ginstling–Brounshtein equation		Kazeev–Erofeev equation	
$1-(1-\alpha)^{1/3}=k\tau$		$1-(2/3)\alpha-(1-\alpha)^{2/3}=k\tau$		$\ln[-\ln(1-\alpha)]=n\ln\tau+\ln k_\tau$	
$k\cdot10^2$, min^{-1}	R^2	$k\cdot10^3$, min^{-1}	R^2	n	R^2
1.2	0.488	4.7	0.986	0.9	0.958

The kinetic data concerning the leaching of rhenium from the concentrate formed after the removal of nickel, with a substantial coefficient of determination, have been successfully linearized using the Ginstling—Brounshtein equation. This equation is particularly relevant for describing processes that occur in the diffusion response region. The value of the index n, which was obtained during the processing of kinetic data using the Kazeev—Erofeev equation, was found to be less than 1. This observation corroborates the results of the analysis conducted using the Ginstling—Brounshtein equation, affirming that the limiting stage of the process is indeed diffusion-driven.

Conclusion

The experimental study of the oxidative hydrochloric acid leaching of rhenium from superalloy grinding waste (particle size fraction –0.071 mm) has yielded significant findings. The highest degree of rhenium leaching (α = 91.0 %) was achieved when the process involved preliminary mixing of grinding waste in an 8M HCl solution for 1 h at approximately 100 °C. Subsequently, the reaction mixture was cooled, and hydrogen peroxide was added batchwise. This study demonstrated that increasing the concentration of hydrochloric acid from 6M to 8M, under the selected conditions, resulted in a 7.5 % increase in the degree of rhenium extraction into solution.

The analysis of kinetic data regarding the leaching of nickel, the primary component of the superalloy, from grinding waste with a 6M hydrochloric acid solution at 70 °C, using the "contracting sphere", Ginstling—Brounshtein, and Kazeev—Erofeev mathematical equations, reveals that the process operates within the kinetic reaction range.

Furthermore, the analysis of the mathematical processing of kinetic data for rhenium leaching using a solution of hydrogen peroxide in hydrochloric acid (2M) from a concentrate, which is the solid residue obtained after the leaching of nickel from grinding waste with hydrochloric acid, employing diffusion and kinetic models, indicates that the leaching rate is predominantly limited by the diffusion of hydrogen peroxide within the solid concentrate.

Subsequent processing of the leaching solutions through solvent extraction allows for the isolation of ammonium perrhenate. Rhenium metal powder, obtained from this compound through hydrogen reduction, can be employed in the production of various alloys.

References

1. Kablov E.N., Bondarenko Yu.A., Kolodyazhnyi M.Yu., Surova V.A., Narskii A.R. Prospects for the creation of high-temperature heat-resistant alloys based on refractory matrices and natural composites. *Voprosy Materialovedeniya*. 2020;4(104):64—78. (In Russ.). https://doi.org/10.22349/1994-6716-2020-104-4-64-78
Каблов Е.Н., Бондаренко Ю.А., Колодяжный М.Ю., Сурова В.А., Нарский А.Р. Перспективы создания высокотемпературных жаропрочных сплавов на основе тугоплавких матриц и естественных композитов. *Вопросы материаловедения*. 2020;4(104):64—78. https://doi.org/10.22349/1994-6716-2020-104-4-64-78
2. Palant A.A., Troshkina I.D., Chekmarev A.M., Kostylev A.I. Rhenium technology. Moscow: LLC "Galleya-Print", 2015. 329 p. (In Russ.).
Палант А.А., Трошкина И.Д., Чекмарев А.М., Костылев А.И. Технология рения. М.: ООО «Галлея-Принт», 2015. 329 с.
3. Znamenskii V.S, Korzhinskii M.A., Shteinberg G.S., Tkachenko S.I., Yakushev A.I., Laputina I.P., Bryzgalov I.A., Samotoin N.D., Magazina L.O., Kuz'mina O.V., Organova N.I., Rassulov V.A., Chaplygin I.V. Rheniite, ReS_2, the natural rhenium disulfide from fumaroles of Kudryavy volcano (Iturup isl., Kurily islands). *Zapiski Rossiiskogo Mineralogicheskogo Obshchestva*. 2005;134(5):32—39. (In Russ.).
Знаменский В.С., Коржинский М.А., Штейнберг Г.С., Ткаченко С.И., Якушев А.И., Лапутина И.П., Брызгалов И.А., Самотоин Н.Д., Магази-

на Л.О., Кузьмина О.В., Органова Н.И., Рассулов В.А., Чаплыгин И.В. Рениит, ReS_2 — природный дисульфид рения из фумарол вулкана Кудрявый (о. Итуруп, Курильские острова). *Записки Российского минералогического общества*. 2005;134(5):32—39.

4. Levchenko E.N., Klyucharev D.S. Non-traditional sources of critical rare metals. In: *Proceedings of the scientific-practical conference "Mineral and raw material base of high-tech metals. Development, reproduction, use"* (Moscow, 3—4 Dec. 2019). Moscow: FGBU "VIMS", 2020. P. 116—127. (In Russ.).
Левченко Е.Н., Ключарев Д.С. Нетрадиционные источники критических редких металлов. *Труды науч.-практ. конференции «Минерально-сырьевая база металлов высоких технологий. Освоение, воспроизводство, использование»* (Москва, 3—4 дек. 2019 г.). М.: ФГБУ «ВИМС», 2020. С. 116—127.
5. Nowotnik A. Nickel-based superalloys (Reference module in materials science and materials engineering). 2016.
https://doi.org/10.1016/B978-0-12-803581-8.02574-1
6. Yagi R., Okabe T. Current status of recycling of rhenium and process technologies. *Journal of MMIJ*. 2016;132:114—122.
https://doi.org/10.2473/journalofmmij.132.114
7. Polyak D.E. USGS metal prices in the United States through 2010: Rhenium. U.S. Geological Survey, Washington DC, 2013. P. 152—154.
8. Koizumi Y., Jianxin Z., Kobayashi T., Yokokawa T., Harada H., Aoki Y., Arai M. Development of next generation Ni-base single crystal superalloys containing ruthenium. *Journal of the Japan Institute of Metals and Materials*. 2003;67(9):468—471.
https://doi.org/10.2320/jinstmet1952.67.9
9. Srivastava R.R., Kim M.S., Lee J.C., Jha M.K., Kim B.S. Resource recycling of superalloys and hydrometallurgical challenges. *Journal of Materials Science*. 2014;49:4671—4686.
http://doi.org/10.1007/s10853-014-8219-y
10. Wang X.G., Liu J.L., Jin T., Sun X.F. The effects of ruthenium additions on tensile deformation mechanisms of single crystal superalloys at different temperatures. *Materials and Design*. 2014;63:286—293.
https://doi.org/10.1016/j.matdes.2014.06.009
11. Latief F.H., Kakehi K. Effects of Re content and crystallographic orientation on creep behavior of aluminized Ni-base single crystal superalloys. *Materials and Design*. 2013;49:485—492.
https://doi.org/10.1016/j.matdes.2013.01.022
12. Baikonurov E.G., Usol'tseva G.A., Chernyshova O.V., Drobot D.V. The effect of technological parameters on electrochemical processing of rhenium-containing heat-resistant alloy. *Non-Ferrous Metals*. 2017;10:56—60. (In Russ.). https://doi.org/10.17580/tsm.2017.08.08
Байконуров Е.Г., Усольцева Г.А., Чернышова О.В., Дробот Д.В. Влияние технологических параметров на процесс электрохимической переработки ренийсодержащего жаропрочного сплава. *Цветные металлы*. 2017;10:56—60.
https://doi.org/10.17580/tsm.2017.08.08
13. Petrova A.M., Kasikov A.G. Extraction of rhenium from waste processing and operation of heat-resistant nickel superalloys. *Aviatsionnye Materialy i Tekhnologii*. 2012;3:9—13. (In Russ.).
Петрова А.М., Касиков А.Г. Извлечение рения из отходов обработки и эксплуатации жаропрочных никелевых суперсплавов. *Авиационные материалы и технологии*. 2012;3:9—13.
14. Kasikov A.G., Petrova A.M. Rhenium recycling. Moscow: RIOR: INFRA-M, 2014. 163 p. (In Russ.).
Касиков А.Г., Петрова А.М. Рециклинг рения. М.: РИОР: ИНФРА-М, 2014. 163 с.
15. Singh Gaur R.P., Wolfe T.A., Braymiller S.A. Recycling of rhenium-containing wire scrap. *International Journal of Refractory Metals and Hard Materials*. 2015;50:79—85.
http://doi.org/10.1016/j.ijrmhm.2014.11.003
16. Anderson C.D., Taylor P.R., Anderson C.G. Extractive metallurgy of rhenium: A review. *Minerals and Metallurgical Processing*. 2013;30(1):59—73.
http://doi.org/10.1007/BF03402342
17. Agapova L.Ya., Kilibayeva S.K., Zagorodnyaya A.N. Electrochemical processing of metal wastes of rhenium-containing heat-resistant nickel alloys. *Solid State Phenomena*. 2021;316:631—636.
https://doi.org/10.4028/www.scientific.net/SSP.316.631
18. Mamo S., Elie M., Baron M., Simons A., Gonzalez-Rodriguez J. Leaching kinetics, separation, and recovery of rhenium and component metals from CMSX-4 superalloys using hydrometallurgical processes. *Separation and Purification Technology*. 2019;212:150—160.
https://doi.org/10.1016/J.SEPPUR.2018.11.023
19. Targanov I.E., Troshkina I.D. Kinetics of sulfuric acid leaching of nickel from grinding waste of rhenium-containing superalloys. *Izvestiya. Non-Ferrous Metallurgy*. 2021;27(4):24—31. (In Russ.).
https://doi.org/10.17073/0021-3438-2021-4-24-31
Тарганов И.Е., Трошкина И.Д. Кинетика серно-кислотного выщелачивания никеля из шлифотходов ренийсодержащих суперсплавов. *Известия вузов. Цветная металлургия*. 2021;27(4):24—31.
https://doi.org/10.17073/0021-3438-2021-4-24-31
20. Zante G., Boltoeva M., Masmoudi A., Barillon R., Trébouet D. Selective separation of cobalt and nickel using

a stable supported ionic liquid membrane. *Separation and Purification Technology.* 2020;252:117477. https://doi.org/10.1016/j.seppur.2020.117477.hal-03419681

21. Free M.L. Hydrometallurgy: Fundamentals and applications. New Jersey, USA: John Wiley & Sons, 2013. 444 p.
22. Ginstling A.M., Brounshtein B.I. Concerning the diffusion kinetics of reactions in spherical particles. *Zhurnal Prikladnoi Khimii.* 1950;23:1249—1259. (In Russ.).
Гинстлинг А.М., Броунштейн Б.И. О кинетике диффузии реакций в сферических частицах. *Журнал прикладной химии.* 1950;23:1249—1259.

Information about the authors

Igor E. Targanov – Postgraduate Student of the Department of Technology of Rare Elements and Nanomaterials (TREN), Mendeleev University of Chemical Technology of Russia (MUCTR).
https://orcid.org/0000-0001-8354-0018
E-mail: targanov.igor@yandex.ru

Maksim A. Solodovnikov – Student of the Department of TREN, MUCTR.
https://orcid.org/0009-0009-3497-160X
E-mail: solodovnikovmaksim1@gmail.ru

Irina D. Troshkina – Dr. Sci. (Eng.), Professor of the Department of TREN, MUCTR.
https://orcid.org/0000-0002-5523-0247
E-mail: troshkina.i.d@muctr.ru

Информация об авторах

Игорь Евгеньевич Тарганов – аспирант кафедры технологии редких элементов и наноматериалов (ТРЭН) Российского химико-технологического университета (РХТУ) им. Д.И. Менделеева.
https://orcid.org/0000-0001-8354-0018
E-mail: targanov.igor@yandex.ru

Максим Александрович Солодовников – студент кафедры ТРЭН РХТУ им. Д.И. Менделеева.
https://orcid.org/0009-0009-3497-160X
E-mail: solodovnikovmaksim1@gmail.ru

Ирина Дмитриевна Трошкина – д.т.н., профессор кафедры ТРЭН РХТУ им. Д.И. Менделеева.
https://orcid.org/0000-0002-5523-0247
E-mail: troshkina.i.d@muctr.ru

Contribution of the authors

I.E. Targanov – conducted experiments, contributed to the discussion of the results, authored the manuscript.

M.A. Solodovnikov – analyzed samples through photometric and titrimetric methods, contributed to the discussion of the results.

I.D. Troshkina – formulated the research objectives, contributed to the discussion of the results, revised the manuscript.

Вклад авторов

И.Е. Тарганов – проведение экспериментов, участие в обсуждении результатов, написание статьи.

М.А. Солодовников – проведение анализов проб методами фотометрии и титриметрии, участие в обсуждении результатов.

И.Д. Трошкина – определение цели работы, участие в обсуждении результатов, редакция статьи.

The article was submitted 27.04.2023, revised 30.07.2023, accepted for publication 02.08.2023

Статья поступила в редакцию 27.04.2023, доработана 30.07.2023, подписана в печать 02.08.2023

FOUNDRY / ЛИТЕЙНОЕ ПРОИЗВОДСТВО

UDC 669.721.5
https://doi.org/10.17073/0021-3438-2023-5-34-46

Research article
Научная статья

Microstructure and properties of the GEWZ522K casting magnesium alloy based on the Mg–Gd–Nd–Y–Zn–Zr system

A.V. Koltygin, A.V. Pavlov, V.E. Bazhenov, O.D. Gnatyuk, I.I. Baranov, V.D. Belov

National University of Science and Technology "MISIS"
4 build 1 Leninskiy Prosp., Moscow, 119049, Russia

✉ Viacheslav E. Bazhenov (V.E.Bagenov@gmail.com)

Abstract: The article discusses the solidification and phase composition of the (wt.%) Mg–4.8Gd–2.1Nd–1.6Y–0.4Zn–0.6Zr (GEWZ522K) casting alloy. It is demonstrated that in the as-cast state, the alloy structure comprises primary zirconium particles, dendrites of the magnesium solid solution (αMg), and eutectic intermetallic phases located between dendritic branches. Following solution heat treatment at t = 530±5 °C, the alloy transitions into a single-phase state and can be significantly strengthened through artificial aging after quenching. It is recommended to apply alloy aging at t = 250 °C for 8–10 h or at t = 200 °C for 15–18 h. This approach leads to the maximum strengthening of the alloy, with the best mechanical properties achieved for the alloy aged at t = 250 °C. Regardless of the aging method used, the ultimate tensile strength (UTS) of the samples surpasses 300 MPa, which significantly exceeds that of commercial casting alloys according to GOST 2856-79. The measured corrosion rate for the GEWZ522K alloy is 7.5±0.4 mm/year, that slightly higher than that for the less alloyed commercial alloy ML10 (approximately 2.5 mm/year) tested under similar conditions. Furthermore, the alloy was subjected to tests for ignition resistance when in contact with air. It was observed that with continuous airflow over the specimen's surface, ignition centers appear at t = 625 °C due to the breakdown of the oxide film, causing the alloy to nearly completely melt. Therefore, the GEWZ522K alloy can be employed as a high-strength casting alloy. However, during the operation of cast parts, particular attention must be paid to safeguarding the surface of these parts against corrosion.

Keywords: magnesium alloy, casting, Mg–Gd–Nd–Y–Zn–Zr, high strength alloy, magnesium corrosion, magnesium ignition.

For citation: Koltygin A.V., Pavlov A.V., Bazhenov V.E., Gnatyuk O.D., Baranov I.I., Belov V.D. Microstructure and properties of the GEWZ522K casting magnesium alloy based on the Mg–Gd–Nd–Y–Zn–Zr system. *Izvestiya. Non-Ferrous Metallurgy.* 2023;29(5):34–46. https://doi.org/10.17073/0021-3438-2023-5-34-46

Структура и свойства литейного магниевого сплава GEWZ522K системы Mg–Gd–Nd–Y–Zn–Zr

А.В. Колтыгин, А.В. Павлов, В.Е. Баженов, О.Д. Гнатюк, И.И. Баранов, В.Д. Белов

Национальный исследовательский технологический университет «МИСИС»
119049, Россия, г. Москва, Ленинский пр-т, 4, стр. 1

✉ Вячеслав Евгеньевич Баженов (V.E.Bagenov@gmail.com)

Аннотация: Рассмотрены кристаллизация и фазовый состав литейного сплава (мас.%) Mg–4,8Gd–2,1Nd–1,6Y–0,4Zn–0,6Zr (GEWZ522K). Показано, что в литом состоянии структура сплава состоит из первичных частиц циркония, дендритов магниевого твердого раствора αMg и эвтектических интерметаллических фаз, находящихся между их ветвями. В результате отжига при

t = 530±5 °C сплав переходит в однофазное состояние и после закалки может быть значительно упрочнен в результате искусственного старения. Было предложено проводить старение сплава при t = 250 °C длительностью 8–10 ч или при t = 200 °C в течение 15–18 ч. При этом достигается максимальное упрочнение сплава, однако лучшие механические свойства были получены для сплава, состаренного при t = 250 °C. Независимо от режима старения, предел прочности на растяжение ($\sigma_в$) образцов превосходит 300 МПа, что гораздо выше показателей промышленных литейных сплавов по ГОСТ 2856-79. Рассчитанная скорость коррозии для сплава GEWZ522K равна 7,5±0,4 мм/год, что несколько больше, чем для менее легированного промышленного сплава МЛ10 (порядка 2,5 мм/год), испытанного в аналогичных условиях. Сплав был также испытан на сопротивление к возгоранию в контакте с воздухом. Установлено, что при непрерывном поступлении воздуха к поверхности образца очаги возгорания появляются при t = 625 °C вследствие разрушения оксидной плены, когда сплав практически полностью расплавляется. Таким образом, сплав GEWZ522K может быть использован в качестве высокопрочного литейного сплава. Однако при эксплуатации литых деталей из него необходимо уделять пристальное внимание защите их поверхности от коррозионного воздействия.

Ключевые слова: магниевый сплав, литье, Mg–Gd–Nd–Y–Zn–Zr, высокопрочный, коррозия магния, возгорание магния.

Для цитирования: Колтыгин А.В., Павлов А.В., Баженов В.Е., Гнатюк О.Д., Баранов И.И., Белов В.Д. Структура и свойства литейного магниевого сплава GEWZ522K системы Mg–Gd–Nd–Y–Zn–Zr. *Известия вузов. Цветная металлургия*. 2023;29(5):34–46. https://doi.org/10.17073/0021-3438-2023-5-34-46

Introduction

Magnesium alloys are considered one of the most promising materials for aerospace and automotive parts due to their low density, high specific strength, and high machining performance [1—3]. Nevertheless, despite the significant efforts made in recent decades to improve Mg alloys [4], their use remains very limited. One of the reasons for this limitation is the relatively low operating temperature of the most common industrial magnesium alloys and the associated fire in air [5; 6]. Additionally, due to magnesium's high chemical reactivity, magnesium alloys often exhibit reduced corrosion resistance [7].

It is well-known that the addition of rare earths (REs) to Mg-based alloys can significantly enhance their mechanical properties at both room and elevated operating temperatures, primarily through strengthening via artificial aging of a supersaturated solid solution of alloying elements in magnesium [3]. Neodymium is among the most commonly used rare earth element for alloying magnesium alloys. It is present in substantial quantities in industrial magnesium alloys hardened by aging. Its solubility decreases notably from approximately 2.1 wt.% at the eutectic temperature to very low values at room temperature [7; 8]. Yttrium also exhibits relatively high solubility in magnesium (~10 wt.%) and is frequently employed as an alloying component, particularly in alloys designed for elevated-temperature applications [5; 8—10]. The heavy rare-earth element gadolinium boasts substantial solubility in solid magnesium (~24 wt.%) at temperatures near the eutectic point. However, its solubility sharply decreases to 3.8 wt.% when the temperature is reduced to 200 °C, leading to significant strengthening during aging [10; 11]. The use of these rare earth elements for strengthening magnesium-based alloys and extending their service temperature limit holds great promise.

Currently, several experimental alloys based on the Mg—Gd—Y—Zn—Zr system are known [12—14]. However, these alloys typically contain a high Gd content, exceeding 8 wt.%. This high Gd content is a consequence of the wide solubility range of gadolinium in solid magnesium. Nevertheless, by incorporating other rare earth elements (REs) such as neodymium into the alloy composition, it becomes possible to reduce the solubility of Gd and Y in magnesium, thus minimizing their presence in the alloy while achieving the desired strengthening effect. The objective of this study was to investigate a novel high-strength casting magnesium alloy. This alloy contains a significant amount of gadolinium as the primary alloying addition, alongside traditional neodymium and yttrium, which are common components in commercial casting alloys. The study focuses on the formation of the cast and heat-treated microstructure and phase composition of this new magnesium alloy [15], based on the Mg—Gd—Nd—Y—Zn—Zr system. By harnessing both light (Nd, Y) and heavy (Gd) rare earth elements, this alloy demonstrates impressive strength properties at relatively low concentrations of Gd and Y. Additionally, the study assesses the impact of these rare earth elements on the alloy's corrosion resistance and its susceptibility to ignition in air.

Materials and methods

The Mg—4.8Gd—2.1Nd—1.6Y—0.4Zn—0.6Zr (wt.%) alloy, designated as GEWZ522K, was prepared using the following materials: industrial-grade magnesium

(99.9 wt.% purity), zinc (99.975 wt.%), commercial master alloys Mg—15Zr (SOMZ LLC, Solikamsk), Mg—20Y, Mg—20Nd (Metagran PC, Moscow), and a Mg—36Gd (wt.%) master alloy produced in-house.

The Mg—Gd master alloy was fabricated in a resistance furnace using the flux free melting method. Initially, industrial-grade magnesium of 99.95 wt.% purity was placed in a clean steel crucible. After complete melting of magnesium, bulk gadolinium 99.9 wt.% purity was added to the melt. The melting process continued until the gadolinium was entirely dissolved. The resulting melt was poured into the mold at a temperature of 740 °C.

The alloy itself was prepared in a resistance furnace also using the flux free melting method. Melting took place in a PT 90/13 furnace (LAC, Czech Republic), within a steel crucible, under the protection of a mixture of argon and sulfur hexafluoride (SF_6) (2 vol.%). The process began with loading industrial-grade magnesium into a clean steel crucible, followed by the addition of zinc, Mg—Zr, Mg—Nd, Mg—Gd, and Mg—Y master alloys as the magnesium melted. After the melt reached a temperature of 780 °C, it was thoroughly mixed using a steel tool. The total mass of the molten alloy was 2 kg. Casting into molds occurred after a 15-minute hold in the furnace at a temperature of 760 °C. Subsequently, the crucible was removed from the furnace, and the alloy was cast into both steel and graphite molds once the melt temperature reached a temperature of 740 °C. The mold temperature was maintained at 25±2 °C. For microstructure analysis, corrosion tests, and ignition tests, cylindrical ingots 35 mm in diameter and 150 mm in height were cast into steel molds. To determine mechanical properties, the ingots were cast into graphite molds. After undergoing heat treatment, which included solution heat treatment followed by quenching and artificial aging (T6 mode), cylindrical proportional samples with a diameter of 5 mm (type III, number 7 according to GOST 1497-84) were cut from them. Details regarding the dimensions of the graphite mold and the sample cutting process can be found elsewhere [16].

The alloy's microstructure and phase composition were investigated using the Vega SBH3 scanning electron microscope (SEM) from Tescan (Czech Republic), equipped with the Oxford energy-dispersive *X*-ray spectroscopy attachment. Additionally, an Axio Observer. D1m optical microscope (Carl Zeiss, Germany) was employed. An etchant solution comprising 11 g of picric acid, 11 mL of acetic acid, and 100 mL of ethyl alcohol was utilized to reveal the alloy's structure. To assess the chemical composition of the obtained alloys, energy dispersive *X*-ray spectroscopy (EDS) was performed within a 1×1 mm area.

Brinell hardness was determined using the NEMESIS 9001 universal hardness tester from INNOVATEST (Netherlands). The testing parameters included a 2.5 mm ball diameter, a 62.5 kgf load (≈613 N), and a 10-second hold time under load. A minimum of 5 measurements were conducted for each specimen.

Tensile mechanical properties were studied using the 5569 universal testing machine (Instron, USA), equipped with a non-contact video extensometer of AVE type (Instron, USA). Cylindrical samples with a 5 mm diameter (type III, No. 7 as per GOST 1497-84) were machined from blanks. The ram speed was set at 5 mm/min, and mechanical properties were determined based on at least 3 samples for each series of measurements.

Electrical conductivity measurements were conducted using the contact-free eddy current conductivity meter VE-27NC/4-5 from Sigma SPE, Ekaterinburg, with measurement limits of 5—37 MS/m. A minimum of 5 measurements were taken for each specimen.

Polythermal and isothermal sections of phase diagrams, the phase composition of alloys, and alloy solidification according to the Scheil—Gulliver model were calculated using Thermo-Calc 2016a software [17], with the thermodynamic database TCMG4 (magnesium alloys database, version 4) being utilized [18].

For corrosion tests, samples in the form of approximately 12×12×12 mm cubes, with a surface area of ~9 cm^2, were cut from the ingots after heat treatment in the T6 mode. The corrosion rate was determined using the volumetric method, based on the measurement of the amount of hydrogen released during specimens corrosion. Tests were conducted in a 3 wt.% NaCl aqueous solution at room temperature for 48 h, using a minimum of 5 samples for each series. The volume of the solution used was 500 mL. Before immersion in the solution, the sample surfaces were cleaned with P320 grit sandpaper and degreased with ethyl alcohol. The amount of released hydrogen was converted to the mass loss of the sample based on the 1 mL H_2 = 1 mg Mg ratio [19], and the corrosion rate was calculated in mm/year following the standard method [20].

To determine the ignition temperature, samples with dimensions of 25×25×60 mm were prepared. Their surfaces were cleaned using P320 grit paper. During the tests, the alloy sample was placed in a sealed steel crucible, and a constant airflow of 1 L/min, controlled by a rotameter, was provided in the crucible space. The crucible containing the sample was heated in a re-

sistance furnace to the desired temperature (600, 625, and 650 °C), with a subsequent 2-hour hold at that temperature. Temperature readings were recorded using the BTM-4208SD 12-channel temperature recorder (Lutron, Israel).

Results and discussion

Figure 1 depicts the microstructure of the alloy in as cast state. The predominant features include dendrites of a magnesium-based solid solution, within which precipitates of the second phase, formed through the eutectic reaction, are situated. Additionally, within the solid solution, distinct near spherical precipitates were identified in the microstructure using optical microscopy after etching. These precipitates exhibit significant contrast compared to the surrounding background when observed through SEM. To elucidate the phase composition of the alloy, its solidification behavior was analyzed by referencing the sections of the multicomponent phase diagram within the alloy's existence region. These calculations were performed using Thermo-Calc software. Zinc was not considered in the calculation due to its minimal presence in the alloy, which has an insignificant impact on the solidification process.

Figure 2 displays polythermal sections of the phase diagram within the composition region of the GEWZ522K alloy. It is evident that the equilibrium solidification process of the alloy starts with the precipitation of primary zirconium-based crystals from the liquid at t ~ 820 °C. Thermo-Calc software calculations have indicated that these crystals are nearly pure zirconium. Subsequently, as the alloy temperature decreases to t ~ 640 °C, the peritectic reaction commences, leading to the complete transformation of zirconium into a magnesium-based solid solution (αMg). Upon further cooling to t ~ 520 °C, zirconium precipitated once more from the supersaturated αMg, forming its distinct phase. Consequently, the equilibrium effective freezing range of the alloy, excluding the primary zirconium solidification region, spans approximately 120 °C. Additionally, as the temperature decreases further, a compositionally variable phase, $Mg_{41}RE_5$ precipitates from αMg, primarily consisting of a mixture of Nd and Y, with a minimal Gd content. Around t ~ 300 °C, the formation of the gadolinium-rich phase $GdMg_5$ becomes evident. Notably, an increase in the Y content exceeding 2 wt.% and a decrease in the Nd content below 1.5 wt.% alter the solidification path of the alloy, leading it into the realm of forming the binary compound $Mg_{24}Y_5$. Consequently, it can be inferred that the GEWZ522K alloy may not endure prolonged holding at t = 300 °C or higher. At such temperatures, the hardening gadolinium-based particles dissolve into the αMg solid solution. Therefore, the practical upper operating temperature limit for this alloy is expected to be lower.

Figure 3 displays the isothermal sections of the multicomponent phase diagram for the Mg—2Nd—0.5Zn—

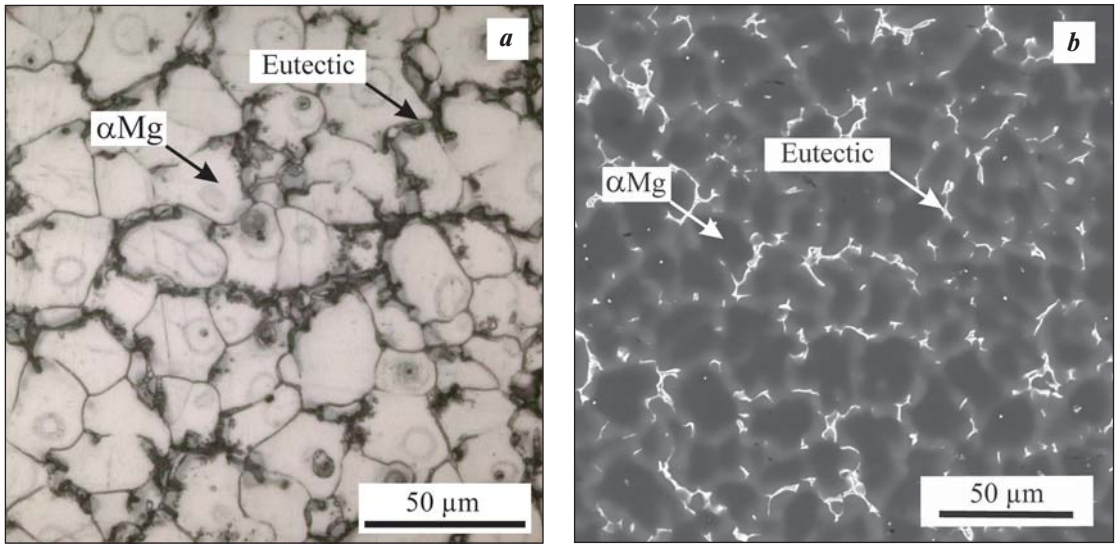

Fig. 1. Microstructure of the GEWZ522K alloy in the as-cast state
a – OM, etched; ***b*** – SEM

Рис. 1. Микроструктура сплава GEWZ522K в литом состоянии
a – ОМ, травлено; ***b*** – СЭМ

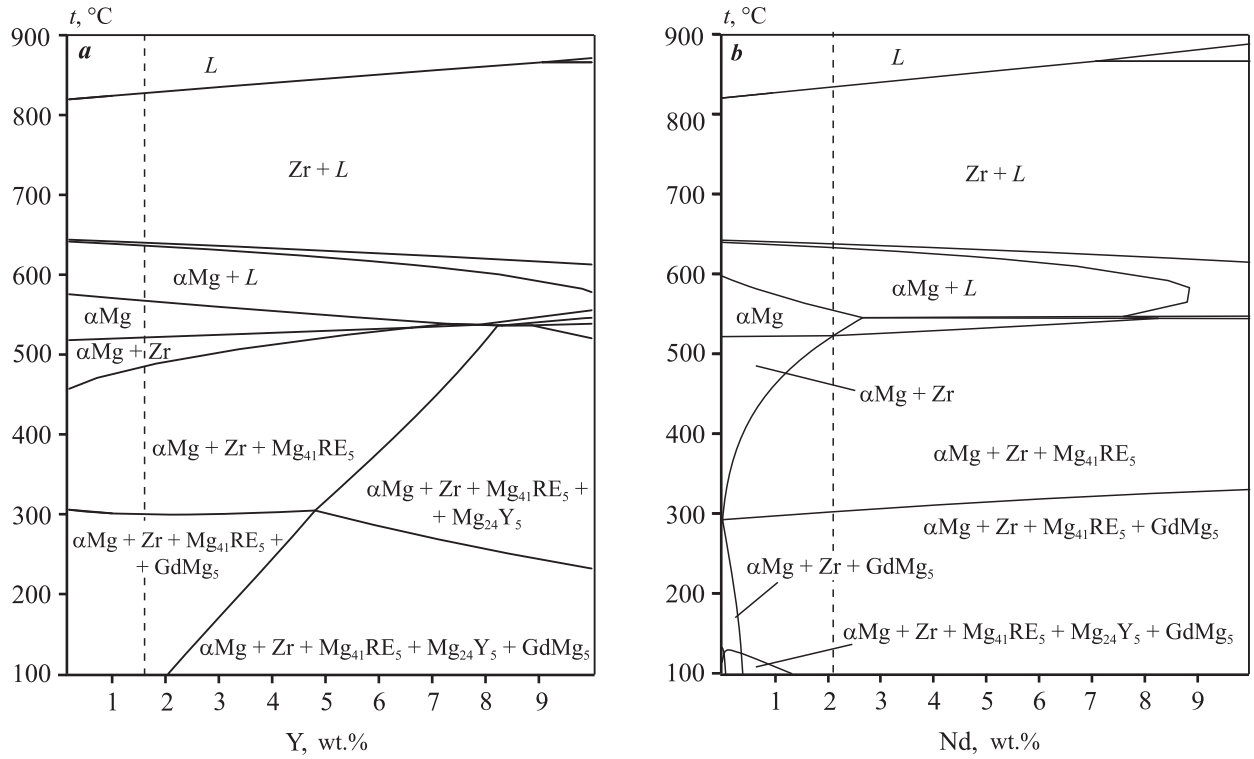

Fig. 2. Polythermal sections of the (wt.%) Mg–5Gd–2Nd–0.6Zr–Y (***a***) and Mg–5Gd–2Y–0.6Zr–Nd (***b***) phase diagrams
The dashed line shows the alloying components content in the GEWZ522K alloy

Рис. 2. Политермические сечения диаграммы состояния для сплавов (мас.%) Mg–5Gd–2Nd–0,6Zr–Y (***a***) и Mg–5Gd–2Y–0,6Zr–Nd (***b***)
Пунктирной линией показано содержание легирующего компонента сплава GEWZ522K

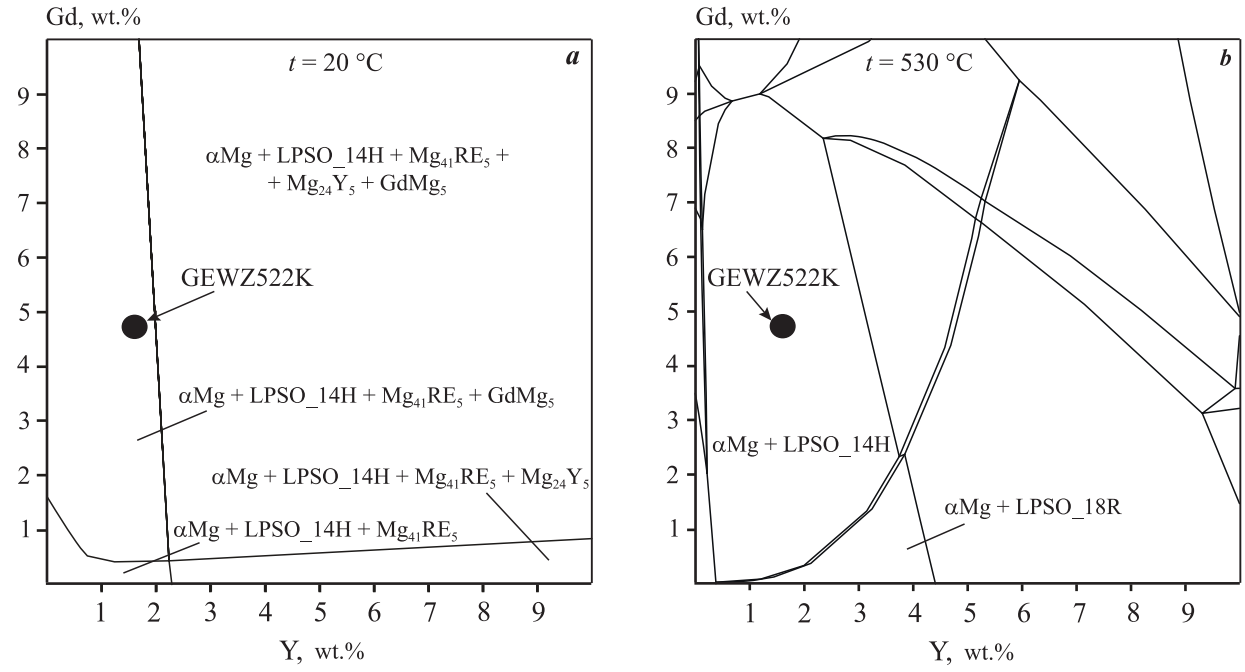

Fig. 3. Isothermal sections of the (wt.%) Mg–2Nd–0.5Zn–Y–Gd phase diagram at 20 °C (***a***) and 530 °C (***b***)

Рис. 3. Изотермические сечения диаграммы состояния сплава (мас.%) Mg–2Nd–0,5Zn–Y–Gd при температурах 20 °C (***a***) и 530 °C (***b***)

Y—Gd (wt.%) alloy at room temperature (20 °C) and at 530 °C, which is approximately 20 °C lower than the solidus temperature of the alloy (as shown in Fig. 2). In this calculation, zinc (0.5 %) was taken into account, and for the sake of clarity, zirconium was omitted. Notably, at t = 530 °C, the alloy exhibits a nearly single-phase equilibrium structure, with only a minimal presence of the LPSO phase. Despite our investigation of the as cast alloy's microstructure, the lamellar structure typically associated with LPSO was not observed. It is highly likely that this structure is either entirely absent or present in extremely low quantities.

Before proceeding with heat treatment, it is essential to confirm that the alloy does not form low melting point structural components or phases during non-equilibrium solidification. To assess this, solidification was calculated for the (wt.%) Mg—5.5Gd—2.0Nd—2.0Y—0.4Zn—0.6Zr alloy. This calculation employed slightly higher amounts of alloying elements to ensure the detection of potential non-equilibrium solidus temperature. As depicted in Fig. 4, the calculation employing the Scheil—Gulliver model reveals a non-equilibrium solidus at t = 520 °C. Nevertheless, the quantity of non-equilibrium phases formed at this temperature is negligible. To prevent the melting of the non-equilibrium eutectic, it is advisable to gradually reach the heat treatment temperature of 530 °C, allowing sufficient time for the dissolution of the non-equilibrium eutectic within αMg.

At room temperature, the alloy exhibits equilibrium between the $Mg_{41}RE_5$ and $GdMg_5$ phases with the αMg solid solution, possibly accompanied by a negligible presence of LPSO. Consequently, the alloy possesses the potential for heat treatment induced strengthening. This can be achieved by solution heat treatment at a temperature slightly below the solidus temperature, such as at t = 530 °C, followed by rapid quenching and subsequent aging. During aging, hardening particles enriched with REs are released, taking advantage of the known propensity of Gd alloys for artificial aging [10; 13]. Utilizing the polythermal section of the phase diagram obtained (refer to Fig. 2), it becomes possible to determine the appropriate aging temperature for the alloy within the temperature ranging from 200 to 250 °C. This temperature range corresponds to the region where hardening particles containing REs will precipitate from the αMg supersaturated solution. Furthermore, the selection of the aging temperature took into consideration the anticipated maximum operating temperature of the cast component.

The alloy sample underwent a high-temperature solid solution heat treatment at t = 530 °C for 8 h, followed by quenching in hot water and subsequent aging at temperatures of t = 200 and 250 °C. The duration of the high-temperature solid solution heat treatment was determined based on the microstructure of the samples. Sufficient time was allowed for the dissolution of all eutectic intermetallic phases situated at the boundaries of αMg dendrites. Figure 5 illustrates the resulting structure of the alloy after heat treatment, including solution heat treatment at t = 530 °C for 8 hours with water quenching, followed by aging at t = 250 °C for 9 h. Notably, all intermetallic phases present in the as cast structure along the αMg dendrite boundaries have completely dissolved. Compact inclusions of the zirconium phase can be observed within the αMg grains. Consequently, the alloy structure after heat treatment can be deemed single-phase. However, upon closer examination, micro-particles of the hardening phase can be observed, which formed as a result of the decomposition of the αMg supersaturated solid solution during aging (Fig. 5, *b*). The largest and most distinct particles are prominently distributed around the zirconium inclusions.

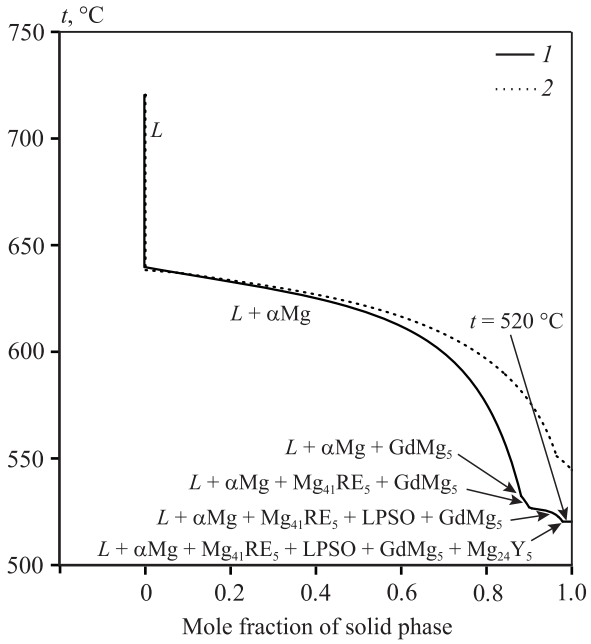

Fig. 4. Results of calculation of the solid phase fraction dependence on temperature for the Mg–5.5Gd–2.0Nd–2.0Y–0.4Zn–0.6Zr alloy at non-equilibrium solidification as per the Schell–Gulliver model (***1***) and for equilibrium solidification conditions (***2***)

Рис. 4. Результаты расчета зависимости количества твердой фазы от температуры для сплава (мас.%) Mg–5,5Gd–2,0Nd–2,0Y–0,4Zn–0,6Zr при неравновесной кристаллизации по модели Шейла–Гулливера (***1***) и для равновесных условий кристаллизации (***2***)

The selection of the aging regime for the GEWZ522K alloy was based on the aim of achieving high mechanical properties after aging. During the aging process of alloys containing Gd and Y, hardening precipitates are sequentially formed as the αMg supersaturated solid solution decomposes. This progression includes stages such as αMg supersaturated solid solution → metastable β″ (D019) → metastable β′ (cbco — base-centered orthorhombic lattice) → metastable β_1 (fcc — face centered cubic lattice) → stable β (fcc) [21; 22]. Importantly, the most significant hardening is accomplished by particles whose crystal lattice exhibits coherence or partial coherence with the lattice of the αMg magnesium solid solution. Therefore, the maximum hardening occurs when the highest number of such particles is released. Since these particles are metastable, they gradually transition to a stable form and the hardening effect diminishes over time, a phenomenon known as the overaging effect. To determine the necessary aging duration for the alloy, samples after quenching were subjected to regular hardness measurements while being kept at the aging temperature. Hardness is directly related to the strength of the magnesium alloy: higher hardness corresponds to greater alloy strength. Consequently, the point at which maximum hardness is attained signifies optimal alloy hardening, and the time required to reach this hardness level represents the ideal aging duration at the given temperature.

Figure 6 illustrates the relationship between the hardness of the solution heat treated alloy and aging time at temperatures of t = 200 and 250 °C, with measurements conducted at 3-hour intervals. The results indicate that at t = 250 °C, maximum hardness is achieved after approximately 8 to 10 h of aging, with a decrease in hardness observed after τ = = 12 h. In the case of aging at t = 200 °C, maximum hardness is reached during a holding period of τ = = 15÷18 h. These values for aging duration can be considered optimal for this alloy. The gradual precipitation in the supersaturated solid solution throughout the alloy aging process leads to a reduction in the concentration of alloying component atoms in magnesium. Consequently, this results in an increase in the electrical conductivity of the alloys during aging. Therefore, the change in electrical conductivity effectively correlates with the alteration in sample hardness during heat treatment and can serve as an additional indicator of the progress of the alloy aging process.

Tensile tests were conducted on the alloy after heat treatment, as depicted in Fig. 7. The results clearly demonstrate the alloy's impressive mechanical properties when compared to casting alloys commonly utilized in the native industry (according to GOST 2856-79). Regardless of the heat treatment process, the ultimate tensile strength (UTS) of the alloy consistently exceeded 300 MPa. Specifically, for the alloy aged at t = 250 °C,

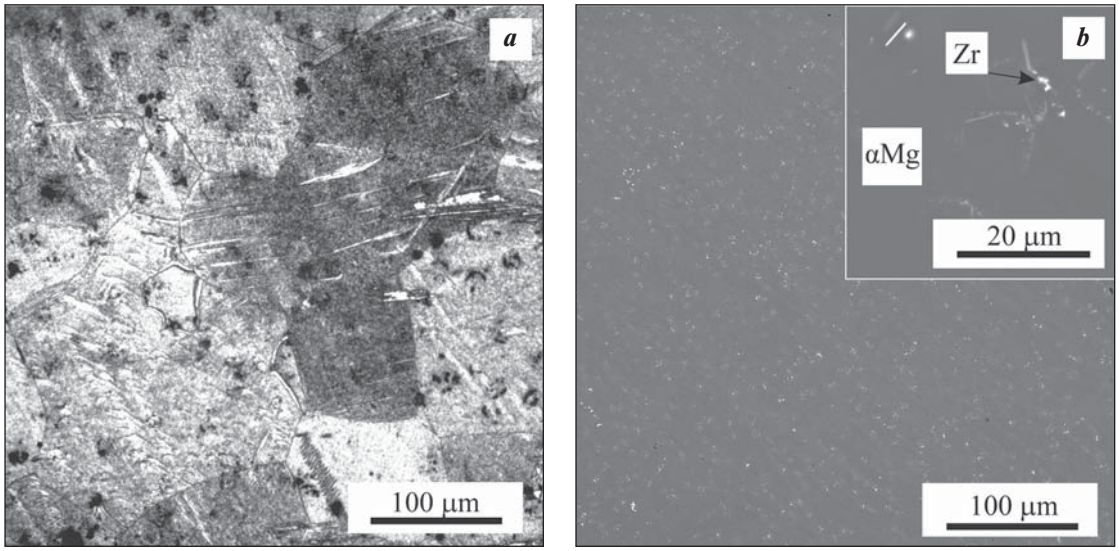

Fig. 5. Microstructure of the alloy after heat treatment (after solid solution treatment at t = 530 °C for 8 h with quenching, followed by aging at t = 250 °C for 9 h)

a – OM, etched; ***b*** – SEM

Рис. 5. Микроструктура сплава после термической обработки (закалка после отжига на твердый раствор при t = 530 °C в течение 8 ч с последующим старением при t = 250 °C в течение 9 ч)

a – ОМ, травлено; ***b*** – СЭМ

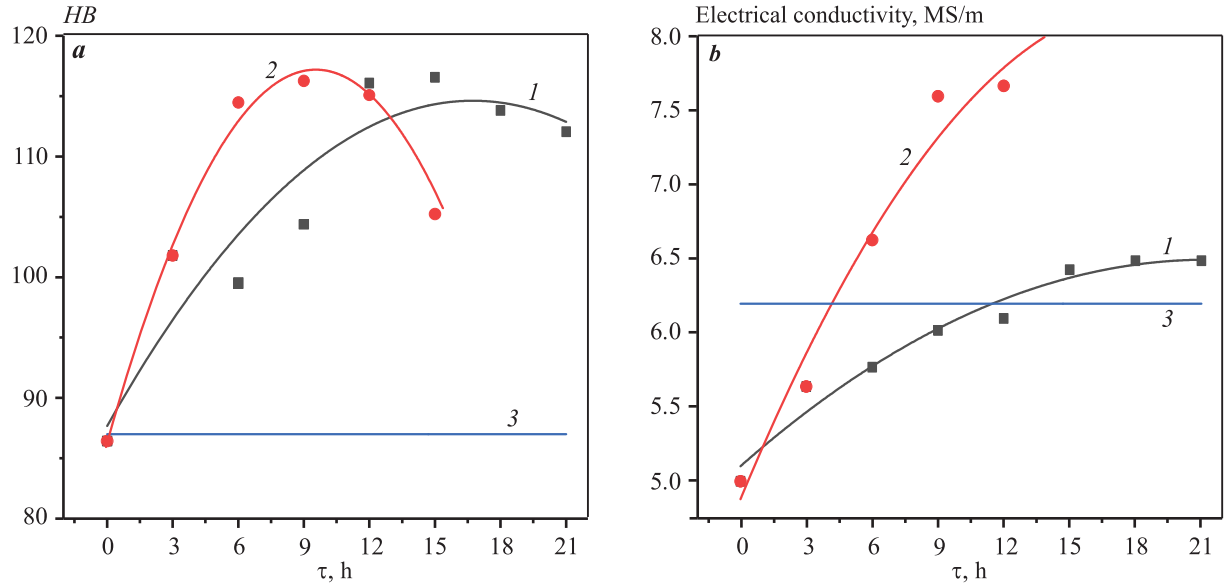

Fig. 6. Changes in hardness (***a***) and electrical conductivity (***b***) of the alloy during aging at $t = 200$ °C (***1***) and 250 °C (***2***)
The values for the as-cast state are given for comparison (***3***)

Рис. 6. Изменение твердости (***a***) и электропроводности (***b***) сплава в процессе старения при $t = 200$ °C (***1***) и 250 °C (***2***)
Для сравнения даны значения для литого состояния (***3***)

UTS = 325±11 MPa, at $t = 200$ °C, UTS = 324±4 MPa. These results are notable for magnesium alloys, surpassing the performance standards set by GOST 2856-79. The yield strength of the alloy after heat treatment also remained high, with values of 227±6.5 MPa and 185±21 MPa observed for alloys subjected to aging at $t = 250$ and 200 °C, respectively. In terms of elongation at fraction (El), the studied samples that underwent aging at $t = 250$ and 200 °C exhibited values of 4.7±1.6 % and 3.3±0.4%, respectively. Consequently, the alloy aged at $t = 250$ °C achieved the most favorable mechanical properties. It is worth noting that aging at $t =$ = 200 °C did not yield similarly high mechanical properties within a reasonable time frame. The relatively wide confidence limits observed for the El values of the studied alloys are attributed to the presence of oxide films, primarily comprised of Y and Gd. These films serve to protect the alloy from atmospheric contact and may also be introduced into the melt, ultimately remaining in the casting. This factor should be considered when developing production technologies, particularly when employing fluxfree melting methods that omit fluxes for melt treatment.

The study evaluating the corrosion behavior of the alloy in a NaCl solution was conducted to assess the corrosion resistance of this new material. Five samples were tested under identical conditions. As shown in Fig. 8, *a*, the samples exhibited very similar behavior during the tests. The calculated corrosion rate for the

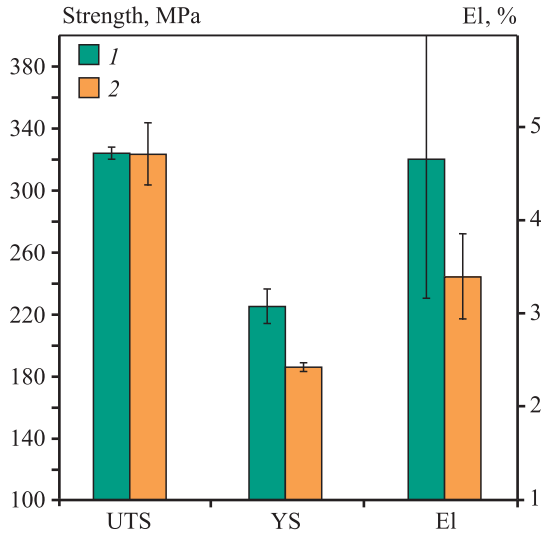

Fig. 7. Mechanical properties of the alloy after heat treatment
1 – solid solution treatment at 530 °C for 8 h + quenching + aging at 250 °C for 9 h; ***2*** – solid solution treatment at 530 °C for 8 h + + quenching + aging at 200 °C for 16 h

Рис. 7. Механические свойства сплава после термической обработки
1 – отжиг на твердый раствор (530 °C, 8 ч) + закалка + + старение (250 °C, 9 ч); ***2*** – отжиг на твердый раствор (530 °C, 8 ч) + + закалка + старение (200 °C, 16 ч)

GEWZ522K alloy was determined to be 7.5±0.4 mm/year, which is higher than that of the commercial alloy ML10 (approximately 2.5 mm/year) under similar test conditions [23]. This difference in corrosion rates may

be attributed to the abundance of hardening particles released within the magnesium solid solution during the aging process, which act as cathodes in relation to it. Consequently, numerous microgalvanic pairs are formed, intensifying galvanic corrosion [23; 24]. In Fig. 8, *b*, the cross-section of a sample after corrosion tests is presented. It can be observed that the most significant areas of corrosion damage in the alloy are located in regions where intermetallic phases and zirconium precipitates (indicated by white dots) accumulate. This suggests that their presence in the alloy structure exacerbates corrosion. Notably, the ML10 commercial alloy contains up to 2.8 wt.% of Nd, whereas the studied GEWZ522K alloy contains a sum of 8.5 wt.% REs. This threefold increase in the total RE content in the studied alloy led to a corresponding threefold increase in the corrosion rate compared to the ML10 alloy. This observation confirms the notion of an almost linear correlation between the galvanic corrosion rate of heat-treated alloys with REs and Zr and the total content of REs and Zr [23]. Consequently, an increase in the corrosion rate in RE-rich alloys is an unavoidable trade-off for enhancing the alloy's mechanical properties. The introduction of elements that form a more robust layer of corrosion products on the alloy's surface in corrosive environments could potentially reduce the corrosion rate, but further research is necessary to explore this avenue.

The propensity of the cast magnesium alloy to ignite in the presence of air is of paramount importance. The addition of yttrium and gadolinium was expected to raise the ignition temperature of the alloy under examination. Flammability tests were conducted on the alloy samples. The methodology employed in this study allowed for some degree of simulation of actual conditions in which magnesium parts might ignite, as the alloy samples were consistently exposed to air blowing over their surface. The results indicated that the alloy resisted ignition until it reached complete melting, at which point the surface oxide film broke. As shown in Fig. 9, under the conditions of sample heating to a temperature of 625 °C, isolated ignition centers appeared, accompanied by significant deviations in the temperature curve, indicating substantial heat release. This behavior stemmed from variations in the geometry of the samples and the disruption of the protective oxide film on their surface. The presence of yttrium and gadolinium in the alloy led to the formation of a relatively dense surface oxide film that protected the alloy from oxidation [25; 26]. When the samples melted and underwent changes in geometry, the existing oxide film on the alloy's surface lost continuity and failed to regenerate under the experimental conditions, resulting in the emergence of ignition centers. Therefore, it can be concluded that the alloy demonstrates notable resistance to ignition, at least until complete melting occurs.

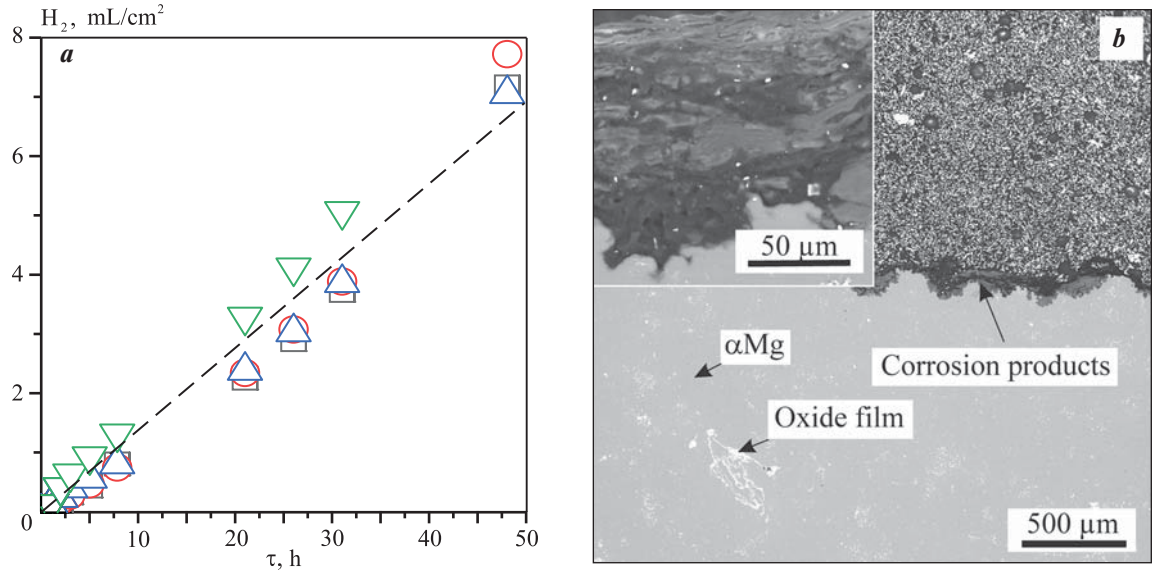

Fig. 8. Dependence of hydrogen evolution on the corrosion test time of alloy samples in 3 wt.% NaCl aqueous solution at room temperature for 48 h (the dashed line shows the averaged dependence) (***a***) and cross-section of the sample after corrosion tests (***b***)

Рис. 8. Зависимость выделения водорода от времени коррозионных испытаний образцов сплава в водном растворе 3 мас.% NaCl при комнатной температуре в течение 48 ч (штриховая линия – усредненная зависимость) (***a***) и поперечное сечение образца после коррозионных испытаний (***b***)

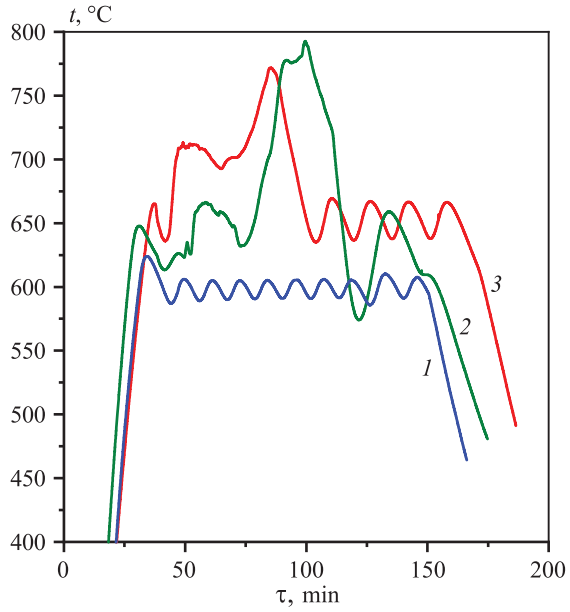

Fig. 9. Ignition test for the GEWZ522K alloy in air at t = 600 °C (***1***), 625 °C (***2***), 650 °C (***3***)

Рис. 9. Испытание на возгорание для сплава GEWZ522K на воздухе при t = 600 °C (***1***), 625 °C (***2***), 650 °C (***3***)

Conclusions

1. The structure of the GEWZ522K casting alloy comprises αMg-based solid solution dendrites and eutectic intermetallic phases situated between these dendritic branches. Furthermore, the alloy's structure features small zirconium precipitates formed as soon as the alloy's temperature drops below the liquidus. Simultaneously, the alloy exhibits an equilibrium freezing range of approximately 120 °C, which is shorter than that of most commercial casting magnesium alloys as per GOST 2856-79. The alloy's structure includes two types of intermetallics containing rare earth elements (REs): $Mg_{41}RE_5$, primarily composed of a mixture of Nd and Y, and $GdMg_5$, which predominantly contains gadolinium.

2. The optimal solution heat treatment temperature for the alloy to reach single phase structure has been determined as 530±5 °C. At this temperature, nearly all phases except Zr completely dissolve in αMg. The duration of solution heat treatment depends on the thickness of the casting and typically lasts around 8—10 h. Subsequent to quenching, the alloy can undergo aging, during which metastable and stable hardening particles containing REs are formed. However, calculations for a completely non-equilibrium solidification, following the Scheil—Gulliver model, suggest a non-equilibrium solidus temperature of 520 °C. This should be taken into consideration when designing the heat treatment regime to prevent melting of the non-equilibrium eutectic.

3. The alloy experiences significant strengthening through heat treatment in the T6 mode. The best strengthening results are achieved at an aging temperature of 250 °C. Under these conditions, the alloy exhibits a high yield strength of YS = 227±6.5 MPa, with a elongation at fracture of El = 4.7±1.6 %. The tensile strength of the alloy remains around UTS ~ 325 MPa, regardless of the aging temperature. The alloy's hardness after aging is approximately 110 HB.

4. Post-heat treatment, the alloy's structure is primarily single-phase, representing a solid solution with microscopic strengthening particles formed through aging. Clusters of such particles, which are larger in size, are notably observed around the primary Zr crystals. The LPSO phase, predicted by calculations, has not been detected in significant quantities within the alloy structure.

5. The corrosion rate of the alloy post-heat treatment exceeds that of the commercial ML10 alloy, produced and tested under similar conditions. This difference is attributed to the threefold increase in the total RE content in the studied alloy compared to ML10, resulting in a larger number of cathode particles formed during alloy aging and exhibiting a greater total surface area. These particles form microgalvanic pairs with the magnesium-based solid solution, leading to galvanic corrosion in the electrolyte medium.

6. Under continuous air exposure to the specimen's surface, ignition centers emerge at temperatures of t = = 625 °C. In this scenario, yttrium and gadolinium within the alloy are consumed in the formation of a dense oxide film on the metal surface.

References

1. Weiler J.P. A review of magnesium die-castings for closure applications. *Journal of Magnesium and Alloys*. 2019;7(2):297—304. https://doi.org/10.1016/j.jma.2019.02.005
2. Kulekci M.K. Magnesium and its alloys applications in automotive industry. *The International Journal of Advanced Manufacturing Technology*. 2008;39:851—865. https://doi.org/10.1007/s00170-007-1279-2
3. Zhang J., Liu S., Wu R., Hou L., Zhang M. Recent developments in high-strength Mg–RE-based alloys: Focusing on Mg—Gd and Mg—Y systems. *Journal of Magnesium and Alloys*. 2018;6(3):277—291. https://doi.org/10.1016/j.jma.2018.08.001

4. Yang Y., Xiong X., Chen J., Peng X., Chen D., Pan F. Research advances in magnesium and magnesium alloys worldwide in 2020. *Journal of Magnesium and Alloys.* 2021;9(3):705—747. https://doi.org/10.1016/j.jma.2021.04.001
5. Fan J.F., Yang Ch.L., Han G., Fang S., Yang W.D., Xu B.S. Oxidation behavior of ignition-proof magnesium alloys with rare earth addition. *Journal of Alloys and Compounds.* 2011;509(5):2137—2142. https://doi.org/10.1016/j.jallcom.2010.10.168
6. Aydin D.S., Bayindir Z., Hoseini M., Pekguleryuz M.O. The high temperature oxidation and ignition behavior of Mg—Nd alloys. Part I: The oxidation of dilute alloys. *Journal of Alloys and Compounds.* 2013;569: 35—44. https://doi.org/10.1016/j.jallcom.2013.03.130
7. Morozova G.I. Phase composition and corrosion resistance of magnesium alloys. *Metal Science and Heat Treatment.* 2008;50:100—104. https://doi.org/10.1007/s11041-008-9020-9
Морозова Г.И. Фазовый состав и коррозионная стойкость магниевых сплавов. *Металловедение и термическая обработка металлов.* 2008;3(633):8—12.
8. Rokhlin L.L., Dobatkina T.V., Tarytina I.E., Timofeev V.N., Balakhchi E.E. Peculiarities of the phase relations in Mg-rich alloys of the Mg—Nd—Y system. *Journal of Alloys and Compounds.* 2004;367(1-2):17—19. https://doi.org/10.1016/j.jallcom.2003.08.004
9. Rokhlin L.L. Magnesium alloys containing rare earth metals: Structure and properties. 1st ed. London: CRC Press, 2003. 256 p. https://doi.org/10.1201/9781482265163
10. Gao L., Chen R.S., Han E.H. Effects of rare-earth elements Gd and Y on the solid solution strengthening of Mg alloys. *Journal of Alloys and Compounds.* 2009;481(1-2): 379—384. https://doi.org/10.1016/j.jallcom.2009.02.131
11. Stulikova I., Smola B., Cizek J., Kekule T., Melikhova O., Kudrnova H. Natural and artificial aging in Mg—Gd binary alloys. *Journal of Alloys and Compounds.* 2018;738:173—181. https://doi.org/10.1016/j.jallcom.2017.12.026
12. Wei X., Jin L., Dong S., Wang F., Dong J. Effect of Zn/(Gd + Y) ratio on the microstructure evolution and mechanical properties of Mg—Gd—Y—Zn—Zr alloy. *Materials Characterization.* 2020;169:110670. https://doi.org/10.1016/j.matchar.2020.110670
13. Zheng J., Yan Z., Ji J., Shi Y., Zhang H., Zhang Z., Xue Y. Effect of heat treatment on mechanical properties and microstructure evolution of Mg—9.5Gd—4Y—2.2Zn—0.5Zr alloy. *Journal of Magnesium and Alloys.* 2022;10(4): 1124—1132. https://doi.org/10.1016/j.jma.2021.05.018
14. Liu W., Zhou B., Wu G., Zhang L., Peng X., Cao L. High temperature mechanical behavior of low-pressure sand-cast Mg—Gd—Y—Zr magnesium alloy. *Journal of Magnesium and Alloys.* 2019;7(4):597—604. https://doi.org/10.1016/j.jma.2019.07.006
15. Koltygin A.V., Pavlov A.V., Bazhenov V.E., Belov V.D. High strength magnesium alloy: Patent 2786785 (RF). 2022. (In Russ.).
Колтыгин А.В., Павлов А.В., Баженов В.Е., Белов В.Д. Высокопрочный литейный магниевый сплав: Патент 2786785 (РФ). 2022.
16. Bazhenov V.E., Koltygin A.V., Sung M.C., Park S.H., Tselovalnik Yu.V., Stepashkin A.A., Rizhsky A.A., Belov M.V., Belov V.D., Malyutin K.V. Development of Mg—Zn—Y—Zr casting magnesium alloy with high thermal conductivity. *Journal of Magnesium and Alloys.* 2021;9(5):1567—1577. https://doi.org/10.1016/j.jma.2020.11.020
17. Andersson J.O., Helander T., Höglund L., Shi P.F., Sundman B. Thermo-Calc and DICTRA, Computational tools for materials science. *CALPHAD.* 2002;26(2): 273—312. https://doi.org/10.1016/S0364-5916(02)00037-8
18. Thermo-Calc software TCMG4: TCS Mg-based alloys database. Version 4. https://thermocalc.com/products/databases/magnesium-based-alloys/ (accessed: 01.05.2022).
19. Kirkland N.T., Birbilis N., Staiger M.P. Assessing the corrosion of biodegradable magnesium implants: a critical review of current methodologies and their limitations. *Acta Biomaterialia.* 2012;8(3):925—936. https://doi.org/10.1016/j.actbio.2011.11.014
20. ASTM Standard G1-03. Standard practice for preparing, cleaning, and evaluating corrosion test specimens. West Conshohocken: ASTM International, 2011.
21. Zhou B., Liu W., Wu G., Zhang L., Zhang X., Ji H., Ding W. Microstructure and mechanical properties of sand-cast Mg—6Gd—3Y—0.5Zr alloy subject to thermal cycling treatment. *Journal of Materials Science & Technology.* 2020;43:208—219. https://doi.org/10.1016/j.jmst.2020.01.013
22. He S.M., Zeng X.Q., Peng L.M., Gao X., Nie J.F., Ding W.J. Precipitation in a Mg—10Gd—3Y—0.4Zr (wt.%)

alloy during isothermal ageing at 250 °C. *Journal of Alloys and Compounds*. 2006;421(1-2):309—313. https://doi.org/10.1016/j.jallcom.2005.11.046

23. Bazhenov V.E., Sannikov A.V., Saidov S.S., Rizhskii A.A., Koltygin A.V., Belov V.D., Yudin V.A. Effect of alloying elements content and cooling rate on corrosion resistance of ML10. *Liteinoe Proizvodstvo*. 2020;(12):13—18. (In Russ.).
Баженов В.Е., Санников А.В., Саидов С.С., Рижский А.А., Колтыгин А.В., Белов В.Д., Юдин В.А. Влияние содержания легирующих элементов и скорости охлаждения на коррозионную стойкость сплава МЛ10. *Литейное производство*. 2020;(12):13—18.
24. Kubásek J., Vojtěch D. Structural and corrosion characterization of biodegradable Mg—RE (RE = Gd, Y, Nd) alloys. *Transactions of Nonferrous Metals Society of China*. 2013;23(5):1215—1225. https://doi.org/10.1016/S1003-6326(13)62586-8
25. Bazhenov V.E., Baranov I.I., Lyskovich V.V., Koltygin A.V., Sannikov A.V., Kyaramyan K.A., Belov V.D., Pavlinich S.P. Investigation of castability, mechanical, corrosion properties and flammability of ML-OPB and EWZ43 magnesium alloys. *Izvestiya. Non-Ferrous Metallurgy*. 2023;29(1):39—55. (In Russ.). https://doi.org/10.17073/0021-3438-2023-1-39-55
Баженов В.Е., Баранов И.И., Лысковић А.А., Колтыгин А.В., Санников А.В., Кярамян К.А., Белов В.Д., Павлинич С.П. Исследование литейных, механических, коррозионных свойств и пожароопасности магниевых сплавов МЛ-ОПБ и EWZ43. *Известия вузов. Цветная металлургия*. 2023;29(1):39—55. https://doi.org/10.17073/0021-3438-2023-1-39-55
26. Tekumalla S., Gupta M. An insight into ignition factors and mechanisms of magnesium based materials: A review. *Materials & Design*. 2017;113:84—98. https://doi.org/10.1016/j.matdes.2016.09.103

Information about the authors

Andrey V. Koltygin – Cand. Sci. (Eng.), Assistant Prof., Department of Foundry Technologies and Material Art Working (FT&MAW), National University of Science and Technology "MISIS" (NUST MISIS).
https://orcid.org/0000-0002-8376-0480
E-mail: misistlp@mail.com

Aleksandr V. Pavlov – Postgraduate Student, Department of FT&MAW, NUST MISIS.
https://orcid.org/0009-0001-1934-0107
E.mail: pavloveone@mail.ru

Viacheslav E. Bazhenov – Cand. Sci. (Eng.), Assistant Prof., Department of FT&MAW, NUST MISIS.
https://orcid.org/0000-0003-3214-1935
E-mail: V.E.Bagenov@gmail.com

Olesya D. Gnatyuk – Student, Department of FT&MAW, NUST MISIS.
https://orcid.org/0009-0005-5881-5135
E-mail: olessya1234@mail.ru

Ivan I. Baranov – Student, Department of FT&MAW, NUST MISIS.
https://orcid.org/0000-0002-0465-7865
E-mail: baranov.wania@yandex.ru

Vladimir D. Belov – Dr. Sci. (Eng.), Head of the Department of FT&MAW, NUST MISIS.
https://orcid.org/0000-0003-3607-8144
E-mail: vdbelov@mail.ru

Информация об авторах

Андрей Вадимович Колтыгин – к.т.н., доцент кафедры литейных технологий и художественной обработки материалов (ЛТиХОМ) Национального исследовательского технологического университета «МИСИС» (НИТУ МИСИС).
https://orcid.org/0000-0002-8376-0480
E-mail: misistlp@mail.ru

Александр Валерьевич Павлов – аспирант кафедры ЛТиХОМ, НИТУ МИСИС.
https://orcid.org/0009-0001-1934-0107
E-mail: pavloveone@mail.ru

Вячеслав Евгеньевич Баженов – к.т.н., доцент кафедры ЛТиХОМ, НИТУ МИСИС.
https://orcid.org/0000-0003-3214-1935
E-mail: V.E.Bagenov@gmail.com

Олеся Дмитриевна Гнатюк – студент кафедры ЛТиХОМ, НИТУ МИСИС.
https://orcid.org/0009-0005-5881-5135
E-mail: olessya1234@mail.ru

Иван Ильич Баранов – студент кафедры ЛТиХОМ, НИТУ МИСИС.
https://orcid.org/0000-0002-0465-7865
E-mail: baranov.wania@yandex.ru

Владимир Дмитриевич Белов – д.т.н., заведующий кафедрой ЛТиХОМ, НИТУ МИСИС.
https://orcid.org/0000-0003-3607-8144
E-mail: vdbelov@mail.ru

Contribution of the authors

A.V. Koltygin – conceptualization, experimental data analysis, manuscript writing.

A.V. Pavlov – conducted experiments, analyzed experimental data.

V.E. Bazhenov – analyzed experimental data, edited the manuscript.

O.D. Gnatyuk – prepared samples, performed experiments.

I.I. Baranov – conducted experiments, analyzed experimental data.

V.D. Belov – supervision, manuscript editing.

Вклад авторов

А.В. Колтыгин – формирование основной концепции, обработка результатов исследований, написание текста статьи.

А.В. Павлов – проведение экспериментов, обработка результатов исследований.

В.Е. Баженов – обработка результатов исследований, редактирование текста статьи.

О.Д. Гнатюк– подготовка образцов, проведение экспериментов.

И.И. Баранов – проведение экспериментов, обработка результатов исследований.

В.Д. Белов – общее руководство, редактирование текста статьи.

The article was submitted 03.04.2023, revised 19.06.2023, accepted for publication 23.06.2023

Статья поступила в редакцию 03.04.2023, доработана 19.06.2023, подписана в печать 23.06.2023

FOUNDRY / ЛИТЕЙНОЕ ПРОИЗВОДСТВО

UDC 669.715 : 669.046.516.4 : 669.046.52
https://doi.org/10.17073/0021-3438-2023-5-47-56

Research article
Научная статья

Influence of various titanium-containing additives on the modification efficiency of aluminum–silicon eutectic alloy

A.D. Shlyaptseva, I.A. Petrov, A.P. Ryakhovskiy

Moscow Aviation Institute (National Research University)
4 Volokolamskoe Highway, Moscow, 125993, Russia

✉ Anastasiya D. Shlyaptseva (shlyaptsevaad@mai.ru)

Abstract: This study investigates the impact of titanium addition to the eutectic silumin AK12 melt, considering various methods of addition. The research results encompass the sole introduction of titanium (at a calculated amount of 0.1 wt.%) through different forms/methods, such as the Al–4%Ti ligature, TiO_2 oxide, K_2TiF_6 salt, and Ti sponge. Additionally, the study explores the combined addition of titanium and a standard flux (comprising 62.5 % NaCl + 12.5 % KCl + 25 % NaF). The research involved qualitative and quantitative analyses of macro- and microstructures, spectral analysis data, and mechanical properties (tensile strength and relative elongation) of the alloys. The findings highlight that titanium has a positive influence on the structure of eutectic silumin, with the most effective results achieved when combined with the standard flux. However, the efficiency of silumin modification with titanium varies depending on the method of addition. Specifically, the introduction of titanium in the form of K_2TiF_6 fluoride salt, Al–4%Ti ligature, and titanium sponge positively affected macro grain refinement, reduced the spacing between the secondary dendrite arms of the solid solution (α-Al), and enhanced the dispersion of eutectic silicon. The most promising approach for complex silumin modification involves the joint introduction of titanium-containing substances and a sodium salt-based flux. This combination has a multifaceted impact on the silumin structure, leading to the simultaneous modification of various structural components in aluminum–silicon alloys. Depending on the type of titanium-containing substance, when processed alongside flux, the alloy achieves a relative elongation ranging from 9.7 % to 11.1 %, exceeding the same parameter for the unmodified alloy by more than 4 times and surpassing the sodium-modified alloy's relative elongation by 17–37 %. Furthermore, the ultimate strength reaches levels of 171–193 MPa, representing a 22–38 % improvement compared to the unmodified alloy and a 7–21 % increase compared to the sodium-modified alloy.

Keywords: cast aluminum alloys, titanium, sodium, complex modification, eutectic silicon, solid solution, macro- and microstructure, spectral analysis.

For citation: Shlyaptseva A.D., Petrov I.A., Ryakhovskiy A.P. Influence of various titanium-containing additives on the modification efficiency of aluminum–silicon eutectic alloy. *Izvestiya. Non-Ferrous Metallurgy.* 2023;29(5):47–56. https://doi.org/10.17073/0021-3438-2023-5-47-56

Влияние различных титансодержащих добавок на эффективность модифицирования эвтектического сплава системы алюминий–кремний

А.Д. Шляпцева, И.А. Петров, А.П. Ряховский

Московский авиационный институт (национальный исследовательский университет)
125993, Россия, г. Москва, Волоколамское шоссе, 4

✉ Анастасия Дмитриевна Шляпцева (shlyaptsevaad@mai.ru)

Аннотация: Изучено влияние титана, в зависимости от способа его ввода в расплав, на структуру и механические свойства эвтектического силумина АК12. Приведены результаты исследований как при одиночном введении титана (расчетное содержание Ti – 0,1 мас.%) различными способами (лигатурой Al–4%Ti, оксидом TiO_2, солью K_2TiF_6, Ti-губкой), так и при совместных добавках титана и стандартного флюса (62,5 % NaCl + 12,5 % KCl + 25 % NaF). Исследования осуществляли путем качественного и количественного анализа макро- и микроструктур сплавов, данных спектрального анализа и механических свойств (предела

прочности на разрыв и относительного удлинения). Установлено, что титан оказывает влияние на структуру эвтектического силумина и наиболее эффективен при совместном введении со стандартным флюсом. При этом эффективность модифицирования силуминов титаном зависит от способа его ввода в расплав. Отмечено положительное влияние титана, введенного с помощью фтористой соли K_2TiF_6, лигатуры Al–4%Ti и титановой губки, на измельчение макрозерна, уменьшение расстояния между ветвями дендритов второго порядка твердого раствора (α-Al), а также на диспергирование эвтектического кремния. Наиболее перспективным способом комплексного модифицирования силуминов является совместное введение титансодержащих веществ и флюса на основе солей натрия. Такие составы оказывают комплексное влияние на структуру силумина, заключающееся в одновременном модифицировании различных структурных составляющих алюминиево-кремниевых сплавов. В зависимости от вида титансодержащего вещества при совместной обработке с флюсом относительное удлинение сплава достигает 9,7–11,1 %, что более чем в 4 раза превышает этот показатель для немодифицированного сплава и на 17–37 % выше, чем у сплава, модифицированного натрием. Предел прочности составляет 171–193 МПа, что на 22–38 % больше, чем у немодифицированного сплава, и на 7–21 % выше по сравнению со сплавом, модифицированным натрием.

Ключевые слова: литейные алюминиевые сплавы, титан, натрий, комплексное модифицирование, эвтектический кремний, твердый раствор, макро- и микроструктура, спектральный анализ.

Для цитирования: Шляпцева А.Д., Петров И.А., Ряховский А.П. Влияние различных титансодержащих добавок на эффективность модифицирования эвтектического сплава системы алюминий–кремний. *Известия вузов. Цветная металлургия*. 2023;29(5):47–56. https://doi.org/10.17073/0021-3438-2023-5-47-56

Introduction

Aluminum—silicon alloys find widespread applications in various industries such as aircraft and automotive due to their suitability for producing intricate castings. Their excellent casting properties enable the creation of complex, thin-walled, and impermeable castings. However, a disadvantage of these silumin alloys is their relatively low mechanical properties in sand casting, primarily attributed to the development of a coarse microstructure in the alloy. It is worth noting that Al-Si cast alloys are typically used for sand casting only in a modified form [1; 2].

In order to enhance modification, surfactants like sodium and strontium are introduced into the melt of pre-eutectic and eutectic silumins [1; 2]. These modifying additives have the effect of refining eutectic silicon particles, causing them to adopt a globular shape during crystallization. Consequently, the mechanical properties of the alloy, especially its relative elongation, improve.

For refining the grains in the solid aluminum-based (α-Al) solution, crystal-nucleating elements such as Ti, Zr, and Sc are added to the melt of deformable and foundry aluminum alloys, including silumins [1; 3; 4]. Notably, the efficiency of grain refinement in deformable alloys differs from that in pre-eutectic silumins. This discrepancy is due to the known fact that increased silicon content in the alloy reduces the degree of grain refinement [5].

Among the various modifiers for α-Al in aluminum-based alloys, titanium is recognized as one of the most effective, particularly for pre-eutectic alloys with silicon content less than 7 % [1]. When introduced into the melt in the range of 0.05—0.15 %, titanium leads to the formation of additional $TiAl_3$ crystallization centers resulting in the refinement of α-Al solid solution grains and significant improvements in the casting and mechanical properties of the alloys [1; 6].

However, the existing scientific and technical literature provides contradictory information regarding the modifying impact of titanium (up to 0.2 wt.%) on pre-eutectic (containing more than 7 % Si) and eutectic silumins. It is generally believed that the modification of such alloys with titanium should not yield significant structural refinement, as titanium primarily modifies α-Al dendrites, while the key structural component determining the complex mechanical properties of silumins is the silicon eutectic [7; 8].

Moreover, as demonstrated in [3; 9—11], a substantial amount of silicon (7—13 wt.%) diminishes the grain refinement efficacy of titanium-modified casting Al—Si alloys. This phenomenon can be explained by the formation and growth of TiAlSi intermetallides, such as $(Al,Si)_3Ti$ and $(Al,Si)_2Ti$, in the melt. Consequently, the number of $TiAl_3$ particles, which act as crystallization centers, decreases.

Nonetheless, there is a discernible beneficial impact of titanium on the structure of both pre- and eutectic silumins, as documented in [12—17]. For instance, in [12], the influence of titanium introduced through the Al—5Ti alloy on the structure and mechanical properties of the Al—10%Si alloy was investigated. The study revealed that the addition of 0.5 wt.% Al—5Ti contributes to the refinement of dendrites (α-Al) and leads to a maximum increase in the solid solution fraction across thin sections. Consequently, the tensile strength and relative elongation of the alloy increase by 9 % and 49 %, respectively, compared to the unmodified alloy.

In [13; 14], the favorable impact of titanium introduced via Al—10%Ti and Al—5%Ti—1%B alloys, combined with strontium, on grain (α-Al) refinement in the Al—7%Si—Mg alloy was demonstrated. Comprehensive treatment of the melt with titanium and strontium amplifies the degree of refinement of eutectic silicon particles compared to using Sr alone. As described in [2], this effect arises because the silicon eutectic undergoes a modified transformation; being a solidified phase, it crystallizes within the restricted space between dendrite arms, and the spacing between them decreases under the influence of the modifier (titanium).

Titanium also synergizes effectively with eutectic silicon modifiers like sodium [17], strontium [13; 14; 18], barium [19; 20], and more. Consequently, titanium-containing additives, such as the K_2TiF_6 salt and titanium dioxide TiO_2 are components of certain complex modifying fluxes for silumins, exerting influence on various structural components of the alloys [19; 20].

The objective of the research was to examine the impact of titanium on the structure and properties of eutectic silumin, contingent on the method of its introduction into the melt. Various introduction methods were studied, including the use of the Al—4%Ti alloy; titanium sponge; K_2TiF_6 salt; and titanium dioxide TiO_2. Additionally, we investigated the effects of titanium-containing additives when introduced in combination with a standard flux for modifying the eutectic in silumins with the following composition, %: 62.5NaCl + 12.5KCl + + 25NaF.

Materials and methods of research

Silumin of eutectic composition AK12, whose chemical composition was as follows (wt.%) according to the spectral analysis data, was chosen as a model alloy:

Al	Base	Ti	0.0031
Si	11.53	Zn	0.0092
Cu	0.0021	Mo	0.0026
Mg	0.0006	Fe	0.358
Mn	0.0026		

Titanium-containing additives were utilized for the modification of silumins. These additives included the following: titanium dioxide TiO_2 (TU 6-10-1356-73), the Al—4%Ti ligature (GOST 11739.20-99), the K_2TiF_6 salt (TU 20.13.62-023-69886968-2017), titanium sponge of TG-90 grade (GOST 17746-79), as well as standard flux 62.5 % NaCl (GOST 4233-77) + 12.5 % KCl (GOST 4568-95) + 25 % NaF (GOST 4463-76) [21]. The quantity of introduced Ti additives was determined based on a calculation aiming for a titanium content of 0.1 wt.%. When introducing titanium sponge, an allowance of 5 % for carbon monoxide was considered, and the standard flux was added at a rate of 1.5 % of the melting mass.

Before melting, fluoride and chloride salts (NaF, KCl, NaCl, K_2TiF_6) and titanium dioxide powder underwent a drying process at t = 150÷200 °C for 2 h to eliminate moisture.

Experimental melting was conducted within an electric resistance furnace, and each experiment was repeated 3 times.

The treatment of the melt with the Al—4%Ti ligature and titanium sponge occurred at t = 740 and 800 °C, respectively. After mixing, dissolution, and holding, the melt underwent degassing with argon.

Complex treatment involving the Al—4%Ti ligature and standard flux, as well as with titanium sponge and standard flux, was performed sequentially. Initially, the melt was treated with the ligature at t = 740 °C, and the sponge applied at t = 800 °C. Afte mixing and holding, standard flux was introduced at t = 740 °C.

When the melt was treated with the K_2TiF_6 salt, standard flux and titanium dioxide TiO_2, the melt was pre-degassed with argon, and then additives were poured on the melt surface at t = 750, 740 and 780 °C, respectively.

Complex treatment involving standard flux and the K_2TiF_6 salt was executed sequentially. First, the melt was treated with standard flux at t = 740 °C, and then, after mixing and holding, the K_2TiF_6 salt was introduced at t = 750 °C. Complex treatment with titanium dioxide and standard flux was performed concurrently at t = 780 °C.

After the treatment with additives, the melt was allowed to stand for 15 min, and slag was removed from the surface. Samples for mechanical tests were cast into a sand—clay mold at t = 710 °C.

The determination of mechanical properties (tensile strength and relative elongation) was conducted using the Instron 5982 testing system (USA).

For the evaluation of the macro- and microstructure of the AK12 alloy samples, thin sections were prepared according using established methods. Thin macro sections were etched with the 10 % copper chloride solution and clarified in concentrated nitric acid.

Micrographical investigations were carried out using an all-purpose Olympus GX51 research microscope (Olympus Corp., Japan) equipped with the Image-Pro image analyzer (Instron, USA).

The dispersion capacity of the eutectic was assessed by measuring the average length of silicon particles

within ($\bar{l}_{Si}$). The average grain size ($\bar{d}$) was determined using the random secant method, calculated as the ratio of the secant length to the number of secant intersections with grain boundaries. In order to analyze the distribution of solid solution dendrites across the thin section area, the secondary dendrite arm spacing (SDAS) was determined ($\bar{\lambda}_2$) [22]. In order to ensure the accuracy of the analysis, a minimum of 50 measurements were conducted, and the resulting values were averaged. Statistical analysis of the research results for both the average length of silicon particles and the average grain size was carried out using Statistica 10 software.

The chemical (elementary) composition of the tested samples was examined utilizing a Q4 TASMAN-170 spark optical emission spectrometer (Bruker Quantron GmbH, Germany).

Results and discussion

The research results demonstrate that the introduction of titanium through titanium-containing additives significantly impacts the properties and structure of the AK12 alloy (Fig. 1).

An enhancement in the mechanical properties of the alloy and the refinement of its structural components are observed with the introduction of all compounds, except when titanium dioxide is introduced alone, and no titanium transition into the alloy occurs (Fig. 1, *e*).

For single introductions of titanium sponge, ligature, and salt, there is a noticeable increase in mechanical properties compared to the initial alloy: the relative elongation (δ) increases by 2.5, 2.2 and 3.1 times, respectively, while the ultimate strength (σ_u) increases by 24, 19, and 25 %, respectively.

Based on the spectral analysis data (Fig. 1, *c*), it is evident that when each of the considered titanium-containing additives is used, a high degree of assimilation of the modifying element by the melt occurs: the titanium yield from the ligature is 100 %, and the yield from the salt and sponge is 80 %.

The improvement in the mechanical properties of the alloy is a result of structural modification. According to qualitative (Fig. 2) and quantitative (Fig. 1, *d*—*f*) structural analysis data, the modification of the AK12 alloy through titanium-containing additives primarily leads to a reduction in the spacing between the secondary dendrite arms ($\bar{\lambda}_2$) of the aluminum-based (α-Al) solid solution (Fig. 1, *e*).

As a consequence of this modification, the dendrites acquire a more compact morphology. Compared to the original alloy, $\bar{\lambda}_2$ decreases by a factor of 1.5—2.0 (Fig. 2, *c2*, *d2*, *e2*). Titanium also promotes macro-grain refinement, resulting in a reduction of more than 5 times (Fig. 1, *d*; Fig. 2, *c3*, *d3*, *e3*).

Nonetheless, titanium introduced via the ligature, titanium sponge, and K_2TiF_6 salt not only influences the solid solution (α-Al) dendrites and macro-grain but also leads to a reduction in the average size of silicon within the eutectic (Fig. 2, *c1*, *d1*, *e1*). Compared to the original alloy, the average silicon size is reduced by a factor of 1.5, 2.5, and 3.5, respectively (Fig. 1, *f*). Modification with titanium-containing substances refines the α-Al dendrites, narrows the inter-dendrite spacing, and subdivides the eutectic into micro-volumes situated within the inter-arm spaces. The eutectic solidifies within a more confined space between dendrite arms, and the silicon refinement occurs due to the restriction of its growth within these micro-volumes. This hypothesis aligns with findings in [23; 24].

The K_2TiF_6 salt plays a significant role in refining the eutectic compared to other titanium-containing additives. It is presumed that this heightened effectiveness is due to the additional influence of potassium, which is present in the salt and acts as a eutectic surfactant [25]. The additional impact of the sponge on the refinement of eutectic silicon is likely a result of the extended holding time of the alloy (>30 min) at elevated temperatures (>780 °C) [26].

In order to investigate the combined effect of titanium addition, it was introduced simultaneously with a sodium and potassium salt-based flux. The standard Na-containing flux is commonly used for eutectic modification in silumins [1; 2]. According to the adsorption theory of modification, sodium, as a surfactant, adsorbs onto the surface of growing silicon crystals, slowing their growth. This process leads to the formation of a finely modified structure within the alloy under supercooled conditions.

The relative elongation of the AK12 alloy, modified with the Na-containing flux, exceeds that of all previously studied titanium-containing additives, reaching a value of 8.1 %, which is 3 times higher than without modification. The flux has a modifying effect on eutectic silicon (Fig. 3, *a1*) but does not influence the SDAS and macro grain diameter (Fig. 3, *a2*, *a3*).

The concurrent introduction of flux and titanium-containing additives, such as titanium dioxide TiO_2, ligature, and K_2TiF_6 salt, results in an even more significant improvement in properties. In comparison to treatment with sodium-containing flux, δ was found to be higher by 36 %, 37 %, and 20 %, and σ_u by 10 %, 7 %, and 21 %, respectively. The combination of titanium sponge with flux also enhances properties but to a lesser extent, with δ being higher by 17 % and σ_u by 7.5 %.

The increased mechanical properties of the alloy are attributed to the structural refinement, especially of the dendrites of the solid solution (α-Al) (Fig. 3, *b2*, *c2*, *d2*, *e2*), and the macrostructure (Fig. 3, *b3*, *c3*, *d3*, *e3*). Consequently, the addition of titanium-containing additives to the flux has minimal impact on the degree of eutectic silicon refinement (Fig. 3, *b1*, *c1*, *d1*, *e1*). When modified with sodium and titanium, as well as sodium alone, the eutectic silicon takes on a globular, highly refined form (compared to the original alloy, the average length of silicon particles decreases by 10—20 times). The inclusion of Ti-containing

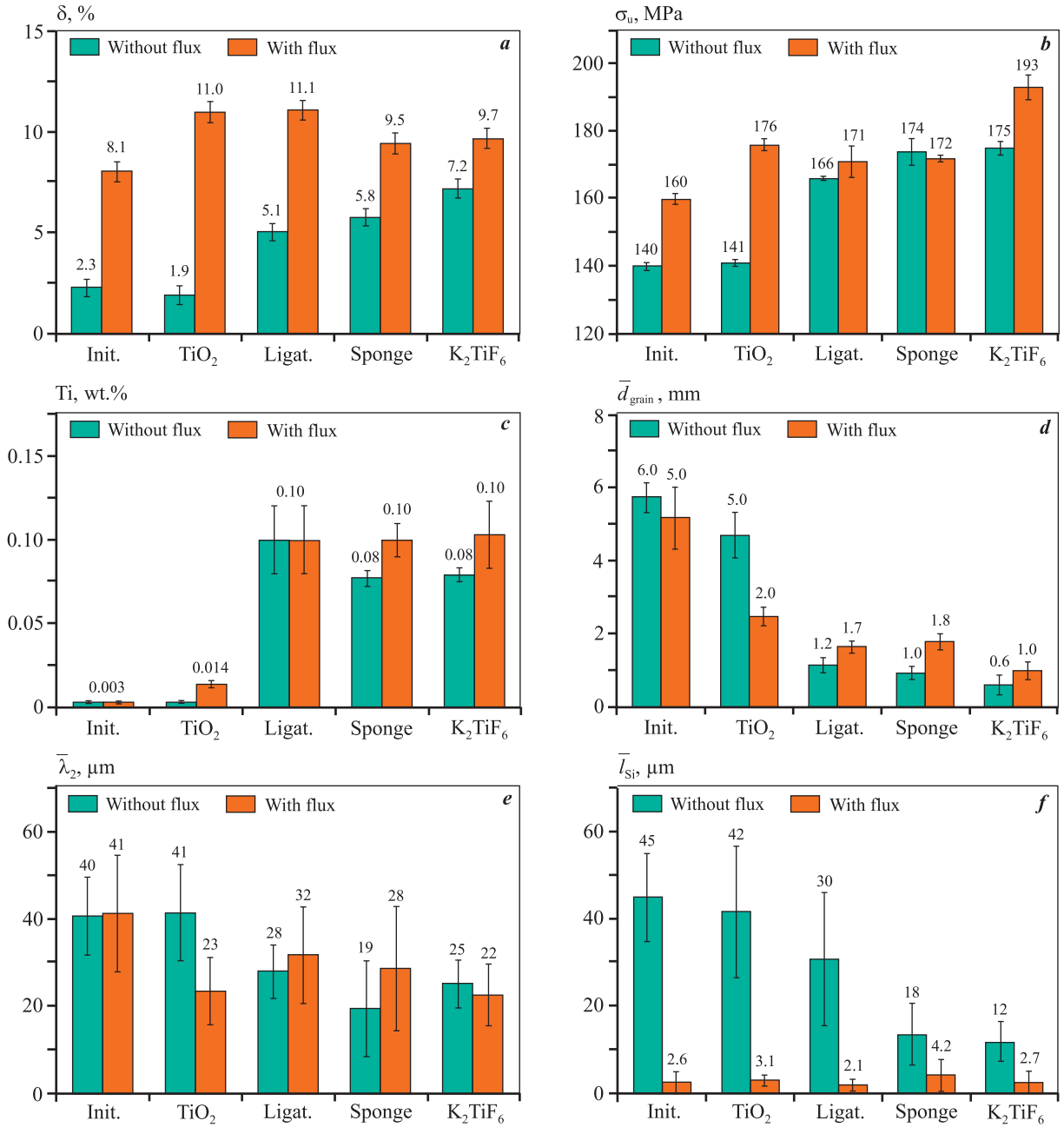

Fig. 1. The influence of different titanium introduction methods on the mechanical properties and structural parameters of the AK12 alloy

a – relative elongation; ***b*** – tensile strength; ***c*** – titanium content in the alloy according to spectral analysis data; ***d*** – average diameter of the macro grain; ***e*** – average secondary dendrite arm spacing; ***f*** – average length of eutectic silicon particles

Рис. 1. Влияние способов ввода титана на механические свойства и параметры структуры сплава АК12

a – относительное удлинение; ***b*** – предел прочности на разрыв; ***c*** – содержание титана в сплаве, по данным спектрального анализа; ***d*** – средний диаметр макрозерна; ***e*** – среднее расстояние между дендритными осями второго порядка; ***f*** – средняя длина частиц эвтектического кремния

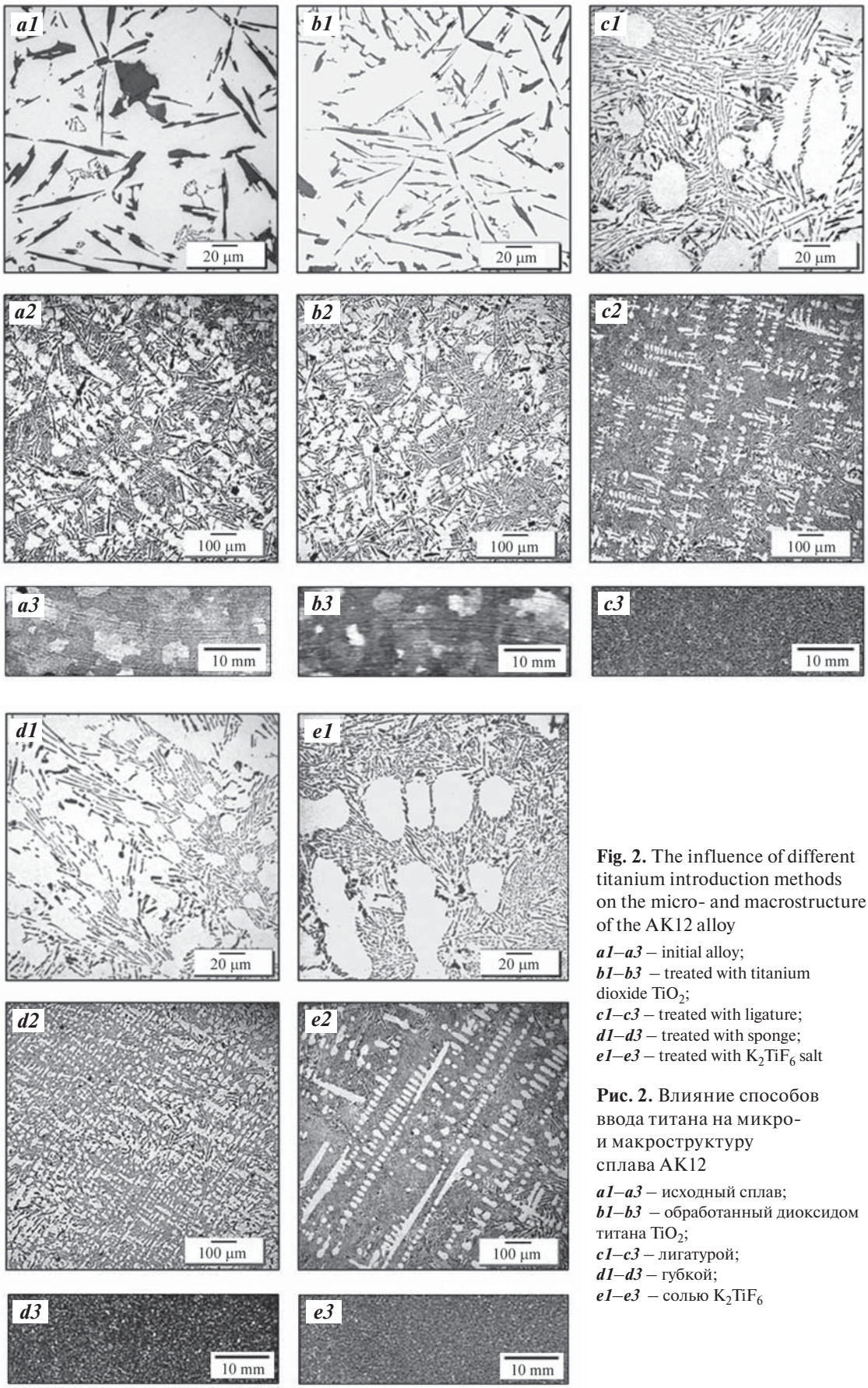

Fig. 2. The influence of different titanium introduction methods on the micro- and macrostructure of the AK12 alloy

a1–a3 – initial alloy;
b1–b3 – treated with titanium dioxide TiO_2;
c1–c3 – treated with ligature;
d1–d3 – treated with sponge;
e1–e3 – treated with K_2TiF_6 salt

Рис. 2. Влияние способов ввода титана на микро- и макроструктуру сплава АК12

a1–a3 – исходный сплав;
b1–b3 – обработанный диоксидом титана TiO_2;
c1–c3 – лигатурой;
d1–d3 – губкой;
e1–e3 – солью K_2TiF_6

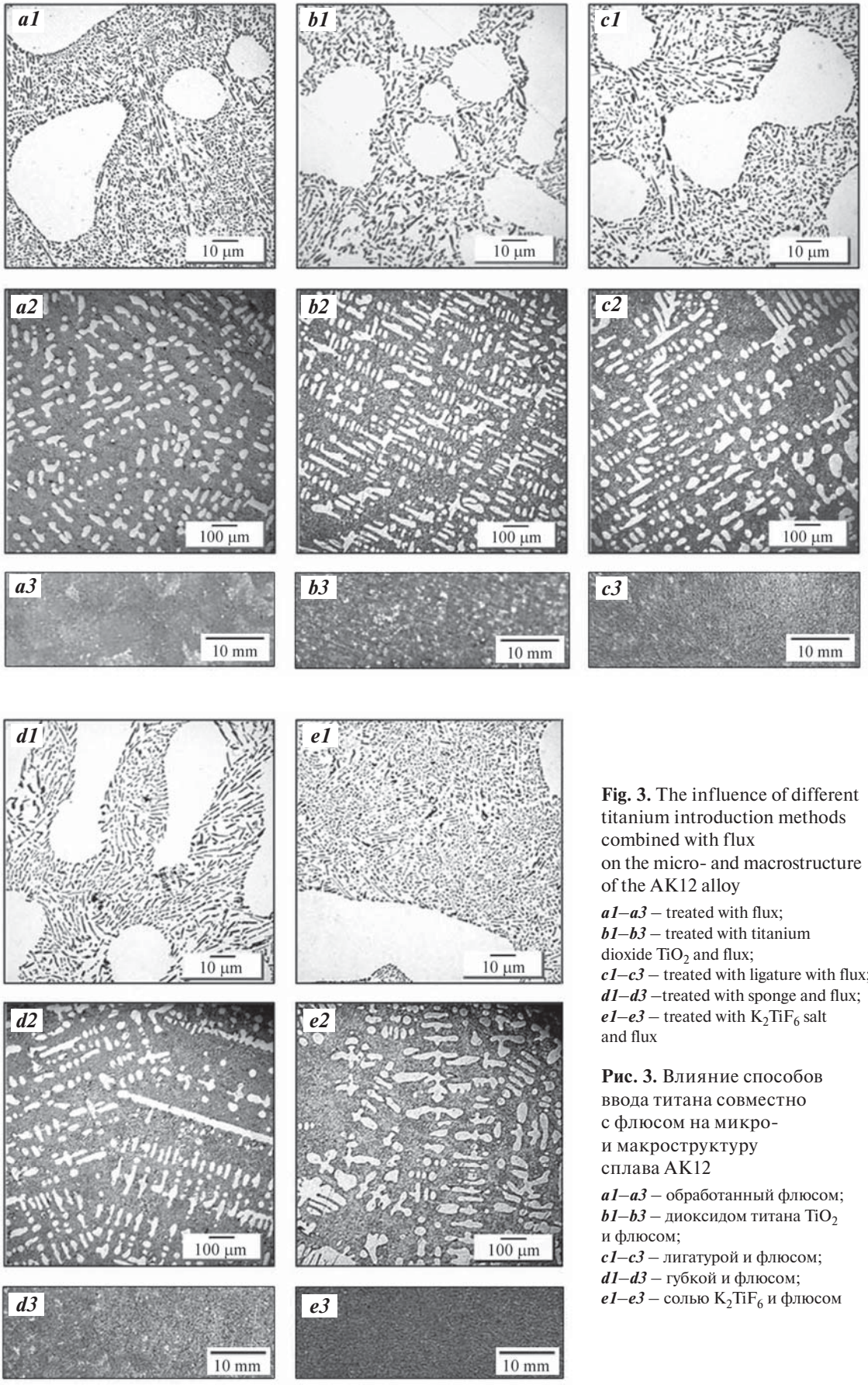

Fig. 3. The influence of different titanium introduction methods combined with flux on the micro- and macrostructure of the AK12 alloy

a1–a3 – treated with flux;
b1–b3 – treated with titanium dioxide TiO_2 and flux;
c1–c3 – treated with ligature with flux;
d1–d3 –treated with sponge and flux;
e1–e3 – treated with K_2TiF_6 salt and flux

Рис. 3. Влияние способов ввода титана совместно с флюсом на микро- и макроструктуру сплава АК12

a1–a3 – обработанный флюсом;
b1–b3 – диоксидом титана TiO_2 и флюсом;
c1–c3 – лигатурой и флюсом;
d1–d3 – губкой и флюсом;
e1–e3 – солью K_2TiF_6 и флюсом

additives in the sodium flux reduces the dendrite arm spacing by 1.3—1.9 times (Fig. 1, *e*), the macro grain diameter by 2—4 times (Fig. 1, *d*), and subsequently improves the alloy's properties.

The standard flux enhances the yield of titanium from titanium dioxide, increasing it from 0 to 14 % in the melt. This effect can be explained by the fact that the fluoride—chloride flux reduces interfacial tension and improves the wetting of solid oxide particles by the melt [27; 28]. Additionally, titanium dioxide dissolves in fluoride salts, leading to aluminothermal reduction of titanium dioxide to titanium in the silumin melt and, consequently, enhanced assimilation of titanium by the melt [17].

Undoubtedly, a significant benefit of modifying silumins with titanium is the sustained duration of the modifying effect. Previous studies have shown that titanium introduced with K_2TiF_6 [20] and TiO_2 [19], at a content of 0.05—0.15 % depending on the composition of complex fluxes, maintains its modifying effect for up to 5 hours and through several remeltings.

Conclusion

1. The positive impact of using titanium for the modification of eutectic silumin has been conclusively demonstrated. Titanium, at levels of 0.05—0.1 wt.%, has a favorable effect on the structure and mechanical properties of the AK12 alloy. However, the extent of these properties and the degree of structural modification depend on the method of titanium introduction. When introduced without flux, the use of the K_2TiF_6 salt for introduction is the most effective.

2. The positive influence of titanium, introduced with the K_2TiF_6 salt, Al—4%Ti ligature, and Ti sponge, has been observed in terms of macro grain refinement, the reduction of spacing between secondary dendritic arms in the α-solid solution, and the dispersion of eutectic silicon within the AK12 alloy.

3. The most effective method of introducing titanium into the silumin melt is through joint introduction with titanium-containing substances and a sodium salt-based flux, at a rate of 0.1 % Ti and 1.5 % flux relative to the melting mass. This combination has a complex effect on the silumin structure, involving simultaneous macro grain refinement, the reduction of spacing between secondary dendritic arms of the solid solution (α-Al) facilitated by titanium, and the refinement and enrichment of silicon in the eutectic with sodium. As a result, the modified AK12 alloy, when cast into a sand—clay mold, achieves a relative elongation of 9.5—11.1 % and an ultimate strength is 171—193 MPa.

References

1. Napalkov V.I., Makhov S.V., Pozdnyakov A.V. Modification of aluminium alloys. Moscow: MISIS, 2017. 348 p. (In Russ.).
Напалков В.И., Махов С.В., Поздняков А.В. Модифицирование алюминиевых сплавов. М.: МИСиС, 2017. 348 с.
2. Nikitin K.V. Modification and complex processing of silumins. Samara: Samarskii gosudarstvennyi tekhnicheskii universitet, 2016. 92 p. (In Russ.).
Никитин К.В. Модифицирование и комплексная обработка силуминов. Самара: Самар. гос. техн. ун-т, 2016. 92 с.
3. Easton M.A., Qian M., Prasad A., StJohn D.H. Recent advances in grain refinement of light metals and alloys. *Current Opinion in Solid State and Materials Science*. 2016;20(1):13—24. https://doi.org/10.1016/j.cossms.2015.10.001
4. Feng Gao, Zhongyun Fan. Solute effect on grain refinement of Al- and Mg-alloys: An overview of the recent advances made by the LiME research hub. *Metals*. 2022;12(9):1488. https://doi.org/10.3390/met12091488
5. Joachim Gröbner, Djordje Mirković, Rainer Schmid-Fetzer. Thermodynamic aspects of grain refinement of Al—Si alloys using Ti and B. *Materials Science and Engineering: A*. 2005;395(1):10—21. https://doi.org/10.1016/j.msea.2004.11.048
6. Ahmad Mostafa. Mechanical properties and wear behavior of aluminum grain refined by Ti and Ti + B. *International Journal of Surface Engineering and Interdisciplinary Materials Science*. 2019;7(1):1—19. https://doi.org/10.4018/IJSEIMS.2019010101
7. Belov N.A., Alabin A.N., Karacharova E.G., Emelina N.B. Appropriateness of doping silumins with titanium and zirconium additives. *Russian Journal of Non-Ferrous Metals*. 2010;51(4):308—315. https://doi.org/10.3103/S1067821210040097
Белов Н.А., Алабин А.Н., Карачарова Е.Г., Емелина Н.Б. О целесообразности легирования силуминов добавками титана и циркония. *Известия вузов. Цветная металлургия*. 2010;(4):46—52.
8. Belov N.A. Phase composition of industrial and promising aluminum alloy. Moscow: MISIS, 2010. 511 p. (In Russ.).
Белов Н.А. Фазовый состав промышленных и перспективных алюминиевых сплавов. М.: МИСиС, 2010. 511 с.
9. Muzaffer Zeren, Erdem Karakulak. Influence of Ti addition on the microstructure and hardness properties of near-eutectic Al—Si alloys. *Journal of Alloys and Compounds*. 2008;450(1-2):255—259. https://doi.org/10.1016/j.jallcom.2006.10.131

10. Himmler David, Randelzhofer Peter, Körner Carolin. Formation kinetics and phase stability of in-situ Al_3Ti particles in aluminium casting alloys with varying Si content. *Results in Materials*. 2020;7:100103. https://doi.org/10.1016/j.rinma.2020.100103
11. Shant Prakash Gupta. Intermetallic compounds in diffusion couples of Ti with an Al—Si eutectic alloy. *Materials Characterization*. 2002;49(4):321—330. https://doi.org/10.1016/S1044-5803(02)00342-X
12. Liu Ya-ling, Wu Chang-jun, Tu Hao, Lu Xiao-wang, Wang Jian-hua, Su Xu-ping. Microstructure and mechanical properties of Al—10Si alloy modified with Al—5Ti. *China Foundry*. 2018;15:405—410. https://doi.org/10.1007/s41230-018-8034-1
13. Golbahar B., Samuel A.M., Doty H.W., Valtierra S., Samuel F.H. Effect of grain refiner on the tensile and impact properties of Al—Si—Mg cast alloys. *Materials & Design (1980—2015)*. 2014;56:468—479. https://doi.org/10.1016/j.matdes.2013.11.058
14. Lee Ji-Young, Lee Jung-Moo, Son Kwang-Suk, Jang Jae-il, Cho Young-Hee. A study on the interaction between a Sr modifier and an Al—5Ti—1B grain refiner in an Al—7Si—0.35Mg casting alloy. *Journal of Alloys and Compounds*. 2023;938:168598. https://doi.org/10.1016/j.jallcom.2022.168598
15. Wu Yuna, Zhang Jianfeng, Liao Hengcheng, Li Gaiye, Wu Yuping. Development of high performance near eutectic Al—Si—Mg alloy profile by micro alloying with Ti. *Journal of Alloys and Compounds*. 2016;660:141—147. https://doi.org/10.1016/j.jallcom.2015.11.083
16. Nikitin K.V., Timoshkin I.Yu., Nikitin V.I. Influence of methods of producing the AlTi master alloy on its structure and efficiency in the grain refinement of aluminum alloy. *Russian Journal of Non-Ferrous Metals*. 2018;59(5):512—519. https://doi.org/10.3103/S1067821218050115
Никитин К.В., Тимошкин И.Ю., Никитин В.И. Влияние способов получения лигатуры AlTi на ее структуру и эффективность при модифицировании алюминиевых сплавов. *Известия вузов. Цветная металлургия*. 2018;(4):45—52.
17. Shlyaptseva A.D., Petrov I.A., Ryakhovskii A.P. Prospects of using titanium dioxide as a component of modifying composition for aluminum casting alloys. *Materials Science Forum*. 2019;946:636—643. https://doi.org/10.4028/www.scientific.net/MSF.946.636
18. Mallapur D.G., Kori S.A., Udupa K.R. Influence of Ti, B and Sr on the microstructure and mechanical properties of A356 alloy. *Journal of Materials Science*. 2011;46:1622—1627. https://doi.org/10.1007/s10853-010-4977-3
19. Shlyaptseva A.D., Petrov I.A., Ryakhovsky A.P., Medvedeva E.V., Tcherdyntsev V.V. Complex structure modification and improvement of properties of aluminium casting alloys with various silicon content. *Metals*. 2021;11(12):1946. https://doi.org/10.3390/met11121946
20. Petrov I.A., Ryakhovskii A. P., Moiseev V.S., Bobryshev B.L., Shlyaptseva A.D. Perspectives for use of carbon-containing materials for treatment of silumins. *Liteishchik Rossii*. 2016;(1):28—32. (In Russ.).
Петров И.А., Ряховский А.П., Моисеев В.С., Бобрышев Б.Л., Шляпцева А.Д. Перспективы использования углеродсодержащего материала для обработки силуминов. *Литейщик России*. 2016;(1):28—32.
21. Galdin N.M., Chernega D.F., Ivanchuk D.F. Casting of non-ferrous alloys: Handbook. Moscow: Mashinostroenie, 1989. 528 p. (In Russ.).
Галдин Н.М., Чернега Д.Ф., Иванчук Д.Ф. Цветное литье: Справочник. М.: Машиностроение, 1989. 528 с.
22. Henk G. Merkus. Particle size measurements: Fundamentals, practice, quality. Springer Science+Business Media, 2009. 534 p.
23. Boom E.A. The nature of modification of alloys of the silumin type. Moscow: Metallurgiya, 1972. 69 p. (In Russ.).
Боом Е.А. Природа модифицирования сплавов типа силумин. М.: Металлургия, 1972. 69 с.
24. Mondolfo L.F. Aluminium alloys, structure and properties, London; Boston: Butterworths, 1976. 971 p.
25. Ashtari P., Tezuka H., Sato T. Modification of Fe-containing intermetallic compounds by K addition to Fe-rich AA319 aluminum alloys. *Scripta Materialia*. 2005;53(8):937—942. https://doi.org/10.1016/j.scriptamat.2005.06.022
26. Deev V.B., Feoktistov A.V., Selyanin I.F., Shvidkov N.I., Zainutdinov K.F. Influence of high-temperature treatment of melt on silumin structure and properties. *Steel in Translation*. 2003;33(10):20—24.
Деев В.Б., Феоктистов А.В., Селянин И.Ф., Швидков Н.И., Зайнутдинов Х.Ф. Влияние режимов высокотемпературной обработки расплавов на формирование структуры и свойства силуминов. *Известия высших учебных заведений. Черная металлургия*. 2003;(10):28—31.
27. Napalkov V.I., Mahov S.V. Alloying and modification of aluminum and magnesium. Moscow: MISIS, 2002. 376 p. (In Russ.).
Напалков В.И., Махов С.В. Легирование и модифицирование алюминия и магния. М.: МИСиС, 2002. 376 с.
28. Zhang G., Lu W., Wu X., Yang B., Tan Y., Xu Z., Tang H., Zeng J., Wang J. A new strategy on designing fluxes for aluminum alloy melt refinement. *Materials*. 2023;16(6):2322. https://doi.org/10.3390/ma16062322

Information about the authors

Anastasiya D. Shlyaptseva – Cand. Sci. (Eng.), Senior Lecturer of the Department 1101, Moscow Aviation Institute (National Research University) (MAI).
https://orcid.org/0000-0001-9081-9930
E-mail: shlyaptsevaad@mai.ru

Igor' A. Petrov – Cand. Sci. (Eng.), Associate Professor of the Department 1101 of MAI.
https://orcid.org/0000-0001-6393-1900
E-mail: petrovia2@mai.ru

Aleksandr P. Ryakhovsky – Cand. Sci. (Eng.), Associate Professor of the Department 1101 of MAI.
https://orcid.org/0009-0005-5444-7558
E-mail: fpk-mati@mail.ru

Информация об авторах

Анастасия Дмитриевна Шляпцева – к.т.н., ст. преподаватель кафедры 1101 Московского авиационного института (национального исследовательского университета) (МАИ).
https://orcid.org/0000-0001-9081-9930
E-mail: shlyaptsevaad@mai.ru

Игорь Алексеевич Петров – к.т.н., доцент кафедры 1101 МАИ.
https://orcid.org/0000-0001-6393-1900
E-mail: petrovia2@mai.ru

Александр Павлович Ряховский – к.т.н., доцент кафедры 1101 МАИ.
https://orcid.org/0009-0005-5444-7558
E-mail: fpk-mati@mail.ru

Contribution of the authors

A.D. Shlyaptseva – defined the research objectives, conducted testing, processed and analyzed the study results, and contributed to writing and preparing the article.

I.A. Petrov – conducted experimental melting and testing, processed and analyzed research results, and contributed to writing and preparing the article.

A.P. Ryakhovsky – processed and analyzed research results and contributed to writing and preparing the article.

Вклад авторов

А.Д. Шляпцева – определение цели работы, проведение испытаний, обработка и анализ результатов исследований, написание и подготовка статьи.

И.А. Петров – проведение экспериментальных плавок и испытаний, обработка и анализ результатов исследований, написание и подготовка статьи.

А.П. Ряховский – обработка и анализ результатов исследований, написание и подготовка статьи.

The article was submitted 03.04.2023, revised 19.06.2023, accepted for publication 23.06.2023

Статья поступила в редакцию 27.04.2023, доработана 06.07.2023, подписана в печать 11.07.2023

UDC 55.09.33
https://doi.org/10.17073/0021-3438-2023-5-57-68

Research article
Научная статья

Investigation into the impact of phase composition on the thermal expansion and mechanical properties of Al–Cu–Li alloys

A.A. Ashmarin[1], M.I. Gordeeva[2], S.Ya. Betsofen[2], A.A. Lozovan[2], R. Wu[3], S.S. Alexandrova[2], A.A. Selivanov[4], A.N. Bykadorov[2], D.A. Prokopenko[2]

[1] **Institute of Metallurgy and Materials Science n.a. A.A. Baikov of the Russian Academy of Sciences**
49 Leninskiy Prosp., Moscow, 119334, Russia

[2] **Moscow Aviation Institute (National Research University)**
4 Volokolamskoe Highway, Moscow, 125993, Russia

[3] **Harbin Engineering University**
145 Nantong Str., Harbin 150001, P.R. China

[4] **All-Russian Research Institute of Aviation Materials of the National Research Center "Kurchatov Institute"**
17 Radio Str., Moscow, 105005, Russia

✉ Sergey Ya. Betsofen (s.betsofen@gmail.com)

Abstract: The study employed high-temperature *X*-ray diffraction, quantitative phase analysis, and tensile mechanical property measurements to investigate the relationship between thermal coefficient of linear expansion (TCLE) and phase composition, along with the average yield strengths and Young's moduli of Al–Cu–Li alloys in three different sheet orientations: 1441, V-1461, V-1469, V-1480, and V-1481. The copper content within the solid solution and the mass fractions of the $T_1(Al_2CuLi)$ and $\delta'(Al_3Li)$ phases were determined using an innovative technique based on measuring the lattice distance of the α solid solution, Vegard's law, and balance equations for the elemental and phase compositions of the alloys. It was observed that as the lithium-to-copper ratio in the alloys increased from 0.32 to 1.12, the proportion of the $\delta'(Al_3Li)$ phase increases from 6.3–8.4 wt.% in V-1481, V-1480 and V-1469 alloys to 16.0–17.3 wt.% in 1441 and V-1461 alloys, accompanied by a decrease in the $T_1(Al_2CuLi)$ phase from 5 to 1 wt.%. This led to an increase in the Young's modulus from 75 to 77 GPa due to higher overall proportion of intermetallic compounds and a reduction in yield strength from 509 to 367 MPa due to the decrease in the T_1 phase. This decrease in yield strength resulted from the fact that the hardening effect of the T_1 phase was 3–4 times greater than that of the δ' phase, and this couldn't be offset by an increase in the total intermetallic compound proportion. The observed increase in Young's modulus indicated that the elastic properties of the intermetallic phases were similar, and the rise in the total fraction of intermetallic compounds compensated for the decrease in the T_1 phase. Furthermore, it was demonstrated that TCLE, as measured based on the thermal expansion of the solid solution, also depended on the characteristics of the intermetallic phases present in the alloy. This expanded the potential interpretations of TCLE measurement results.

Keywords: Al–Cu–Li alloys, quantitative phase analysis, high temperature radiography, TCLE, Young's modulus, yield strength.

Acknowledgments: This work received support from the Russian Science Foundation (Grant No. 23-49-00098) and the National Natural Science Foundation of China (52261135538).

For citation: Ashmarin A.A., Gordeeva M.I., Betsofen S.Ya., Lozovan A.A., Wu R., Alexandrova S.S., Selivanov A.A., Bykadorov A.N., Prokopenko D.A. Investigation into the impact of phase composition on the thermal expansion and mechanical properties of Al–Cu–Li alloys. *Izvestiya. Non-Ferrous Metallurgy.* 2023;29(5):57–68. https://doi.org/10.17073/0021-3438-2023-5-57-68

Исследование влияния фазового состава на термическое расширение и механические свойства сплавов Al–Cu–Li

А.А. Ашмарин[1], М.И. Гордеева[2], С.Я. Бецофен[2], А.А. Лозован[2], R. Wu[3], С.С. Александрова[2], А.А. Селиванов[4], А.Н. Быкадоров[2], Д.А. Прокопенко[2]

[1] **Институт металлургии и материаловедения им. А.А. Байкова РАН**
119334, Россия, г. Москва, Ленинский пр-т, 49

[2] **Московский авиационный институт (национальный исследовательский университет)**
125993, Россия, г. Москва, Волоколамское шоссе, 4

[3] **Harbin Engineering University**
P.R. China, 150001, Harbin, Nantong Str., 145

[4] **Всероссийский научно-исследовательский институт авиационных материалов Национального исследовательского центра «Курчатовский институт»**
105005, Россия, г. Москва, ул. Радио, 17

✉ Сергей Яковлевич Бецофен (s.betsofen@gmail.com)

Аннотация: Методами высокотемпературной рентгенографии, количественного фазового анализа и измерения механических свойств при растяжении определяли корреляционные соотношения характеристик термического коэффициента линейного расширения (ТКЛР) и фазового состава с усредненными значениями по 3-м направлениям в листах пределов текучести и модулей Юнга сплавов системы Al–Cu–Li: 1441, В-1461, В-1469, В-1480 и В-1481. Содержание меди в твердом растворе и массовые доли фаз $T_1(Al_2CuLi)$ и $\delta'(Al_3Li)$ оценивали с помощью оригинальной методики, основанной на измерении периода решетки α-твердого раствора, законе Вегарда и уравнениях баланса элементного и фазового составов сплавов. Показано, что с увеличением отношения лития к меди в сплавах от 0,32 до 1,12 повышается доля $\delta'(Al_3Li)$-фазы от 6,3–8,4 мас.% в сплавах В-1481, В-1480 и В-1469 до 16,0–17,3 мас.% в сплавах 1441 и В-1461 за счет снижения количества $T_1(Al_2CuLi)$-фазы от 5 до 1 мас.%. Это приводит к увеличению модуля Юнга от 75 до 77 ГПа из-за возрастания суммарной доли интерметаллидов и к снижению предела текучести от 509 до 367 МПа из-за уменьшения количества T_1-фазы, поскольку эффект упрочнения T_1-фазы в 3–4 раза превосходит упрочнение от выделения δ'-фазы, что не может быть скомпенсировано повышением суммарной доли интерметаллидов. Тот факт, что модуль Юнга при этом увеличивается, свидетельствует о том, что упругие свойства интерметаллидных фаз близки и возрастание суммарной доли интерметаллидов компенсирует снижение количества T_1-фазы. Показано, что величина ТКЛР, измеренная на основании термического расширения твердого раствора, зависит также от характеристик присутствующих в сплаве интерметаллидных фаз, что расширяет возможности интерпретации результатов измерения ТКЛР.

Ключевые слова: сплавы Al–Cu–Li, количественный фазовый анализ, высокотемпературная рентгенография, ТКЛР, модуль Юнга, предел текучести.

Благодарности: Работа выполнена при финансовой поддержке Российского научного фонда (грант № 23-49-00098) и Китайского фонда естественных наук (52261135538).

Для цитирования: Ашмарин А.А., Гордеева М.И., Бецофен С.Я., Лозован А.А., Wu R., Александрова С.С., Селиванов А.А., Быкадоров А.Н., Прокопенко Д.А. исследование влияния фазового состава на термическое расширение и механические свойства сплавов Al–Cu–Li. *Известия вузов. Цветная металлургия.* 2023;29(5):57–68. https://doi.org/10.17073/0021-3438-2023-5-57-68

Introduction

The thermal coefficient of linear expansion (TCLE) is a critical characteristic for both structural and functional materials. A mismatch in TCLE between phases or components can result in product failure during thermal cycling. Additionally, in materials with non-cubic lattices, TCLE anisotropy becomes a significant concern, potentially leading to inconsistent deformation in grains of different orientations, even within single-phase alloys. Experimental determination of TCLE through high-temperature *X*-ray imaging, as opposed to dilatometry, offers the advantage of measuring TCLE in various phases within multiphase systems [1],

as well as in thin surface layers and coatings [2]. However, when it comes to structural materials, research predominantly focuses on determining TCLE values using the dilatometric method, primarily to address component compatibility issues in composite materials.

It is worth noting that many articles in the field of materials science often use the term "thermal expansion" instead of TCLE, emphasizing the physical aspects rather than solely the engineering considerations of these effects. Several studies in this domain delve into the unique category of modern materials characterized by negative (negative thermal expansion — NTE) or small positive (low positive thermal expansion — PTE) thermal expansion [3—5]. This phenomenon is achieved due to the strong anisotropy of interatomic bonding forces, causing TCLE to be negative along some crystallographic directions and positive along others. Consequently, the volumetric TCLE within a certain temperature range is considered as zero thermal expansion ($<1\cdot10^{-6}$ K^{-1}). This effect has been observed in materials such as CrB_2 [3], $Hf_{0.80}Ta_{0.20}Fe_{2.5}$ [4], $Nb_{14}W_3O_{44}$ [5].

This effect is most pronounced in graphite, where the combination of negative TCLE values within the plane of the basis and high positive TCLE values along the "*c*" axis results in significant stress at the interfaces of crystallites with different orientations during thermal cycling. This stress leads to premature material failure. To address this issue, the use of isotropic, isostatically molded graphite has been proposed [6]. Furthermore, research has shown that TCLE anisotropy can be mitigated by utilizing nanographite in the form of carbon nanowalls [7].

In another study [8], the influence of temperature ranging from 25 to 1150 °C on the phase and structural state of NiCrAlY coatings obtained through plasma sputtering was investigated using high-temperature *X*-ray diffraction. This research provided insights into the conditions of metallic and intermetallic phases (γ-Ni, γ′-Ni_3Al, β-NiAl and α-Cr), but also on the oxidation of the coating, including the formation of thermally growing oxides (TGO).

In [9], an innovative approach was proposed to enhance the fracture toughness of α-Al_2O_3 ceramics. This involved creating a layered composite with alternating textureless and textured layers, each characterized by different TCLE values. The authors attributed the improved fracture resistance of the layered composite to the stress state controlled by the TCLE gradient, which holds promise for enhancing the plastic characteristics of ceramics.

For efficient cooling systems with high heat dissipation capacity, a W—Cu composite was developed [10]. This composite combines the high thermal conductivity of Cu with a reduced TCLE (~$10\cdot10^{-6}$ K^{-1}) due to the presence of W. This reduction in TCLE makes it compatible with the TCLE of electronic components. High-temperature synchrotron radiation was employed to determine TCLE, including the anisotropy of TCLE, of tetragonal lattice anatase nanoparticles doped with Al, In, In + Cr, and Ag + Cr [11]. Additionally, first-principles TCLE calculations were performed, showing good agreement with experimental data for Cu (isotropic case) and AlN (anisotropic case) [12].

Unfortunately, there is limited literature focusing on the use of thermal expansion for metallurgical purposes. While magnesium alloys offer several advantages, their high TCLE ($26\cdot10^{-6}$ K^{-1}), restricts their use in electronics. Consequently, research is actively exploring alloying elements that can reduce the TCLE of magnesium [13—15]. For example, a study demonstrated that the addition of 4 wt.% Si reduces the TCLE of pure Mg from $26\cdot10^{-6}$ to $17.98\cdot10^{-6}$ K^{-1} due to the formation of the Mg_2Si phase with a low TCLE value of $7{,}5\cdot10^{-6}$ K^{-1}. In the case of VNS9-Sh TRIP steel, research [16] revealed a decomposition of approximately 40 % of austenite within a surface layer of about 5 μm, resulting in significant compressive stresses. To understand these processes in thin layers, determining TCLE values of α and γ phases in TRIP steel under different thermomechanical conditions is crucial [17].

A promising approach for analyzing multiphase systems is demonstrated in a study [1], where TCLE measurements of solid solutions, silicon, and six intermetallic phases in foundry alloys such as Al—9.5Si—5.1Cu—0.5Fe, Al—12.5Si—3.9Cu—2.8Ni—0.7Mg—0.4Mn, Al—9.6Si—4.4Ni—0.5Fe, Al—9.5Si—2.5Mn—0.5Fe were conducted using high-temperature *X*-ray radiography (from room temperature to 400 °C). Importantly, the alloy compositions were carefully selected to ensure distinct diffraction from intermetallic compounds, enabling the determination of TCLE values along different crystallographic axes of tetragonal Al_2Cu, monoclinic Al_9FeNi, hexagonal Al_3Ni_2, orthorhombic Al_3Ni, and trigonal Al_7Cu_4Ni. This allowed for the identification of correlations not only related to the mismatch between TCLE values of intermetallic compounds and the matrix but also to their anisotropy. The results from this study [1] highlight that TCLE compatibility issues are relevant not only for substrate coatings and composite

components but also for solid solutions and intermetallic particles. Moreover, investigating the relationships between TCLE values and the mechanical and service properties of alloys and coatings is of great importance.

Al—Li alloys are extensively utilized in aerospace applications owing to their unique blend of low density, necessary strength, and exceptionally high elastic modulus values in comparison to other aluminum alloys [18]. Currently, research is advancing in the direction of developing a new generation of materials for aircraft construction: laminated aluminous-glass plastics (SIALs) based on the Al—Cu—Li system. This innovation is projected to enhance the elastic modulus by 8—10 % while reducing the density of SIALs by 5—7 % [19; 20]. Nevertheless, optimizing alloy compositions to achieve maximum strength or elastic properties encounters methodological challenges in estimating elastic properties. In this context, exploring correlations between the elastic moduli and TCLE values of Al—Cu—Li alloys holds promise.

This paper examines the relationships between TCLE characteristics and the properties of Al—Cu—Li alloys. Such investigations can broaden the applicability of the TCLE measurement method concerning the study and prediction of the structural phase state and properties of these materials.

1. Materials and methods

1.1. Materials

The materials employed in this study comprised sheets of Al—Cu—Li alloys with thicknesses ranging from 1 to 3 mm. Specifically, the alloys examined included 1441, V-1461, V-1469, V-1480, and V-1481 variants. Table 1 provides the composition details of the primary alloying elements (Cu and Li). These sheets were manufactured through rolling processes at OAO "KUMZ" (Kamensk—Uralsky). Subsequently, they underwent a series of heat treatments, including: hardening via cooling in cold water, straightening, and artificial ageing with either, two, or three stages. Al—Li alloy samples were tested using a Zwick/Roell KAPPA 50DS testing machine (Germany) equipped with a force sensor of accuracy class 0.5 and a makroXtens strain gauge (Zwick Roell, Germany) with a 50 mm design length. The testing procedure began with a motion speed of 2 mm/min in the elastic segment, which was subsequently increased to 5 mm/min once the yield strength was determined. Tensile mechanical properties at room temperature were determined according to State Standards GOST 1497 and GOST 11701, and Young's modulus was calculated using regression analysis on a linear segment.

1.2. Methods

X-ray diffraction patterns were recorded using an XRD-600 *X*-ray diffractometer (Shimadzu, Japan) with a HA-1001 high-temperature attachment in an atmospheric environment. Copper radiation was employed with β filtering, and data were collected in the angular range $2\theta = 20 \div 60°$ at temperatures of 20, 100, 150, 200, 300, 400, 500 °C.

In order to determine the lattice period (a) for the reflection (hkl) of a crystal with a cubic lattice at each recording temperature (t_i), the following formula was applied:

$$a_{t_i} = [\lambda/(2\sin\theta)]\sqrt{h^2 + k^2 + l^2}. \quad (1)$$

The TCLE values ($\alpha_{100-500}$) were calculated for the temperature range of 100—500 °C by the least squares method by determining the slope of the straight line in the corresponding coordinates $a_{t_i} - t_i$ (Fig. 1).

2. Results and discussion

Figure 2 illustrates *X*-ray diffraction patterns for five alloys within the Al—Cu—Li system, each distinguished by variations in their Cu and Li content.

These *X*-ray diffraction patterns exclusively display reflections from the FCC α solid solution. Neverthe-

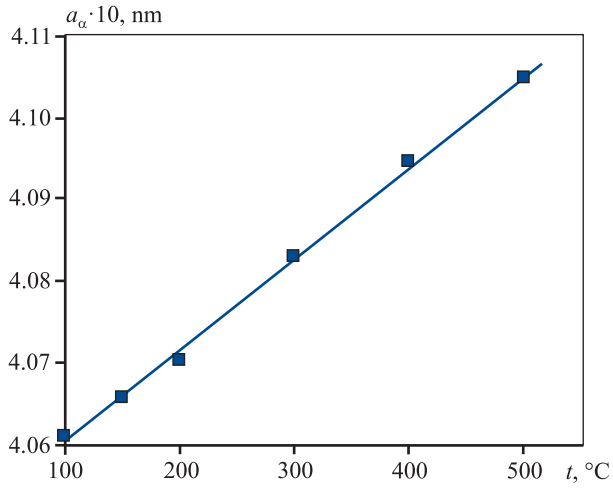

Fig. 1. Lattice distance as a function of *X*-ray temperature for the (111) reflection of the V-1469 alloy

Рис. 1. Зависимость периода решетки от температуры рентгеновской съемки для рефлекса (111) сплава В-1469

less, the relative intensities of these reflections differ across the various alloys. This discrepancy in reflection intensities hints at differences in textures, which play a vital role in explaining the inherent anisotropy of properties characteristic of alloys within this alloying system.

By calculating the lattice periods of the α solid solution based on the position of the reflections in the *X*-ray diffraction patterns, it becomes possible to estimate the copper content within the solid solution and the mass fractions of the $T_1(Al_2CuLi)$ and $\delta'(Al_3Li)$ phases. This estimation is carried out using an innovative technique, as described in [21]. The method relies on measuring the lattice period of an α solid solution, applying Vegard's law, and employing balance equations for the elemental and phase compositions of these alloys. The calculation

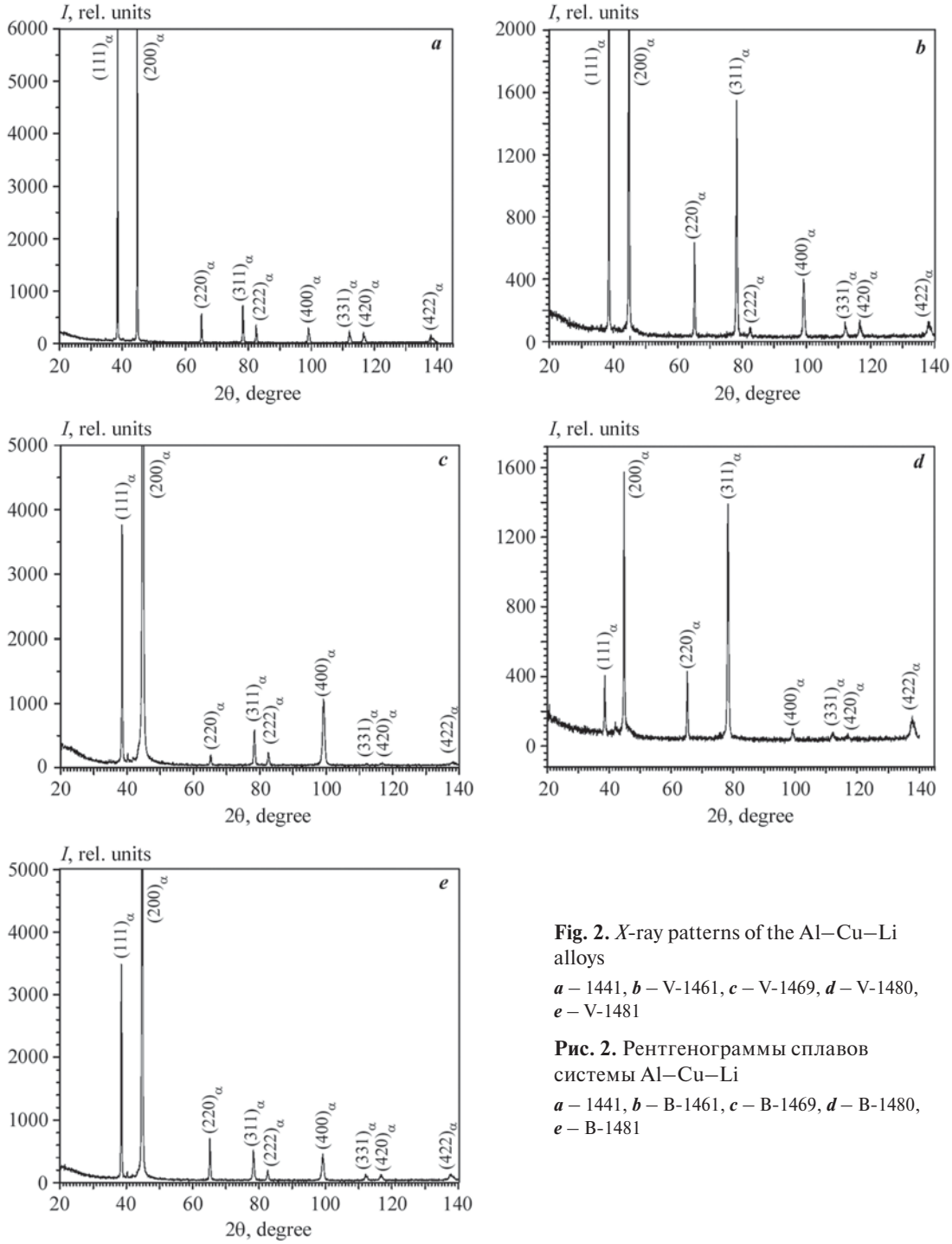

Fig. 2. *X*-ray patterns of the Al–Cu–Li alloys

a – 1441, ***b*** – V-1461, ***c*** – V-1469, ***d*** – V-1480, ***e*** – V-1481

Рис. 2. Рентгенограммы сплавов системы Al–Cu–Li

a – 1441, ***b*** – В-1461, ***c*** – В-1469, ***d*** – В-1480, ***e*** – В-1481

equations for alloys of the Al—Cu—Li system are as follows:

$$W_\alpha = \left[(X^{\delta'}_{Li} - X^{T_1}_{Li})(X^0_{Al}X^{T_1}_{Cu} - X^{T_1}_{Al}X^0_{Cu}) - \right.$$
$$\left. - X^{\delta'}_{Al}X^{T_1}_{Cu}(X^0_{Li} - X^{T_1}_{Li})\right] /$$
$$/ \left[(X^{\delta'}_{Li} - X^{T_1}_{Li})(100X^{T_1}_{Cu} - X^{\alpha}_{Cu}X^{T_1}_{Cu} - X^{T_1}_{Cu}X^{\alpha}_{Li} - X^{T_1}_{Al}X^{\alpha}_{Cu}) - \right.$$
$$\left. - X^{\delta'}_{Al}X^{T_1}_{Cu}(X^{\alpha}_{Li} - X^{T_1}_{Li})\right] \cdot 100,$$

$$W_{T_1} = \frac{100X^0_{Cu} - X^{\alpha}_{Cu}W_\alpha}{X^{T_1}_{Cu}}, \quad (2)$$

$$W_{\delta'} = 100 - W_\alpha - W_{T_1},$$

where X^0_{Al}, X^0_{Cu}, X^0_{Li} represent the concentrations of Al, Cu and Li in the alloy, respectively, wt.%; W_α, W_{T_1}, $W_{\delta'}$ denote the content of the α, T_1 and δ′ phases, respectively, wt.%; X^{α}_{Al}, X^{α}_{Cu}, X^{α}_{Li}, $X^{T_1}_{Al}$, $X^{T_1}_{Cu}$, $X^{T_1}_{Li}$, $X^{\delta'}_{Al}$, $X^{\delta'}_{Li}$ represent the concentrations of Al, Cu and Li in the α, T_1 and δ′ phases, respectively.

The values of $X^{\delta'}_{Li}$, $X^{\delta'}_{Al}$, $X^{T_1}_{Al}$, $X^{T_1}_{Cu}$, $X^{T_1}_{Li}$ are calculated based on the stoichiometry of the $T_1(Al_2CuLi)$ and δ′(Al_3Li) phases.

$$X^{\alpha}_{Cu} = \frac{a_\alpha - a_{Al} - 0{,}01W_\alpha X^0_{Mg}(\Delta a/\Delta X)^{\alpha}_{Mg}}{(\Delta a/\Delta X)^{\alpha}_{Cu}},$$

$0{,}01W_\alpha X^0_{Mg}(\Delta a/\Delta X)^{\alpha}_{Mg}$ is the change in the lattice constant due to presence of magnesium in the solid solution, Å; $(\Delta a/\Delta X)^{\alpha}_{Cu}$ represents the change of the lattice constant by 1 wt.% Cu, Å/wt.%.

Figure 3 provides graphical representations of the dependencies of mass fractions of intermetallic phases for two of the five alloys, specifically 1441 and V-1480. These dependencies reveal a clear trend: as the ratio of lithium content to copper content in the alloy increases, the fraction of the δ′ phase markedly rises, while the fraction of the ternary phase decreases. Table 1 compiles the quantities of intermetallic phases, calculated using Eq. (2), further confirming this pattern.

The ratio X^0_{Li}/X^0_{Cu} increases from 0.32 in the V-1480 alloy to 1.12 in the 1441 alloy. This increase in this ratio results in a higher fraction of the δ′(Al_3Li) phase, ranging from 6.3 to 17.3 wt.%, while reducing the proportion of the $T_1(Al_2CuLi)$ phase from 5 to 1 wt.%. Consequently, the total amount of intermetallic phases increases because the δ′ phase (6.3—17.3 wt.%) significantly outweighs the T_1 phase (1—5 wt.%) in quantity. It is noteworthy that the total amount of intermetallic phases in these alloys is notably greater than in other aluminum alloys. Only in the V-1481 alloy, with a low lithium content of 1 wt.%, does the total amount of intermetallic phases fall below 10 wt.% (7.5 wt.%). In the remaining four alloys, the quantity of intermetallic compounds ranges from 11.7 to 18.5 wt.%. This observation accounts for the fact that alloys containing lithium exhibit the highest Young's modulus among aluminum alloys.

Another notable characteristic of these alloys is the significantly more pronounced anisotropy in mechanical properties when compared to other aluminum alloys. Interestingly, the crystallographic texture in alloys con-

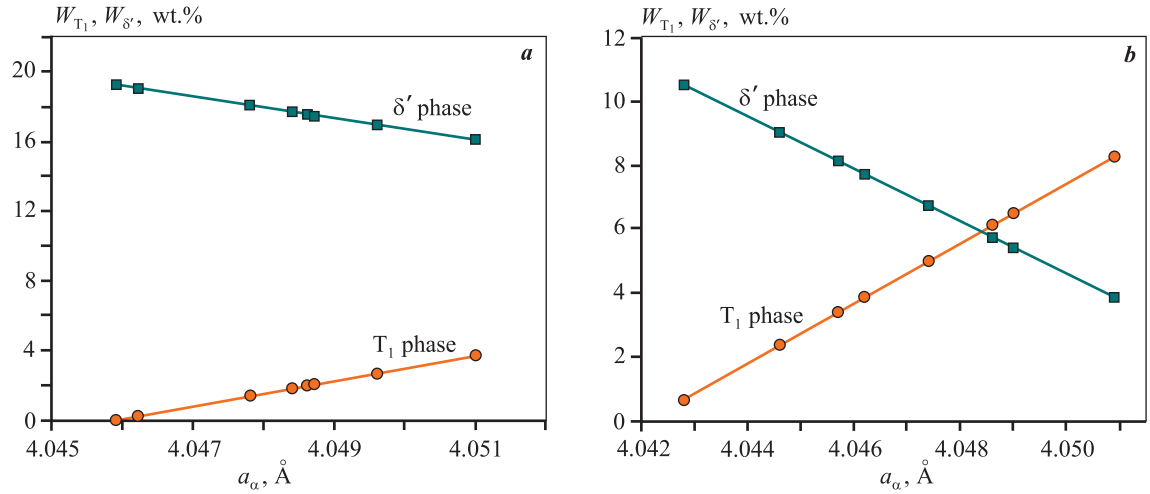

Fig. 3. Fractions of T_1 and δ′ phases as a function of the lattice period of the α-Al-solid solution in Al–Cu–Li alloys
a – alloy 1441 (1.6Cu–1.8Li); ***b*** – V-1480 (3.8Cu–1.2Li)

Рис. 3. Зависимости количества T_1 и δ′-фаз от периода решетки α-твердого раствора Al в сплавах системы Al–Cu–Li
a – сплав 1441 (1,6Cu–1,8Li); ***b*** – В-1480 (3,8Cu–1,2Li)

Table 1. **Primary alloying elements (Cu and Li), wt.%, and content of T_1 and δ′ phases, wt.%, within Al–Cu–Li alloys**

Таблица 1. Количество основных легирующих элементов (Cu и Li), мас.%, и содержание T_1- и δ′-фаз, мас.%, в сплавах системы Al–Cu–Li

Alloy	X^0_{Cu}	X^0_{Li}	X^0_{Li}/X^0_{Cu}	W_{T_1}	$W_{\delta'}$	$W_{T_1} + W_{\delta'}$
V-1480	3.8	1.2	0.32	5.0	6.7	11.7
V-1481	3.0	1.0	0.33	1.2	6.3	7.5
V-1469	3.8	1.3	0.34	4.6	8.4	13.0
V-1461	2.9	1.8	0.62	2.5	16.0	18.5
1441	1.6	1.8	1.12	1.0	17.3	18.3

Table 2. **Primary alloying elements (Cu and Li), TCLE (α), Young's modulus (*E*) and yield strength ($\sigma_{0.2}$) within Al–Cu–Li alloys**

Таблица 2. Количество основных легирующих элементов (Cu и Li), величины ТКЛР (α), модуля Юнга (*E*) и предела текучести ($\sigma_{0,2}$) в сплавах системы Al–Cu–Li

Alloy	X^0_{Cu}, wt.%	X^0_{Li}, wt.%	X^0_{Li}/X^0_{Cu}	$\alpha \cdot 10^6$, K^{-1}	*E*, GPa	$\sigma_{0,2}$, MPa
V-1480	3.8	1.2	0.32	26.2	75.3	509.2
V-1481	3.0	1.0	0.33	26.0	75.1	478.8
V-1469	3.8	1.3	0.34	25.1	74.5	509.2
V-1461	2.9	1.8	0.62	23.6	76.5	468.3
1441	1.6	1.8	1.12	22.8	77.3	366.7

taining lithium is practically indistinguishable from that in other aluminum alloys. It is possible that intermetallic phases play a role in contributing to this anisotropy effect. Investigating the anisotropy of these alloys is a distinct endeavor and will be the focus of our upcoming study. The current research aims to establish correlations between chemical and phase compositions, mechanical properties, and thermal expansion in lithium-containing alloys. Given the complexity of accounting for anisotropy, we opted to average the mechanical properties using a well-known formula for estimating the Lankford coefficient, which is averaged for sheet materials:

$$X_{avg} = (X_L + X_T + 2X_{45°})/4, \quad (3)$$

where $X = E$, σ_u, $\sigma_{0.2}$, δ are in the longitudinal rolling direction (L), transversal direction (T), and at an angle of 45°.

Figure 4, which illustrates the anisotropy of mechanical properties, showcases the results of testing in three directions for the V-1480 alloy sheet. The mechanically averaged properties, calculated using Eq. (3), are presented in Table. 2.

The increase in the X^0_{Li}/X^0_{Cu} ratio from 0.32 in alloy V-1480 to 1.12 in alloy 1441 is accompanied by a rise in Young's modulus and a decline in yield strength of these alloys (Fig. 5, *a*). However, the underlying reasons for these changes differ. The increase in Young's modulus is attributed to a rise in the overall proportion of intermetallic compounds, progressing from 7.5—13.0 wt.% in V-1481, V-1480, and V-1469 alloys to 18.3—18.5 wt.% in 1441 and V-1461 alloys (see Table 1). Conversely, the quantity of the T_1 phase decreases, contributing to a reduction in yield strength (Fig. 5, *b*). This decrease in yield strength occurs because, as demonstrated in [21], the hardening effect caused by the T_1 phase is 3—4 times greater than the hardening effect resulting from δ′ phase separation. Consequently, the decrease in the amount of the T_1 phase in 1441 and V-1461 alloys cannot be adequately offset by a significant increase in the overall proportion of intermetallic compounds in these alloys. The fact that Young's modulus increases while yield strength decreases indicates that the elastic properties of the intermetallic phases are comparable, and the overall increase in the fraction of intermetallic compounds compensates for the decrease in the T_1 phase content.

Figure 6 displays the composite *X*-ray diffraction images of the (200) planes of the α Al solid solution for alloys 1441 and V-1469. These images were acquired through imaging at temperatures of 20, 100, 200, 300, 400, and 500 °C. These images were then used to cal-

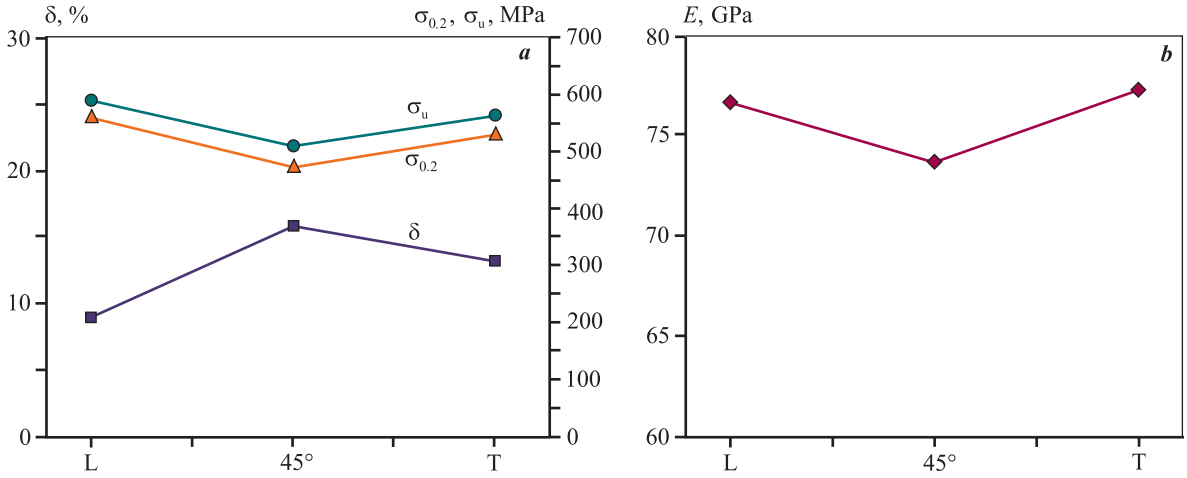

Fig. 4. Mechanical properties (δ, $\sigma_{0.2}$, σ_u, *E*) of V-1480 alloy sheets in the longitudinal rolling direction (L), transverse direction (T) and at a 45°angle

Рис. 4. Механические свойства (δ, $\sigma_{0,2}$, $\sigma_в$, *E*) листов сплава В-1480 в долевом направлении прокатки (L), поперечном (Т) и под углом 45°

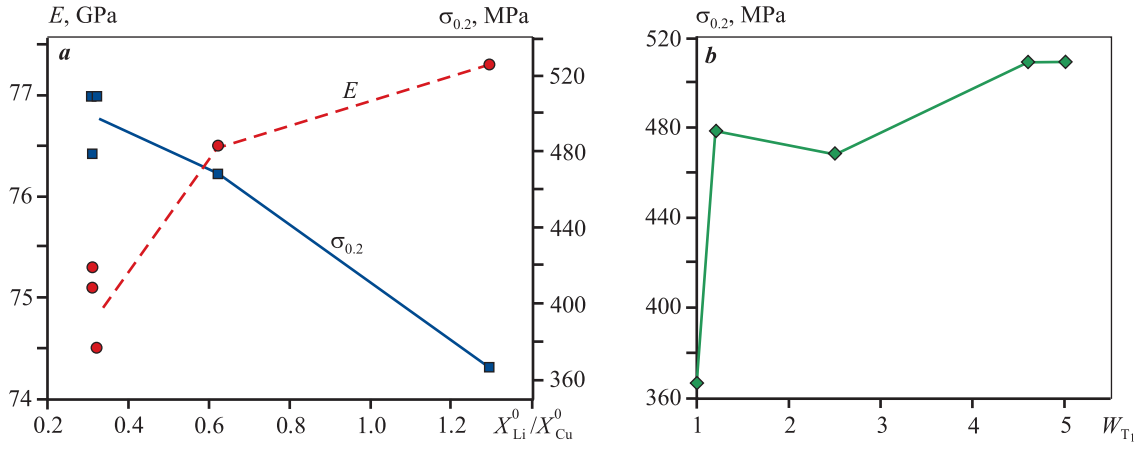

Fig. 5. Young's modulus and yield strength as functions of the ratio of lithium to copper concentration (X^0_{Li}/X^0_{Cu}) (***a***), and yield strength as a function of the amount of T_1-phase (***b***) in Al–Cu–Li alloys

Рис. 5. Зависимости модуля Юнга и предела текучести от соотношения концентраций лития и меди (X^0_{Li}/X^0_{Cu}) (***a***) и зависимость предела текучести от количества T_1-фазы (***b***) в сплавах системы Al–Cu–Li

culate the TCLE, with the resulting values (α) provided in Table 2.

The rise in the X^0_{Li}/X^0_{Cu} ratio from alloy V-1481 to alloy 1441 coincides with an increase in Young's modulus and a decrease in TCLE (Fig. 7). This pattern would be expected for a single-phase alloy, as an increase in Young's modulus typically signifies an augmentation in interatomic bonding forces, which, in turn, should lead to a reduction in TCLE. However, in the case of alloys containing lithium, the heightened Young's modulus is attributed to the substantial presence of intermetallic phases, which possess a higher Young's modulus than the solid solution. Consequently, the decrease in TCLE value may not be directly attributed to this factor. This is because the TCLE measurement pertains solely to the solid solution and not to the TCLE of the solid solution combined with intermetallic compounds, as is the case with Young's modulus measurements.

Therefore, the variation in TCLE in Al—Cu—Li alloys suggests that TCLE values, measured based on the thermal expansion of the atoms within the solid solution, exhibit a dependency on the intermetallic particles present within the solid solution. This dependency's presence should result in a violation of the additivity rule when averaging TCLE for composites and multiphase alloys comprising components with significantly different elastic properties. The most well-known models

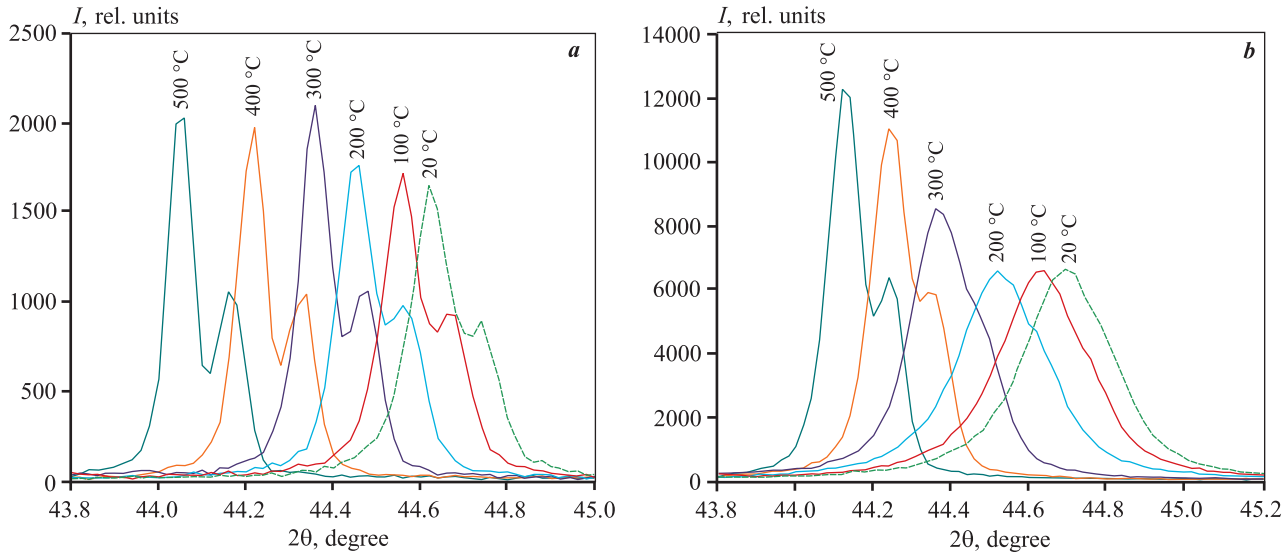

Fig. 6. Combined reflections (200) of the α Al solid solution, obtained by *X*-ray photography of alloys 1441 (***a***) and V-1469 (***b***) at different temperatures

Рис. 6. Совмещенные рефлексы (200) α-твердого раствора Al, полученные рентгеновской съемкой сплавов 1441 (***a***) и В-1469 (***b***) при различных температурах

for such averaging are the Kerner model (Eq. 4) and the Turner model (Eq. 5):

$$\alpha = \alpha_m - (\alpha_m - \alpha_p) \times \\ \times \frac{K_p(3K_m + 4G_m)V_p}{K_m(3K_p + 4G_m) + 4(K_p - K_m)G_m V_p}, \quad (4)$$

$$\alpha = \frac{\alpha_m K_m V_m + \alpha_p K_p V_p}{K_m V_m + K_p V_p}, \quad (5)$$

where $K = E/[3(1 - 2\nu)]$ represents the volumetric modulus, $G = E/[2(1 + \nu)]$ denotes the shear modulus, V_m and V_p represent the volumetric fractions of the matrix and the second phase, respectively. These models were employed in [13] during studies involving the influence of Si on TCLE of Mg—Si—Ca alloys. The results demonstrated that the experimental TCLE values align with the calculations within the framework of the Kerner model. These findings underscore the complex nature of the interaction between the matrix and the second phase during thermal expansion.

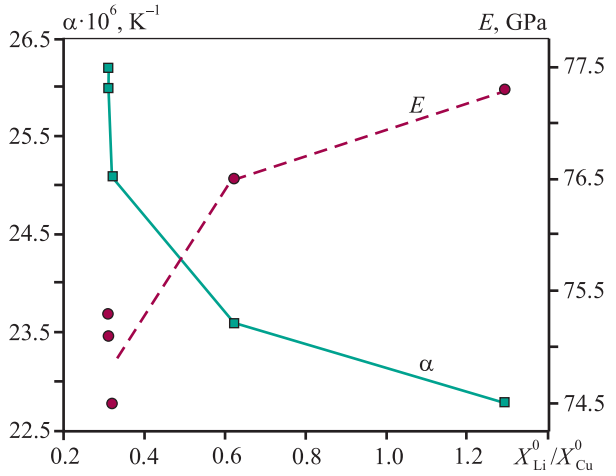

Fig. 7. Dependence of TCLE (α) and Young's modulus (*E*) as a function of the ratio of lithium to copper concentration (X^0_{Li}/X^0_{Cu}) for Al–Cu–Li alloys

Рис. 7. Зависимость ТКЛР (α) и модуля Юнга (*E*) от соотношения концентраций лития и меди (X^0_{Li}/X^0_{Cu}) для сплавов системы Al–Cu–Li

Conclusions

An analysis was conducted to examine the correlation between thermal coefficient of linear expansion (TCLE) characteristics and phase composition with the properties of Al—Cu—Li alloys under tensile stress. The study reveals that an increase in the ratio of lithium to copper content in the alloys results in a higher proportion of the δ′(Al_3Li) phase, primarily due to a decrease in the quantity of the T_1(Al_2CuLi) phase. Additionally, the overall amount of intermetallic phases increases because the δ′ phase significantly outweighs the T_1 phase in quantity. This leads to an increase in Young's modulus but a decrease in yield strength and TCLE. The rise in Young's modulus is attributed to the increased presence of intermetallic compounds, while the decline in yield

strength is associated with the decreased T_1 phase content. It's worth noting that the hardening effect of the T_1 phase is 3—4 times greater than that of the δ′ phase, and a reduction in the T_1 phase content cannot be fully compensated by an increase in the overall fraction of intermetallic compounds. The fact that Young's modulus increases while yield strength decreases indicates that the elastic properties of the intermetallic phases are similar. Consequently, the overall increase in the fraction of intermetallic compounds compensates for the decrease in the T_1 phase content. The study demonstrates that TCLE, measured based on the thermal expansion of solid solution atoms, is influenced by the characteristics of the intermetallic phases present in the alloy. This suggests that TCLE in multiphase alloys and composites results from a complex interaction among mixture components. While this complexity complicates the interpretation of TCLE measurements, it also broadens the possibilities for interpretations.

References

1. Saringer C., Kickinger C., Munnik F., Schalk N., Tkadletz M. Thermal expansion of magnetron sputtered TiC_xN_{1-x} coatings studied by high-temperature *X*-ray diffraction. *Thin Solid Films*. 2019;688:137307. https://doi.org/10.1016/j.tsf.2019.05.026
2. Chen C.-L., Thomson R.C. Study on thermal expansion of intermetallics in multicomponent Al—Si alloys by high temperature *X*-ray diffraction. *Intermetallics*. 2010;18(9):1750—1757. https://doi.org/10.1016/j.intermet.2010.05.015
3. Yong Xu, Xin Chen, Yili Cao, Kun Lin, Chin-Wei Wang, Qiang Li, Jinxia Deng, Jun Miao, Xianran Xing. Neutron diffraction study on anomalous thermal expansion of CrB_2. *Chinese Journal of Structural Chemistry*. 2023; (January):100009. https://doi.org/10.1016/j.cjsc.2022.100009
4. Dongyu Cen, Bin Wang, Ruixue Chu, Yuanyuan Gong, Guizhou Xu, Fenghua Chen, Feng Xu. Design of (Hf,Ta)Fe_2/Fe composite with zero thermal expansion covering room temperature. *Scripta Materialia*. 2020;186: 331—335. https://doi.org/10.1016/j.scriptamat.2020.05.048
5. Niu Zhang, Jinghua Li, Xiaoshuai Kong, Mengting She, Peng Guo, Jingjing Sun, Peiling Yuan, Shuaipu Zang, Mingju Chao, Erjun Liang. Negative thermal expansion property in $Nb_{14}W_3O_{44}$. *Journal of Materials Research and Technology*. 2022;18:3841—3848. https://doi.org/10.1016/j.jmrt.2022.04.083
6. Keith R. Hallama, James Edward Darnbrough, Charilaos Paraskevoulakos, Peter J. Hearda, T. James Marrow, Peter E.J.Flewitt. Measurements by *X*-ray diffraction of the temperature dependence of lattice parameter and crystallite size for isostatically-pressed graphite. *Carbon Trends*. 2021;4:100071. https://doi.org/10.1016/j.cartre.2021.100071
7. Kazuma Akikubo, Tyler Kurahashi, Sota Kawaguchi, Masaru Tachibana. Thermal expansion measurements of nano-graphite using high-temperature *X*-ray diffraction. *Carbon*. 2020;169:307—311. https://doi.org/10.1016/j.carbon.2020.07.027
8. Abhijith Vijay V., Santhy K., Sivakumar G., Rajasekaran B. Thermal expansion and microstructure evolution of atmospheric plasma sprayed NiCrAlY bond coat using in-situ high temperature *X*-ray diffraction. *Surface and Coatings Technology*. 2023;452:129132. https://doi.org/10.1016/j.surfcoat.2022.129132
9. Josef Schlacher, Zdenek Chlup, Anna-Katharina Hofer, Raul Bermejo. High-temperature fracture behaviour of layered alumina ceramics with textured microstructure. *Journal of the European Ceramic Society*. 2023;43(7): 2917—2927. https://doi.org/10.1016/j.jeurceramsoc.2022.11.046
10. Huanbei Chen, Feiyu Zheng, Weizheng Cheng, Peng Tao, Chengyi Song, Wen Shang, Benwei Fu, Tao Deng. Low thermal expansion metal composite-based heat spreader for high temperature thermal management. *Materials & Design*. 2021;208:109897. https://doi.org/10.1016/j.matdes.2021.109897
11. Hani Manssor Albetran. Thermal expansion coefficient determination of pure, doped, and co-doped anatase nanoparticles heated in sealed quartz capillaries using in-situ high-temperature synchrotron radiation diffraction. *Heliyon*. 2020;6(7):e04501. https://doi.org/10.1016/j.heliyon.2020.e04501
12. Pikea Nicholas A., Løvvika Ole M. Calculation of the anisotropic coefficients of thermal expansion: A first-principles approach. *Computational Materials Science*. 2019;167:257—263. https://doi.org/10.1016/j.commatsci.2019.05.045
13. Guo Tian, Wu Shusen, Zhou Xiong, Lü Shulin, Xia Lanqing. Effects of Si content and Ca modification on microstructure and thermal expansion property of Mg—Si alloys. *Materials Chemistry and Physics*. 2020;253:123260. https://doi.org/10.1016/j.matchemphys.2020.123260
14. Wang Xue Yi, Yang Jun, Chi Pei Zhou, Bahonar Ehsan, Tayebi Morteza. Effects of the microstructure and precipitation hardening on the thermal expansion behavior of ZK60 magnesium alloy. *Journal of Alloys and Compounds*. 2022;901:163422. https://doi.org/10.1016/j.jallcom.2021.163422
15. Ningning Dong, Jinhui Wang, Hongbin Ma, Peipeng Jin. Effects of Nd content on thermal expansion be-

havior of Mg—Nd alloys. *Materials Today Communication*. 2021;29:102894. https://doi.org/10.1016/j.mtcomm.2021.102894

16. Betsofen S.Y., Ashmarin A.A., Terent'ev V.F., Grushin I.A., Lebedev M.A. Phase composition and residual stresses in the surface layers of VNS9-Sh TRIP steel. *Russian Metallurgy (Metally).* 2020;(11):1129—1136. https://doi.org/10.1134/S0036029520100067
Бецофен С.Я., Ашмарин А.А., Терентьев В.Ф., Грушин И.А., Лебедев М.А. Фазовый состав и остаточные напряжения в поверхностных слоях трип-стали ВНС9-Ш. *Деформация и разрушение материалов*. 2020;6:12—20.
17. Ashmarin A.A., Betsofen S.Y., Lukin E.I. Effect of annealing on the phase composition and the linear thermal expansion coefficient of VNS9-Sh TRIP steel. *Russian Metallurgy (Metally).* 2022;(11):1397—1402. https://doi.org/10.1134/S0036029522110027
Ашмарин А.А., Бецофен С.Я., Лукин Е.И. Исследование влияния отжига на фазовый состав и термические коэффициенты линейного расширения трип-стали ВНС9-Ш. *Металлы*. 2022;6:66—72.
18. Betsofen S.Y., Antipov V.V., Serebrennikova N.Y., Dolgova M.I., Kabanova Yu.A. Phase composition, texture, and anisotropy of the properties of Al—Cu—Li—Mg alloy sheets. *Russian Metallurgy (Metally).* 2017;2017(10):831—837. https://doi.org/10.1134/S0036029517100044
Бецофен С.Я., Антипов В.В., Долгова М.И. Серебренникова Н.Ю., Кабанова Ю.А. Исследование фазового состава, текстуры и анизотропии свойств листов из сплавов системы Al—Cu—Li—Mg. *Деформация и разрушение материалов*. 2017;1:24—30.
19. Kablov E.N., Antipov V.V., Girsh R.I., Serebrennikova N.Yu., Konovalov A.N. Designed layered materials based on sheets of aluminum-lithium alloys and fiberglass in the designs of new generation aircrafts. *Vestnik Mashinostroeniya*. 2020;(12):46—52. (In Russ.). http://dx.doi.org/10.36652/0042-4633-2020-12-46-52
Каблов Е.Н., Антипов В.В., Гирш Р.И., Серебренникова Н.Ю., Коновалов А.Н. Конструируемые слоистые материалы на основе листов из алюминий-литиевых сплавов и стеклопластиков в конструкциях летательных аппаратов нового поколения. *Вестник машиностроения*. 2020;(12):46—52.
20. Kablov E.N., Antipov V.V., Oglodkova Yu.S., Ogladkov M.S. Development and application prospects of aluminum—lithium alloys in aircraft and space technology. *Metallurgist*. 2021;65(1-2):72—81. https://doi.org/10.1007/s11015-021-01134-9
Каблов Е.Н., Антипов В.В., Оглодкова Ю.С., Оглодков М.С. Опыт и перспективы применения алюминий-литиевых сплавов в изделиях авиационной и космической техники. *Металлург.* 2021;65(1):62—70.
21. Betsofen S.Y., Antipov V.V., Grushin I.A., Knyazev M.I., Khokhlatova L.B., Alekseev A.A. Effect of the composition of Al—Li alloys on the quantitative relation between the $\delta'(Al_3Li)$, $S_1(Al_2MgLi)$, and $T_1(Al_2CuLi)$ phases. *Russian Metallurgy (Metally).* 2015;(1):51—58. https://doi.org/10.1134/S0036029515010024
Бецофен С.Я., Антипов В.В., Грушин И.А., Князев М.И., Хохлатова Л.Б., Алексеев А.А. Закономерности влияния состава Al—Li сплавов на количественное соотношение $\delta'(Al_3Li)$, $S_1(Al_2MgLi)$ и $T_1(Al_2CuLi)$ фаз. *Металлы*. 2015;(1):59—66.

Information about the authors

Artem A. Ashmarin – Cand. Sci. (Eng.), Leading Researcher, Institute of Metallurgy and Materials Science n.a. A.A. Baikov of the Russian Academy of Sciences.
https://orcid.org/0000-0003-3160-5179
E-mail: ashmarin_artem@list.ru

Margarita I. Gordeeva – Cand. Sci. (Eng.), Associate Prof., Department 1102, Moscow Aviation Institute (National Research University) (MAI).
https://orcid.org/0009-0003-0538-6926
E-mail: gordeevami@mai.ru

Sergey Ya. Betsofen – Dr. Sci. (Eng.), Professor, Department 1101, MAI.
https://orcid.org/0000-0003-0931-2839
E-mail: s.betsofen@gmail.com

Alexander A. Lozovan – Dr. Sci. (Eng.), Professor, Department 1101, MAI.
https://orcid.org/0000-0001-9478-6793
E-mail: loz-plasma@yandex.ru

Информация об авторах

Артем Александрович Ашмарин – к.т.н., ведущий научный сотрудник Института металлургии и материаловедения им. А.А. Байкова (ИМЕТ) РАН.
https://orcid.org/0000-0003-3160-5179
E-mail: ashmarin_artem@list.ru

Маргарита Игоревна Гордеева – к.т.н., доцент кафедры 1102 Московского авиационного института (национального исследовательского университета) (МАИ).
https://orcid.org/0009-0003-0538-6926
E-mail: gordeevami@mai.ru

Сергей Яковлевич Бецофен – д.т.н., профессор, кафедра 1101 МАИ.
https://orcid.org/0000-0003-0931-2839
E-mail: s.betsofen@gmail.com

Александр Александрович Лозован – д.т.н., профессор, кафедра 1101 МАИ.
https://orcid.org/0000-0001-9478-6793
E-mail: loz-plasma@yandex.ru

Ruizhi Wu – Ph.D, Deputy Head of Key Laboratory, Harbin Engineering University.
E-mail: rzwu@hrbeu.edu.cn

Svetlana S. Alexandrova – Cand. Sci. (Eng.), Associate Prof., Department 1101, MAI.
https://orcid.org/0000-0002-3134-2375
E-mail: sweta.sergeeva@gmail.com

Andrey A. Selivanov – Cand. Sci. (Eng.), Head of the laboratory, All-Russian Research Institute of Aviation Materials of the National Research Center "Kurchatov Institute".
https://orcid.org/0009-0006-0028-1684
E-mail: julies87@mail.ru

Artem N. Bykadorov – Engineer, Department 1101, MAI.
https://orcid.org/0009-0006-9561-7354
E-mail: xartem94@mail.ru

Denis A. Prokopenko – Engineer, MAI.
https://orcid.org/0000-0002-9932-5344
E-mail: denis.prokop1234@gmail.com

Ruizhi Wu – PhD, зам. заведующего ключевой лабораторией Харбинского технического университета.
E-mail: rzwu@hrbeu.edu.cn

Светлана Сергеевна Александрова – к.т.н., доцент, кафедра 1101 МАИ.
https://orcid.org/0000-0002-3134-2375
E-mail: sweta.sergeeva@gmail.com

Андрей Аркадьевич Селиванов – к.т.н., начальник лаборатории, НИЦ «Курчатовский институт»–ВИАМ.
https://orcid.org/0009-0006-0028-1684
E-mail: julies87@mail.ru

Артем Никитич Быкадоров – инженер, кафедра 1101 МАИ.
https://orcid.org/0009-0006-9561-7354
E-mail: xartem94@mail.ru

Денис Алексеевич Прокопенко – инженер МАИ.
https://orcid.org/0000-0002-9932-5344
E-mail: denis.prokop1234@gmail.com

Contribution of the authors

A.A. Ashmarin – conducted *X*-ray phase analysis.

M.I. Gordeeva – participated in the discussion of the results.

S.Ya. Betsofen – contributed to the discussion of the results, and drafted the manuscript.

A.A. Lozovan – formulated the research objectives, contributed to the discussion of the results, and co-wrote the manuscript.

R. Wu – participated in the discussion of the result.

S.S. Alexandrova – conducted the experiments.

A.A. Selivanov – performed *X*-ray diffraction analysis.

A.N. Bykadorov – conducted experiments and contributed to the discussion of the results.

D.A. Prokopenko – prepared the initial samples.

Вклад авторов

А.А. Ашмарин – проведение рентгенофазового анализа.

М.И. Гордеева – участие в обсуждении результатов.

С.Я. Бецофен – участие в обсуждении результатов, написание статьи.

А.А. Лозован – определение цели работы, участие в обсуждении результатов, написание статьи.

R. Wu – участие в обсуждении результатов.

С.С. Александрова – проведение экспериментов.

А.А. Селиванов – проведение рентгеноструктурного анализа.

А.Н. Быкадоров – проведение экспериментов, участие в обсуждении результатов.

Д.А. Прокопенко – приготовление исходных образцов.

The article was submitted 29.06.2023, accepted for publication 04.07.2023

Статья поступила в редакцию 29.06.2023, подписана в печать 04.07.2023

UDC 669.715 : 621.793.182
https://doi.org/10.17073/0021-3438-2023-5-69-78

Research article
Научная статья

Electron-ion-plasma surface modification of hypereutectic silumin

Yu.A. Shliarova[1], V.V. Shlyarov[1], D.V. Zaguliaev[1], Yu.F. Ivanov[2], V.E. Gromov[1]

[1] **Siberian State Industrial University**
42 Kirov Str., Novokuznetsk, 654007, Russia

[2] **Institute of High-Current Electronics of Siberian Branch of the Russian Academy of Sciences**
2/3 Akademicheskiy Ave., Tomsk, 634055, Russia

✉ Yuliya A. Shliarova (rubannikova96@mail.ru)

Abstract: In this study, an integrated treatment approach was employed to modify hypereutectic silumin. This method involved electroexplosive alloying of the surface layer with yttrium oxide powder, followed by irradiation with a pulsed electron beam. The experimental data obtained demonstrate that this integrated treatment results in the formation of a submicron-nanocrystalline structure characterized by high-speed cellular crystallization of aluminum within the surface layer. This structure is composed of crystallization cells enriched with aluminum atoms, indicating the creation of a solid solution based on aluminum. The nanocrystalline layers, formed by silicon particles and yttrium oxide, are positioned at the cell boundaries. The study reveals that, as a consequence of integrated treatment with an electron beam energy density of 25 J/cm^2, the wear parameter of the modified samples increases by 7.9±0.6-fold, and the friction coefficient decreases by 1.7±0.15-fold compared to the initial state. Additionally, the microhardness of the modified silumin surface layer increases by 1.5±0.12-fold compared to the initial state. When the electron beam energy density is elevated to 35 J/cm^2, the wear parameter of silumin is enhanced by 2.1±0.21-fold, while the friction coefficient increases by 1.13±0.1-fold. However, the microhardness decreases by 1.3±0.13-fold, while still surpassing the specified characteristics of untreated silumin. This investigation postulates that the substantial increase in the wear parameter during integrated treatment may be attributed to the presence of silicon inclusions in the surface layer that did not dissolve during the modification process. These inclusions are surrounded by the high-speed cellular crystallization structure mentioned earlier.

Keywords: silumin, electroexplosive alloying, pulsed electron beam, structure, wear parameter.

Acknowledgments: This research was supported by the Russian Science Foundation, grant No. 19-79-10059, https://rscf.ru/project/19-79-10059/

For citation: Shliarova Yu.A., Shlyarov V.V., Zaguliaev D.V., Ivanov Yu.F., Gromov V.E. Electron-ion-plasma surface modification of hypereutectic silumin. *Izvestiya. Non-Ferrous Metallurgy.* 2023;29(5):69–78. https://doi.org/10.17073/0021-3438-2023-5-69-78

Электронно-ионно-плазменное модифицирование поверхности силумина заэвтектического состава

Ю.А. Шлярова[1], В.В. Шляров[1], Д.В. Загуляев[1], Ю.Ф. Иванов[2], В.Е. Громов[1]

[1] **Сибирский государственный индустриальный университет**
654007, Россия, г. Новокузнецк, ул. Кирова, 42

[2] **Институт сильноточной электроники СО РАН**
634055, Россия, г. Томск, пр. Академический, 2/3

✉ Юлия Андреевна Шлярова (rubannikova96@mail.ru)

Аннотация: В настоящем исследовании проведена сложная обработка силумина заэвтектического состава, включающая комбинацию электровзрывного легирования поверхностного слоя порошком оксида иттрия с последующим облучением импульсным

электронным пучком. Полученные данные свидетельствуют о том, что такая комплексная обработка приводит к созданию многофазной субмикро-нанокристаллической структуры высокоскоростной ячеистой кристаллизации алюминия в поверхностном слое. Объем кристаллизационных ячеек обогащен атомами алюминия, что свидетельствует об образовании твердого раствора на основе алюминия. Нанокристаллические слои, образованные частицами кремния и оксидом иттрия, расположены вдоль границ ячеек. Исследование показывает, что в результате комплексной обработки при плотности энергии электронного пучка 25 Дж/см^2 происходит увеличение параметра износа модифицированных образцов в 7,9±0,6 раза и уменьшение коэффициента трения в 1,7±0,15 раза по сравнению с силумином в исходном состоянии. Кроме того, микротвердость модифицированного таким образом поверхностного слоя силумина возрастает по сравнению с исходным состоянием в 1,5±0,12 раза. Повышение плотности энергии электронного пучка до 35 Дж/см^2 приводит к увеличению параметра износа силумина в 2,1±0,21 раза, коэффициента трения в 1,13±0,1 раза и снижению микротвердости в 1,3±0,13 раза, при этом все еще превышая заданные характеристики силумина в исходном состоянии. В исследовании предполагается, что многократное увеличение параметра износа при комплексной обработке связано с присутствием в поверхностном слое включений кремния, которые не растворились при модификации, в окружении высокоскоростной ячеистой кристаллизационной структуры.

Ключевые слова: силумин, электровзрывное легирование, импульсный электронный пучок, структура, параметр износа.

Благодарности: Исследование выполнено за счет гранта Российского научного фонда № 19-79-10059, https://rscf.ru/project/19-79-10059/

Для цитирования: Шлярова Ю.А., Шляров В.В., Загуляев Д.В., Иванов Ю.Ф., Громов В.Е. Электронно-ионно-плазменное модифицирование поверхности силумина заэвтектического состава. *Известия вузов. Цветная металлургия*. 2023;29(5):69–78.
https://doi.org/10.17073/0021-3438-2023-5-69-78

Introduction

Hypereutectic aluminum-silicon (Al—Si) casting alloys find extensive applications in the aerospace, automotive, and general engineering industries. This popularity is primarily attributed to their excellent properties, including good castability, wear and corrosion resistance, high strength, low density, good thermal conductivity, and a low coefficient of thermal expansion. [1—3]. As a result, hypereutectic Al—Si alloys are becoming attractive materials to replace conventional cast iron in engineering applications such as cylinder blocks, cylinder liners, and pistons. This substitution aims to promote fuel economy and reduce vehicle gas emissions [4; 5].

The microstructure of hypereutectic Al—Si alloys typically includes primary Si crystals and an α-Al and eutectic Si mixture. As silicon content increases, primary silicon and elongated eutectic silicon can degrade the alloy's performance by disrupting the matrix. Therefore, modifying hypereutectic Al—Si alloys to alter the morphology and distribution of these silicon phases is vital for enhancing mechanical and tribological properties [6; 7]. Furthermore, it's well-established that exposing materials to intense pulsed electron beams leads to significant changes in their surface structure and properties [8—11]. The combination of beneficial features in intense pulsed electron beams is unquestionably the core for their use in advanced techniques for modifying metal materials.

In [12—14], the hypereutectic Al—17.5Si alloy underwent treatment with a high-current pulsed electron beam. As a result, the treated surface exhibits different structural characteristics in various compositions and distribution zones: a silicon rich zone, an aluminum enriched zone, and an intermediate zone. The microstructure in the silicon-rich zone consists of small, dispersed, spherical nanosized Si crystals surrounded by Al cells. The aluminum-rich zone features a cellular microstructure with a cell size of ~100 nm. The intermediate zone forms at the boundary between two zones and consists of a eutectic structure. As the number of pulses increases, the proportion of silicon-rich zone over the entire upper surface increases, and numerous cellular substructures transform into fine equiaxed grains. In a similar study [15], irradiation of hypereutectic silumin with a lower silicon content (Al—12.6Si) leads to the formation of a fine, equiaxed grain structure, significantly improving the wear resistance of the alloy (2.5-folds).

In [16], the surface alloying of an aluminum alloy with molybdenum using a high-current electron beam was investigated. As a result, it was discovered that after irradiation, an Al_5Mo phase with a needle-like structure appeared in the alloying layer. Numerous structural defects were observed, including craters, various cracks, dislocation loops, and dislocation walls. Studies of various irradiation modes have shown that with an increase in the number of pulses, the density and size of craters formed on the irradiated surface significantly decrease; and a noticeable increase in corrosion resistance is also observed. An international scientific team conducted

research on the influence of electron beam treatment on the solubility of Sc in Al and the associated hardening effects [17].

The high-current pulsed electron beam treatment of hypereutectic Al—15Si alloy increases the tensile strength of the alloy by 41.4 %. This treatment method appears to be a y approach for enhancing the mechanical properties of hypereutectic alloys within the Al—Si system [18].

One of the most promising techniques for surface treatment of metals and alloys is the electron-ion-plasma method, which involves both coating and subsequent irradiation with an electron beam. This combination of methods enables not only the application of thermal effects to the material's surface but also alloying of the surface layer [19—21]. Collectively, these methods for influencing the structure and phase composition offer the potential to mitigate many of the shortcomings and extend the service life of machine parts and mechanisms.

The aim of this study is to investigate and analyze the patterns governing the formation of the structure and properties of hypereutectic silumin when subjected to modification with yttrium oxide particles using an integrated method that combines electroexplosive alloying with subsequent irradiation via a pulsed electron beam.

Materials and methods

In order to conduct this study at Siberian State Industrial University (SibSIU, Novokuznetsk), we produced five samples of silumin with a eutectic composition, comprising the following elements: Si — 20.28 wt.%, Fe — 1.14 %, Cu — 0.072 %, Mn — 0.015 %, Ni — 0.006 %, Ti — 0.006 %, Cr — 0.001 %, with the remainder being aluminum.

The first step of treatment involved electroexplosive alloying of the silumin. This process was carried out using an EVU 60/10 electric discharge unit at SibSIU. Aluminum foil served as the material for the exploding conductors, while Y_2O_3 was employed as the powder sample. The treatment was conducted under the following conditions: aluminum foil weight — 58.9 mg, Y_2O_3 powder mass — 58.9 mg, discharge voltage — 2.8 kV.

In the second stage, the modified surface of silumin samples underwent irradiation with a pulsed electron beam. The irradiation was performed using the SOLO facility (Institute of High Current Electronics, SB RAS, Tomsk). The irradiation parameters were as follows: accelerated electron energy — 18 keV, electron beam energy density — 25 and 35 J/cm^2, electron beam pulse duration — 150 μs, number of current pulses — 3, and pulse repetition rate — 0.3 s^{-1}.

The analysis of the irradiated surface's structure was conducted using scanning electron microscopy with an SEM-515 device (Philips, Netherlands). The elemental composition of the material's surface layer was determined through *X*-ray spectral microanalysis using an EDAX ECON IV microanalyzer, an attachment to the SEM-515 scanning electron microscope (Philips, Germany). The structural-phase state of the silumin, depending on the distance to the modification surface, was investigated using transmission electron diffraction microscopy of thin foils with a JEM-2100F device (JEOL, Japan). This technique enabled the study of defect substructures, phase composition, and highly sensitive scanning with an electron beam, as well as the examination of the foil's elemental composition through energy dispersive analysis of *X*-ray radiation. The mechanical properties of modified silumin were assessed at room temperature in air, including microhardness determination using a PMT-3 device (JSC LOMO, St. Petersburg) with an indenter load of 0.5 N. The tribological properties of the modified silumin were characterized using a TRIBOtester device, employing the Pin-on-Disc test method (France). These tests were conducted at room temperature in air, with an Al_2O_3 ball (diameter: 6 mm) as the indenter, a 5 N load on the indenter, a sample rotation speed of 25 mm/s, and a friction path length of 100 m.

Results and discussion

The studies conducted included the irradiation of silumin samples doped using the electroexplosive method. The samples were exposed to a pulsed electron beam with an energy density of 25 J/cm^2. A significant reduction in the wear parameter of the modified samples by 7.9±0.6-fold and the friction coefficient by 1.7±0.15-fold was observed compared to the cast silumin in its original state. The microhardness of the surface layer of the silumin modified in this manner showed a relatively small increase: 1.5±0.12-fold. However, an increase in the energy density of the electron beam to 35 J/cm^2 resulted in a 2.1±0.21-fold increase in the silumin wear parameter and a 1.13±0.1-fold increase in the friction coefficient. Additionally, there was a 1.3±0.13-fold decrease in microhardness compared to the characteristics of silumin modified at an electron beam energy density of 25 J/cm^2 while still exceeding the characteristics of the original silumin state.

It is evident that the mechanical and tribological characteristics of silumin are determined by the state of the structure of the modified surface layer. Figure 1 displays electron microscopic images of the silumin surface structure in its initial state, illustrating the presence of numerous faceted inclusions (dark-colored particles), needle-shaped inclusions, and inclusions resembling Chinese hieroglyphs.

It is widely recognized that faceted inclusions are silicon particles (the dark-colored particles), while hieroglyphic inclusions and needle inclusions consist of complex compounds (the light-colored particles) formed by aluminum, iron, copper, manganese, and silicon atoms [22].

In a previous study [23], focusing on silumins with eutectic composition, it was demonstrated that integrated treatment combining electroexplosive alloying with yttrium oxide and subsequent irradiation with a pulsed electron beam (at 40 J/cm^2, 200 μs pulse duration, and 3 pulses) results in the formation of a surface layer up to 150 μm thick. This layer exhibits a high-speed cellular crystallization structure, with cell volumes ranging between 400—800 nm and being comprised of an aluminum-based solid solution. These cells are separated by interlayers up to 100 nm thick, which are composed of silicon and intermetallic compounds with complex elemental compositions. This observed modification of silumin leads to a 3.5-fold increase in wear resistance, a 1.3-fold decrease in the coefficient of friction, and a 1.2-fold increase in microhardness compared to the original material. It can be hypothesized that the patterns of structural and property evolution previously established for silumin of eutectic composition, as described in [19], will also be observed in silumin with a hypereutectic composition. Indeed, the studies conducted in this work revealed the formation of a high-speed cellular crystallization structure during integrated treatment of hypereutectic silumin (Fig. 2).

X-ray microanalysis of the foils, as shown in Fig. 3, revealed that the cell volume is enriched with aluminum atoms, while the interlayers situated along the cell boundaries are predominantly enriched with silicon and yttrium atoms. Additionally, atoms of oxygen, iron, titanium, and nickel were detected in small quantities within the studied layer. These elements are considered impurities in the material under investigation.

A distinctive feature of the structure of hypereutectic silumin, which has undergone integrated modification, is the presence of silicon inclusions in the surface layer that did not dissolve during high-energy treatment. When the surface modified by the electroexplosive method is irradiated with a pulsed electron beam at an electron beam energy density of 25 J/cm^2, it results in the formation of a microtwin structure within the silicon inclusions (Fig. 4, *a*, *c*). At the same time, the silicon inclusions themselves maintain their faceted shape, which is characteristic of inclusions in cast silumin. As depicted in Fig. 4, there is evidence of the formation of silumin layers situated along the boundaries of aluminum crystallization cells. These layers exhibit a nanocrystalline structure with grains measuring 10—15 nm (Fig. 4, *c*). Additionally, the presence of yttrium oxysilicide particles is observed (Fig. 4, *d*).

Irradiating silumin with a pulsed electron beam at an electron beam energy density of 35 J/cm^2 results in

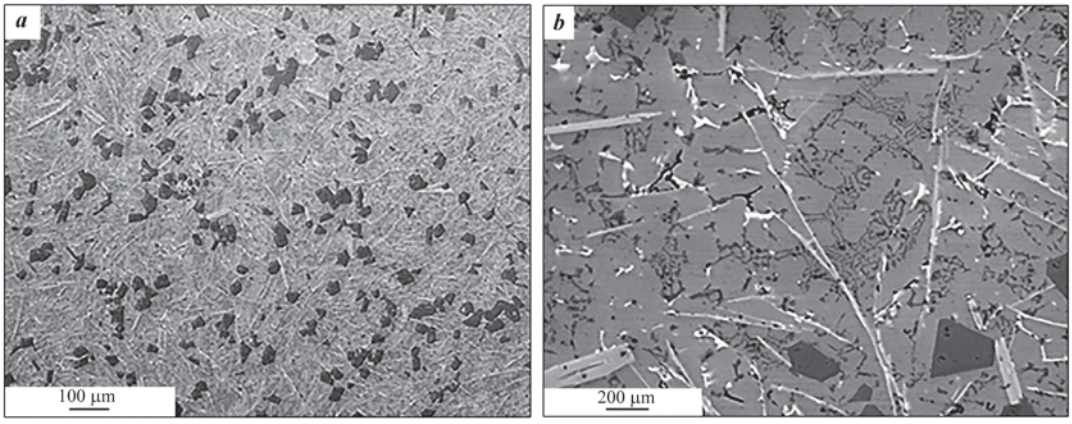

Fig. 1. Electron microscopic images of the structure of hypereutectic silumin in the initial state

Рис. 1. Электронно-микроскопические изображения структуры силумина заэвтектического состава в исходном состоянии

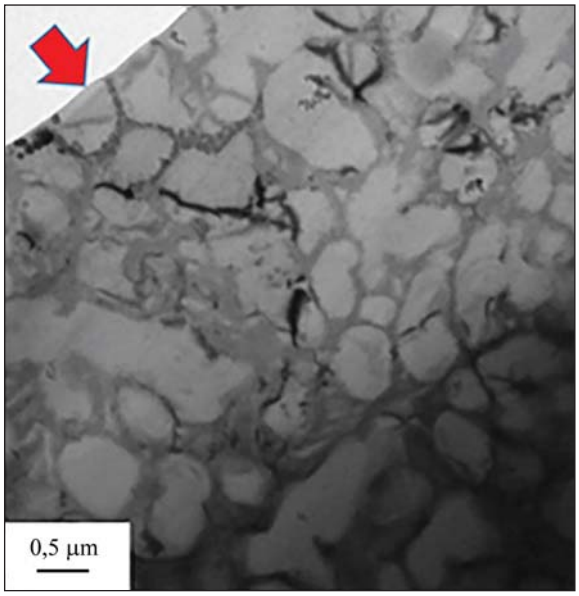

Fig. 2. Electron microscopic image of the structure of high-speed cellular crystallization formed in the surface layer of hypereutectic silumin exposed to electroexplosive alloying by yttrium oxide and subsequent irradiation by pulsed electron beam at an electron beam density of 25 J/cm^2

Modified surface is indicated by an arrow

Рис. 2. Электронно-микроскопическое изображение структуры высокоскоростной ячеистой кристаллизации, формирующейся в поверхностном слое силумина заэвтектического состава, подвергнутого электровзрывному легированию оксидом иттрия и последующему облучению импульсным электронным пучком при плотности энергии пучка электронов 25 Дж/см^2

Стрелкой указана поверхность модифицирования

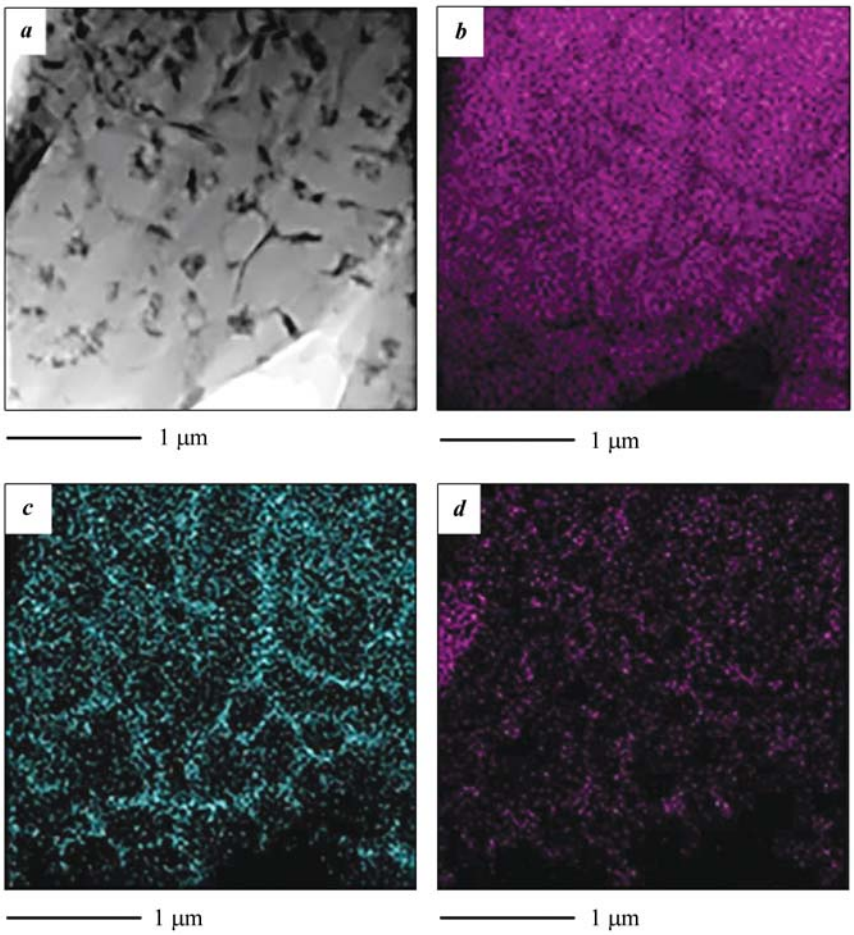

Fig. 3. Electron microscopic image of the structure of the silumin surface layer exposed to integrated treatment (25 J/cm^2) (***a***), and images of foil segment ***a***, acquired in characteristic *X*-ray irradiation of aluminum (***b***), silicon (***c***), and yttrium (***d***) atoms

Рис. 3. Электронно-микроскопическое изображение структуры поверхностного слоя силумина, подвергнутого комплексной обработке (25 Дж/см^2) (***a***), и изображения участка фольги ***a***, полученные в характеристическом рентгеновском излучении атомов алюминия (***b***), кремния (***c***), иттрия (***d***)

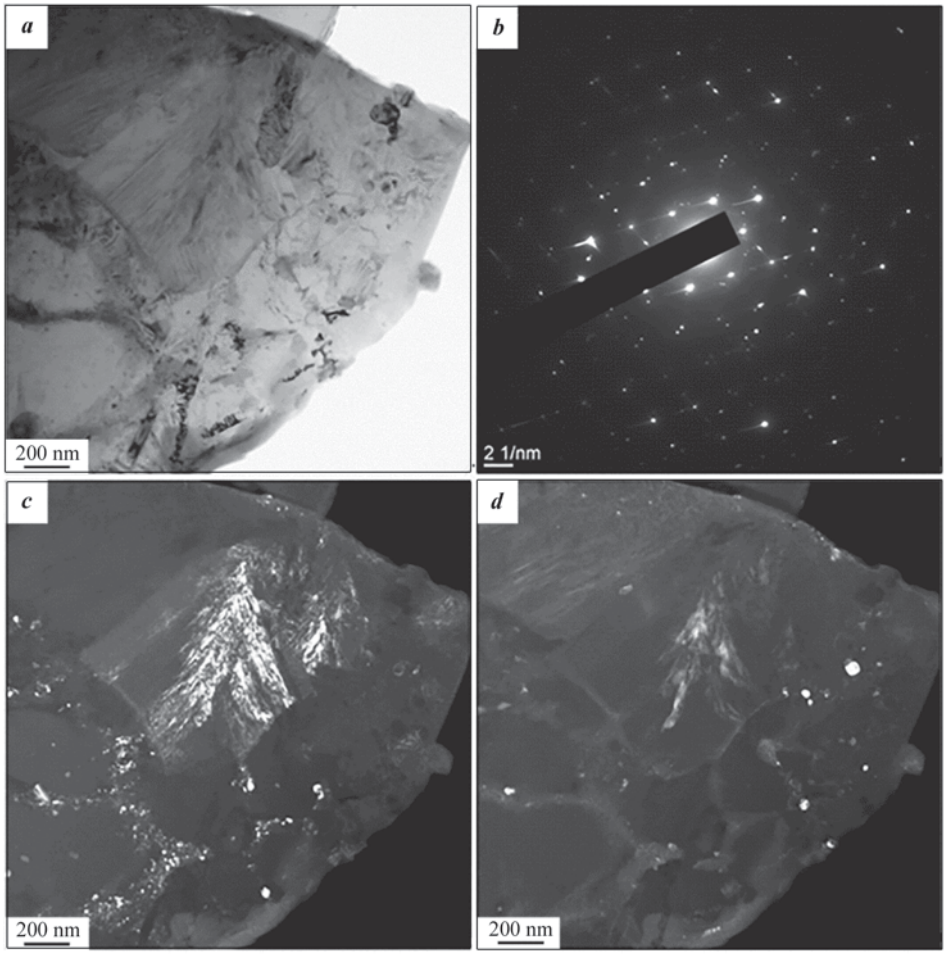

Fig. 4. Electron microscopic image of structure formed in the surface layer of hypereutectic silumin exposed to electroexplosive alloying by yttrium oxide and subsequent irradiation by pulsed electron beam at an electron beam energy density of 25 J/cm^2

a – light filed; ***b*** – electron diffraction pattern; ***c***, ***d*** – dark fields acquired in reflections [111] Si (***c***) and [022] Y_2SiO_5 (***d***)

Рис. 4. Электронно-микроскопическое изображение структуры, формирующейся в поверхностном слое силумина заэвтектического состава, подвергнутого электровзрывному легированию оксидом иттрия и последующему облучению импульсным электронным пучком при плотности энергии пучка электронов 25 Дж/см^2

a – светлое поле; ***b*** – микроэлектронограмма; ***c***, ***d*** – темные поля, полученные в рефлексах [111] Si (***c***) и [022] Y_2SiO_5 (***d***)

the development of a nanocrystalline structure within the preserved silicon inclusions, with the grains measuring between 9—30 nm. Notably, these inclusions assume a rounded (globular) shape (Fig. 5). Similar to the scenario illustrated in Fig. 4, the partial dissolution of silicon inclusions followed by high-speed crystallization of the surface layer leads to the formation of a cellular structure. This structure is characterized by the precipitation of nanosized silicon particles and yttrium oxysilicides along the boundaries of the cells (Fig. 5, *c*, *d*).

The collection of results obtained leads us to infer that the significant enhancement in the wear resistance of silumin, following integrated treatment, can be attributed, at least in part, to the presence of silicon inclusions that did not dissolve during modification. surrounded by a structure of high-speed cellular crystallization in the surface layer. These inclusions are surrounded by a high-speed cellular crystallization structure in the surface layer. This effect is observed not only in comparison to the untreated cast silumin but also in comparison to eutectic silumin that underwent a similar modification process.

Conclusions

1. Integrated treatment, which combines electroexplosive alloying with subsequent pulse irradia-

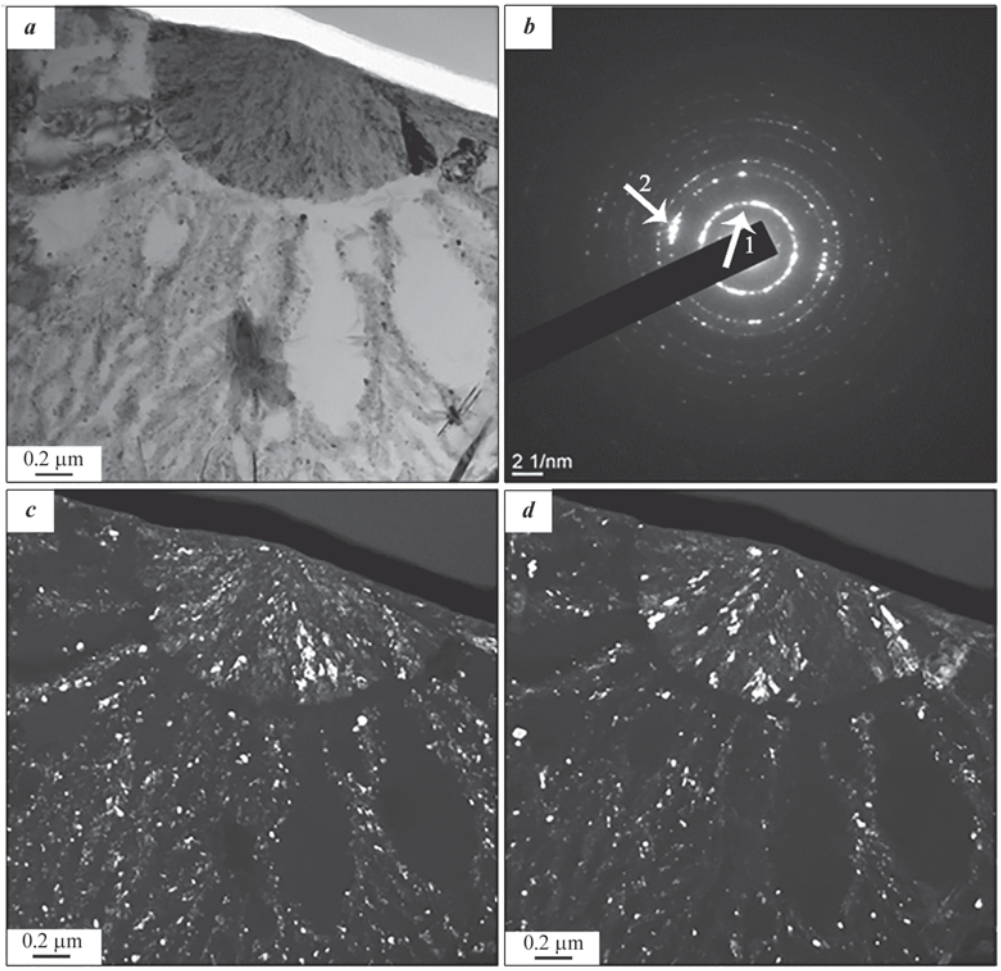

Fig. 5. Electron microscopic image of the structure formed in the surface layer of hypereutectic silumin exposed to electroexplosive alloying by yttrium oxide and subsequent irradiation by pulsed electron beam at an electron beam energy density of 35 J/cm^2

a – light filed; ***b*** – electron diffraction pattern;
c, ***d*** – dark fields acquired in reflections [111] Si (***c***) and [032] $Y_2Si_2O_7$ (***d***)

Рис. 5. Электронно-микроскопическое изображение структуры, формирующейся в поверхностном слое силумина заэвтектического состава, подвергнутого электровзрывному легированию оксидом иттрия и последующему облучению импульсным электронным пучком при плотности энергии пучка электронов 35 Дж/см^2

a – светлое поле; ***b*** – микроэлектронограмма; ***c***, ***d*** – темные поля, полученные в рефлексах
1 – [111] Si (***c***) и ***2*** – [220] Si + [032] $Y_2Si_2O_7$ (***d***)

tion using an electron beam at an energy density of 25 J/cm^2, results in a substantial 7.9±0.6-fold increase in wear parameter of the modified samples and a 1.7±0.15-fold reduction in the friction coefficient compared to the initial state of the silumin. Additionally, the microhardness of the silumin surface layer increases by 1.5±0.12-fold relative to its initial state.

2. Irradiation of samples with an electron beam energy density of 35 J/cm^2 leads to a 2.1±0.21-fold increase in the silumin wear parameter and a 1.13±0.1-fold increase in the friction coefficient, along with a 1.3±0.13-fold decrease in microhardness compared to samples modified at an electron beam energy density of 25 J/cm^2.

3. It is postulated that the substantial increase in the wear parameter of silumin following integrated treatment, when compared to both the untreated cast silumin and eutectic silumin modified in a similar manner, can be attributed to the presence of silicon inclusions in the surface layer. These silicon inclusions, which remained intact during modification, are surrounded by a high-speed cellular crystallization structure.

References

1. Tutunchilar S., Besharati Givi M.K., Haghpanahi M., Asadi P. Eutectic Al—Si piston alloy surface transformed to modified hypereutectic alloy via FSP. *Materials Science and Engineering: A.* 2012;534:557—567. https://doi.org/10.1016/j.msea.2011.12.008
2. Mohamed A.M.A., Samuel A.M., Samuel F.H., Doty H.W. Influence of additives on the microstructure and tensile properties of near-eutectic Al—10.8%Si cast alloy. *Materials & Design*. 2009;30(10):3943—3957. https://doi.org/10.1016/j.matdes.2009.05.042
3. Li Q., Xia T., Lan Y., Li P., Fan L. Effects of rare earth Er addition on microstructure and mechanical properties of hypereutectic Al—20% Si alloy. *Materials Science and Engineering: A*. 2013;588:97—102. https://doi.org/10.1016/j.msea.2013.09.017
4. Chen M., Meng-Burany X., Perry T.A., Alpas A.T. Micromechanisms and mechanics of ultra-mild wear in Al—Si alloys. *Acta Materialia*. 2008;56(19):5605—5616. https://doi.org/10.1016/j.actamat.2008.07.043
5. Chen M., Alpas A.T. Ultra-mild wear of a hypereutectic Al—18.5wt.%Si alloy. *Wear*. 2008;265(1-2):186—195. https://doi.org/10.1016/j.wear.2007.10.002
6. Cao F., Jia Y., Prashanth K.G., Ma P., Liu J., Scudino S., Huang F., Eckert J., Sun J. Evolution of microstructure and mechanical properties of as-cast Al—50Si alloy due to heat treatment and P modifier content. *Materials & Design*. 2015;74:150—156. https://doi.org/10.1016/j.matdes.2015.03.008
7. Li Q., Xia T., Lan Y., Zhao W., Fan L., Li P. Effect of in situ γ-Al_2O_3 particles on the microstructure of hypereutectic Al—20%Si alloy. *Journal of Alloys and Compounds*. 2013;577:232—236. https://doi.org/10.1016/j.jallcom.2013.04.043
8. Wenhai P., Shengzhi H., Jun C., Wei L., Limin Z., Jun D. Surface composite microstructure and improved mechanical property of YG10X cemented carbide induced by high current pulsed electron beam irradiation. *International Journal of Refractory Metals and Hard Materials*. 2019;78:233—239. https://doi.org/10.1016/j.ijrmhm.2018.09.016
9. Hangyu Y., Yuyong C., Xiaopeng W., Fantao K. Effect of beam current on microstructure, phase, grain characteristic and mechanical properties of Ti—47Al—2Cr—2Nb alloy fabricated by selective electron beam melting. *Journal of Alloys and Compounds*. 2018;750:617—625. https://doi.org/10.1016/j.jallcom.2018.03.343
10. Wei J., Langping W., Xiaofeng W. Studies on surface topography and mechanical properties of TiN coating irradiated by high current pulsed electron beam. *Nuclear Instruments and Methods in Physics Research Section B: Beam Interactions with Materials and Atoms*. 2018;436:63—67. https://doi.org/10.1016/j.nimb.2018.09.003
11. Zou J., Qin Y., Dong C., Wang X., Almin W., Hao S. Numerical simulation of the thermal-mechanical process of high current pulsed electron beam treatment. *Journal of Vacuum Science and Technology A: Vacuum, Surfaces and Films*. 2004;22(3):545—552. https://doi.org/10.1116/1.1697481
12. Gao B., Hao Y., Zhuang W.F., Tu G.F., Shi W.X., Li S.W., Hao S.Z., Dong C., Li M.C. Study on continuous solid solution of Al and Si elements of a high current pulsed electron beam treated hypereutectic Al—17.5Si alloy. *Physics Procedia*. 2011;18:187—192. https://doi.org/10.1016/j.phpro.2011.06.079
13. Gao B., Hu L., Li S., Hao Y., Zhang Y., Tu G., Grosdidier T. Study on the nanostructure formation mechanism of hypereutectic Al—17.5Si alloy induced by high current pulsed electron beam. *Applied Surface Science*. 2015;346:147—157. https://doi.org/10.1016/j.apsusc.2015.04.029
14. Hu L., Gao B., Lv J.K., Hao Y., Tu G.F., Hao S.Z., Dong C. The metastable structure of hypereutectic Al—17.5Si alloy surface induced by high current pulsed electron beam. *Materials Research Innovations*. 2015;19:S5320—S5324. https://doi.org/10.1179/1432891714Z.0000000001102
15. Hao Y., Gao B., Tu G.F., Cao H., Hao S.Z., Dong C. Surface modification of Al—12.6Si alloy by high current pulsed electron beam. *Applied Surface Science*. 2012;258:2052—2056. https://doi.org/10.1016/j.apsusc.2011.04.104
16. Xia H., Zhang C., Lv P., Cai J., Jin Y., Guan Q. Surface alloying of aluminum with molybdenum by high-current pulsed electron beam. *Nuclear Instruments and Methods in Physics Research Section B: Beam Interactions with Materials and Atoms*. 2018;416:9—15. https://doi.org/10.1016/j.nimb.2017.11.028
17. Tomus D., Qian M., Brice C.A., Muddle B.C. Electron beam processing of Al—2Sc alloy for enhanced precipitation hardening. *Scripta Materialia*. 2010;63(2):151—154. https://doi.org/10.1016/j.scriptamat.2010.03.039
18. Bo G., Ning X., Pengfei X. Shock wave induced

nanocrystallization during the high current pulsed electron beam process and its effect on mechanical properties. *Materials Letters*. 2019;237:180—184. https://doi.org/10.1016/j.matlet.2018.11.054

19. Zaguliaev D., Gromov V., Rubannikova Yu., Konovalov S., Ivanov Yu., Romanov D., Semin A. Structure and phase states modification of Al—11Si—2Cu alloy processed by ion-plasma jet and pulsed electron beam. *Surface and Coatings Technology*. 2020; 383:125246. https://doi.org/10.1016/j.surfcoat.2019.125246
20. Zaguliaev D., Konovalov S., Ivanov Yu., Gromov V., Petrikova E. Microstructure and mechanical properties of doped and electron-beam treated surface of hypereutectic Al—11.1%Si alloy. *Journal of Materials Research and Technology*. 2019;8(5):3835—3842. https://doi.org/10.1016/j.jmrt.2019.06.045
21. Zaguliaev D., Konovalov S., Ivanov Yu., Gromov V. Effect of electron-plasma alloying on structure and mechanical properties of Al—Si alloy. *Applied Surface Science*. 2019;498:143767. https://doi.org/10.1016/j.apsusc.2019.143767
22. Belov N.A., Savchenko S.V., Khvan A.V. Phase composition and structure of silumins. Moscow: MISIS, 2008. 282 p. (In Russ.).
Белов Н.А., Савченко С.В., Хван А.В. Фазовый состав и структура силуминов. М.: МИСиС, 2008. 282 с.
23. Gromov V.E., Zagulyaev D.V., Ivanov Yu.F., Konovalov S.V., Nevskii S.A., Sarychev V.D., Budovskikh E.A., Rubannikova Yu.A. Structure and hardening of silumin modified by electron-ion plasma. Novokuznetsk: Publishing Center SibGIU, 2020. 284 p. (In Russ.).
Громов В.Е., Загуляев Д.В., Иванов Ю.Ф., Коновалов С.В., Невский С.А., Сарычев В.Д., Будовских Е.А., Рубанникова Ю.А. Структура и упрочнение силумина, модифицированного электронно-ионной плазмой. Новокузнецк: Изд центр СибГИУ, 2020. 284 с.

Information about the authors

Yuliya A. Shliarova – Postgraduate Student of the Department of Natural Science Disciplines of Siberian State Industrial University (SibSIU), Researcher of the Laboratory of electron microscopy and image processing of SibSIU.
https://orcid.org/0000-0001-5677-1427
E-mail: rubannikova96@mail.ru

Vitaliy V. Shlyarov – Postgraduate Student of SibSIU, Researcher of the Laboratory of electron microscopy and image processing of SibSIU.
https://orcid.org/0000-0001-8130-648X
E-mail: shlyarov@mail.ru

Dmitriy V. Zaguliaev – Dr. Sci. (Eng.). Deputy Head of Scientific Research Department of SibSIU.
https://orcid.org/0000-0002-9859-8949
E-mail: zagulyaev_dv@physics.sibsiu.ru

Yuriy F. Ivanov – Dr. Sci. (Phys.-Math.), Professor, Chief Researcher of the Institute of High-Current Electronics of Siberian Branch of the Russian Academy of Sciences.
https://orcid.org/0000-0001-8022-7958
E-mail: yufi55@mail.ru

Viktor E. Gromov – Dr. Sci. (Phys.-Math.), Professor, Head of the Department of Natural Science Disciplines of SibSIU.
https://orcid.org/0000-0002-5147-5343
E-mail: gromov@physics.sibsiu.ru

Информация об авторах

Юлия Андреевна Шлярова – аспирант кафедры естественно-научных дисциплин Сибирского государственного индустриального университета (СибГИУ), научный сотрудник лаборатории электронной микроскопии и обработки изображений СибГИУ.
https://orcid.org/0000-0001-5677-1427
E-mail: rubannikova96@mail.ru

Виталий Владиславович Шляров – аспирант кафедры естественно-научных дисциплин СибГИУ, научный сотрудник лаборатории электронной микроскопии и обработки изображений СибГИУ.
https://orcid.org/0000-0001-8130-648X
E-mail: shlyarov@mail.ru

Дмитрий Валерьевич Загуляев – д.т.н., зам. начальника управления научных исследований СибГИУ.
https://orcid.org/0000-0002-9859-8949
E-mail: zagulyaev_dv@physics.sibsiu.ru

Юрий Федорович Иванов – д.ф.-м.н., профессор, главный научный сотрудник Института сильноточной электроники СО РАН.
https://orcid.org/0000-0001-8022-7958
E-mail: yufi55@mail.ru

Виктор Евгеньевич Громов – д.ф.-м.н., профессор, заведующий кафедрой естественно-научных дисциплин СибГИУ.
https://orcid.org/0000-0002-5147-5343
E-mail: gromov@physics.sibsiu.ru

Contribution of the authors

Yu.A. Shliarova – formulation of the main concept, goal, and objectives of the study, manuscript writing.

V.V. Shlyarov – experiment preparation, experiment execution, literature review.

D.V. Zaguliaev – scientific guidance, manuscript revision, and results analysis.

Yu.F. Ivanov – electron microscopic studies, results analysis.

V.E. Gromov – work concept, TEM images analysis, manuscript writing, conclusions formulation.

Вклад авторов

Ю.А. Шлярова – формирование основной концепции, постановка цели и задачи исследования, подготовка текста.

В.В. Шляров – подготовка экспериментов, проведение экспериментов, обзор литературы.

Д.В. Загуляев – научное руководство, корректировка текста, корректировка выводов.

Ю.Ф. Иванов – проведение электронно-микроскопических исследований, анализ результатов.

В.Е. Громов – концепция работы, анализ ПЭМ-изображений, подготовка текста, формулировка выводов.

The article was submitted 03.02.2023, revised 25.05.2023, accepted for publication 30.05.2023

Статья поступила в редакцию 03.02.2023, доработана 25.05.2023, подписана в печать 30.05.2023